

N° d'ordre NNT : 2017LYSE1065

THÈSE DE DOCTORAT DE L'UNIVERSITÉ DE LYON
opérée au sein de
l'Université Claude Bernard Lyon 1

École Doctorale ED52
Physique et Astrophysique de Lyon

Spécialité de doctorat : Physique des particules

Soutenue publiquement le 21/04/2017, par :
Davide Caiulo

Charge readout analysis in Liquid Argon Time Projection Chambers for neutrino and astro-particle physics

---

Devant le jury composé de :

NEDELEC Patrick,	Professeur des Universités, Université Lyon 1	Président
JOLLET Cécile,	Maître de Conférences - HDR, Université de Strasbourg	Rapporteur
HASEGAWA Takuya,	Professeur, KEK, Tsukuba (Japon)	Rapporteur
FARIZON Bernadette,	Directrice de Recherche, CNRS Lyon	Examinatrice
PESSARD Henri,	Directeur de Recherche, CNRS Annecy	Examinateur
AUTIERO Dario,	Directeur de Recherche, CNRS Lyon	Directeur de thèse

UNIVERSITE CLAUDE BERNARD - LYON 1

Président de l'Université	**M. le Professeur Frédéric FLEURY**
Président du Conseil Académique	M. le Professeur Hamda BEN HADID
Vice-président du Conseil d'Administration	M. le Professeur Didier REVEL
Vice-président du Conseil Formation et Vie Universitaire	M. le Professeur Philippe CHEVALIER
Vice-président de la Commission Recherche	M. Fabrice VALLÉE
Directrice Générale des Services	Mme Dominique MARCHAND

COMPOSANTES SANTE

Faculté de Médecine Lyon Est – Claude Bernard	Directeur : M. le Professeur G.RODE
Faculté de Médecine et de Maïeutique Lyon Sud – Charles Mérieux	Directeur : Mme la Professeure C. BURILLON
Faculté d'Odontologie	Directeur : M. le Professeur D. BOURGEOIS
Institut des Sciences Pharmaceutiques et Biologiques	Directeur : Mme la Professeure C. VINCIGUERRA
Institut des Sciences et Techniques de la Réadaptation	Directeur : M. X. PERROT
Département de formation et Centre de Recherche en Biologie Humaine	Directeur : Mme la Professeure A-M. SCHOTT

COMPOSANTES ET DEPARTEMENTS DE SCIENCES ET TECHNOLOGIE

Faculté des Sciences et Technologies	Directeur : M. F. DE MARCHI
Département Biologie	Directeur : M. le Professeur F. THEVENARD
Département Chimie Biochimie	Directeur : Mme C. FELIX
Département GEP	Directeur : M. Hassan HAMMOURI
Département Informatique	Directeur : M. le Professeur S. AKKOUCHE
Département Mathématiques	Directeur : M. le Professeur G. TOMANOV
Département Mécanique	Directeur : M. le Professeur H. BEN HADID
Département Physique	Directeur : M. le Professeur J-C PLENET
UFR Sciences et Techniques des Activités Physiques et Sportives	Directeur : M. Y.VANPOULLE
Observatoire des Sciences de l'Univers de Lyon	Directeur : M. B. GUIDERDONI
Polytech Lyon	Directeur : M. le Professeur E.PERRIN
Ecole Supérieure de Chimie Physique Electronique	Directeur : M. G. PIGNAULT
Institut Universitaire de Technologie de Lyon 1	Directeur : M. le Professeur C. VITON
Ecole Supérieure du Professorat et de l'Education	Directeur : M. le Professeur A. MOUGNIOTTE
Institut de Science Financière et d'Assurances	Directeur : M. N. LEBOISNE

I would like to thank the people who accompanied me during the PhD for their support.

First of all, I would to thank my director Dario Autiero, who offered me the opportunity to work on this interesting subject and who patiently supervised me in these years teaching me a lot about neutrino physics.

I would also like to thank my referees, Cécile Jollet and Takuya Hasegawa, who accepted to read carefully the manuscript and gave me suggestions to improve my work.

I am also grateful to Bernadette Farizon, Patrick Nedelec and Henri Pessard for accepting to be part of my thesis committee.

I thank Elisabetta and Slavic, who were of great help during my work. The discussions within the neutrino group of the IPNL were always very rich and enlightening.

I would like to thank Sylvie Flores, who helped me with all the bureaucratic procedures since I arrived in France and reminded me several times all the deadlines before the thesis defence.

A special thanks to the IPNL, who provided a great work environment during these years, as well as the Université Claude Bernard Lyon 1, who gave me the opportunity to gain experience in the academic sphere.

I would like to express my gratitude to the WA105 collaboration for giving me the occasion to participate to this challenging experiment and to meet researchers involved in neutrino physics.

Finally I would like to thank my friends and my family.
Un grand merci à vous tous, les amis (plus ou moins) lyonnais qui m'avez soutenu et encouragé ces années: Vanessa et Pierre, Biagio, Anna Claudia, Marcel, Yiru, Victor, Teresa, Véronique, Murray, Alessandra, Lorenzo, Luigia et Guillaume, Manuela, et tous les autres. Vous êtes devenus ma deuxième famille et je vous suis reconnaissant pour tous les moments inoubliables passés ensemble.

Infine, un ringraziamento speciale alla mia famiglia: grazie per avermi sempre sostenuto e incoraggiato nelle mie scelte, grazie per avermi sempre stimolato a cercare di soddisfare la mia curiosità sin da quando ero piccolo. È grazie a voi se sono arrivato fin qui.

Я посвящаю эту работу тебе, которая была рядом со мной в этом году, сделав мою работу более лёгкой и наполнив каждый момент моего дня счастьем.

Contents

1 Neutrino oscillations physics **3**
- 1.1 Observation of neutrino oscillations . . . 4
  - 1.1.1 Sudbury Neutrino Observatory . . . 4
  - 1.1.2 Super-Kamiokande . . . 5
- 1.2 Oscillations . . . 8
- 1.3 CP violation . . . 12
- 1.4 Deep Underground Neutrino Experiment . . . 13

2 Liquid Argon Time Projection Chamber (LAr TPC) **19**
- 2.1 Basic concept of a Liquid Argon Time Projection Chamber . . . 20
- 2.2 Ionization process . . . 22
  - 2.2.1 Recombination . . . 23
  - 2.2.2 Scintillation . . . 23
- 2.3 Drift and diffusion processes . . . 25
- 2.4 Dual-phase readout . . . 28
  - 2.4.1 Large Electron Multiplier (LEM) . . . 29
  - 2.4.2 Anode charge collection . . . 30
- 2.5 Differences between single-phase TPC and dual-phase TPC . . . 32
- 2.6 Future experiments . . . 33
  - 2.6.1 DUNE . . . 33
  - 2.6.2 WA105/ProtoDUNE dual-phase . . . 34

3 Verification of the Paschen law **39**
- 3.1 The Paschen law derivation . . . 40
- 3.2 Experimental apparatus . . . 41
- 3.3 Paschen measurements analysis . . . 45
- 3.4 Application of the results . . . 55

4 Charge readout analysis **57**
- 4.1 The Qscan software . . . 58
- 4.2 Energy losses simulation . . . 61
- 4.3 Simulation of detector response . . . 66
  - 4.3.1 Charge digitization . . . 66

4.3.2 Drift and diffusion . . . 67
4.3.3 ADC conversion . . . 72
4.3.4 Hit reconstruction . . . 72
4.3.5 Energy reconstruction . . . 75
4.4 Reconstruction effects on energy losses measurement . . . 76
4.5 Summary . . . 79

5 Kaons and pions separation using energy losses 83
5.1 Proton decay . . . 85
5.2 Definition and generation of the Monte Carlo samples . . . 85
5.3 Energy loss parametrization and particles ID analysis . . . 92
5.4 Development of the kaon identification algorithm . . . 98
5.4.1 Simulation including only fluctuations . . . 98
5.4.2 Simulation including fluctuations and noise . . . 102
5.4.3 Simulation including δ-rays and noise . . . 105
5.5 Event energy cut . . . 109
5.6 Summary . . . 120

6 Electron/photon separation and π^0 rejection 123
6.1 Definition and generation of the Monte Carlo samples . . . 124
6.2 Energy profile reconstruction and *electron*/γ separation . . . 126
6.3 White noise effects . . . 131
6.4 Summary . . . 133

7 Conclusions 137

Bibliography 139

Introduction

The discovery of the Higgs boson and its characterization embody a confirmation of the Standard Model (SM). A crucial point for the future of Particle Physics is the study of the neutrino masses and mixing representing the first established evidence of physics beyond the SM. Since 2011, the large value of the θ_{13} mixing angle opened the way to the investigation of CP violation in the neutrino sector. A next generation long baseline neutrino experiment (DUNE) has unprecedented potential to precisely measure the neutrino oscillation parameters, determine the neutrino mass hierarchy and has a very good chance to discover evidence for CP violation in the leptonic sector. The large underground neutrino detectors needed for this task will also address the search for proton decay and the observation of supernovae neutrinos.

Giant Liquid Argon Time Projection Chambers (LAr TPCs) will be employed as neutrino targets and detectors. They provide bubble-chamber quality imaging coupled to excellent energy resolution and particles identification capabilities. Neutrino interactions produce secondary particles, which ionize the liquid argon. The ionization electrons drift for long distances along a uniform electric field present inside the TPC until they reach finely segmented and instrumented anodes, producing electrical signals that are used for 3D imaging and analysis of the primary interactions. The dual-phase readout technique foresees the amplification of the ionization signal in avalanches occurring in the gas phase above the liquid argon level. This technique further enhances the performance of the LAr TPC by increasing its signal to noise ratio and allowing for a finer segmentation and lower threshold.

The subject of this thesis is the ionization charge reconstruction and analysis in the dual-phase LAr TPC: the ionization charges measurement is a crucial information provided by the detector. It provides information about the kinetic energy of secondary charged particles produced in neutrino interactions. In this way, it is possible to reconstruct the incoming neutrino energy. Ionization measurements make also possible identifying and rejecting electromagnetic shower generated by photons from π^0 decay and performing particles identification from the measurement of the specific ionization losses.

All these measurements imply a detailed knowledge of the detector response and of the charge reconstruction algorithm. In order to achieve this knowledge a detailed analysis of the simulated energy losses has been performed by studying the differences between the theoretical knowledge and the simulation. Then the simulation of the detector response has been studied by looking at the effects occurring during the drift of the charges and

at the effects related to the response of the electronic readout. These systematic effects affecting the accuracy of the reconstruction algorithm are then characterized with respect to the Monte Carlo generation.

By sampling the trajectory of a charged particle and by measuring its energy losses, it is possible to identify its nature. A giant Lar TPC is also an ideal environment to search for proton decay, in particular by looking at some exclusive decay channels such as $p \rightarrow K + \overline{\nu}$ decay. In this thesis it is studied as well how particles identification based on energy losses measurement allows identifying charged kaons.

Successively it is shown how it is possible to perform π^0 rejection by studying energy losses. The production of π^0 in neutral current neutrino interactions and the conversion of photons from π^0 decays in proximity of the neutrino interaction vertex represent an important background source to the detection of charged current interactions of electron neutrinos. By measuring the ionization profile at the beginning of an electromagnetic shower it is possible to understand if the shower has been produced by an electron or by a photon. A photon conversion in an electron-positron pair will result in the double of the ionization deposited by a genuine electron track originating the shower. The measurement of the ionization profile allows rejecting the photons background in the electron neutrino appearance channel, fundamental for the search for CP violation.

Chapter 1 introduces the neutrino oscillation, starting from the description of the two main experiments which proved the existence of neutrino oscillations and describing subsequently the neutrino oscillations phenomenology and δ_{CP} measurements.

Chapter 2 presents the Liquid Argon Time Projection Chamber (LAr TPC), with a description of all the effects involved in the charge generation, transport and detection. A description of the dual-phase readout and of the Large Electron Multiplier (LEM) is presented, showing the differences between single-phase and dual-phase TPC.

Chapter 3 describes a study on the Paschen law. The operation of the LEM in the dual-phase Liquid Argon TPC requires a good knowledge about the maximal voltage that can be applied to the LEM before starting an electric arc. In this Chapter is presented an experimental study aimed at verifying the Paschen law in pure gaseous argon at cryogenic temperatures.

Chapter 4 presents a detailed analysis of the charge readout, with a description of the energy depositions simulation, the detector response simulation and charge digitization. Finally a comparison between the Monte Carlo generation and reconstructed energy is presented.

Chapter 5 discusses the study of the energy losses profile in proximity of the stopping point for pions and kaons, the extraction of a parametrization of these energy losses and the definition of a particle identification algorithm for the identification of kaons in the proton decay search.

Chapter 6 reports the study performed in order to obtain a parametrization of the ionization charge profile produced in an electromagnetic shower for electrons and photons as a function of the distance from the starting point of the cascade, and a definition of the analysis procedure allowing to distinguish the originating particle of the shower.

Chapter 1

Neutrino oscillations physics

In 2015 the Nobel Prize in Physics was awarded jointly to Takaaki Kajita and Arthur B. McDonald "for the discovery of neutrino oscillations, which shows that neutrinos have mass". First ideas of neutrino masses, mixing and oscillations were developed by Bruno Pontecorvo at the end of the 1950s. In 1968 the first detection of solar neutrinos was performed by R. Davis. After it, several experiments studied neutrino oscillations. Two experiments proved definitively the existence of neutrino oscillations: in 1998 Super-Kamiokande observing neutrinos created by cosmic ray interactions in the atmosphere and the Sudbury Neutrino Observatory (SNO) in 2001, measuring the neutrino flux from the Sun.

In the last years several experiments contributed to increase the comprehension of neutrino oscillations. Thanks to them actually a good knowledge of this physical process has been achieved. Nevertheless some parameters which govern the neutrino mixing are still unknown. The current challenge in neutrino physics is to provide measurements for these parameters, in order to complete our knowledge on neutrinos and to exploit a window opened on physics beyond the SM. Thanks to the recent measurements of θ_{13}, it is now possible to perform experiments to study neutrino and anti-neutrino oscillations in order to determine if the charge-parity (CP) symmetry is violated in the leptonic sector. The best way to perform these measurements is based on long-baseline experiments, with a distance between neutrino source and the detector of $\gtrsim 1000$ km. The Deep Underground Neutrino Experiment (DUNE) is currently the most advanced initiative towards the measurement of the CP violation phase δ_{CP}.

This Chapter describes the two experiments which proved the existence of neutrino oscillations and the results they obtained. Then, a short formal introduction to neutrino oscillations is given, describing the oscillation matrix and its parameters. The results obtained so far and the experimental challenges for the continuation of this research line are presented. Subsequently, the measurement of δ_{CP} is discussed, including the effects of the interaction between neutrinos and Earth crust matter related to the neutrino masses hierarchy. It is shown how a long baseline experiment is capable to solve the mass hierarchy problem and to measure the CP violation phase at the same time. Finally a short description of the scientific goals of the future long base-line experiment DUNE is given.

1.1 Observation of neutrino oscillations

1.1.1 Sudbury Neutrino Observatory

The Sudbury Neutrino Observatory (SNO) was a solar-neutrino experiment which collected data in the period going from 1999 to 2006. This experiment used 1000 t of heavy water (D_2O) contained in a spherical acrylic vessel. The heavy water was surrounded by 9438 photomultipliers in order to detect the Čerenkov light produced with the neutrino interaction after its propagation in the D_2O. Other 91 outward-looking photomultipliers were constituting a veto system in order to detect photons produced by cosmic-ray muons crossing the detector. The entire cavity outside of the acrylic sphere was filled with 7000 t of water.

The SNO experiment was built in order to solve the Solar Neutrino Problem [1] by performing a flavor independent measurement of the solar neutrino flux. It was studying mainly neutrinos coming from the β-decay of ^{8}B in the Sun:

$$^8\mathrm{B} \rightarrow ^8\mathrm{Be} + e^+ + \nu_e \tag{1.1}$$

achieving a effective electron kinetic energy threshold $T_{eff} = 3.5$ MeV [2].

Previous solar neutrino experiments were either exclusively (chlorine, gallium) or predominantly (H_2O) sensitive to the electron-type neutrinos produced in the Sun. The SNO experiment was able to measure separately three reactions:

$$\nu_e + d \rightarrow p + p + e^- \tag{1.2}$$

$$\nu_x + d \rightarrow n + p + \nu_x \tag{1.3}$$

$$\nu_x + e^- \rightarrow \nu_x + e^- \tag{1.4}$$

The reaction (1.2) is a charged current (CC) reaction which is sensitive only to electron neutrinos. The reaction (1.3) is a neutral current (NC) reaction and it is sensitive to all active neutrino flavors. The reaction (1.4) is the elastic scattering (ES) which is mainly sensitive to electron neutrinos but has also some sensitivity to other flavors via its NC component.

The NC reaction provides a measurement of the total flux of ^{8}B solar neutrinos independent from possible neutrino flavor changes related to oscillations [3]: this is a very important handle to solve the Solar Neutrino Problem. A significant deficit in ^{8}B neutrinos flux measured by the CC reaction with respect to the total flux measured by the NC interactions directly demonstrates that the Sun's electron neutrinos have been changing to one of the other active flavors.

The CC and ES reactions were detected by observing the cone of Čerenkov light produced by the electron in the final state. The electron produced by CC reaction can be distinguished from the one scattered in the ES process by exploiting the different $\cos\vartheta_\odot$ distribution. $\vartheta_\odot$ is the angle of the electron in the final state with respect to the incoming neutrino direction from the Sun. While the ES process has a strong forward peak, CC

events have an angular distribution going as $\sim 1 - 1/3 \cos\vartheta_{\odot}$. The signal of NC reactions is provided by neutron capture in deuterium, producing a 6.25 MeV photon. In order to improve the capture efficiency and to increase the total γ-ray energy, 2 t of NaCl were added to the heavy water in the second phase of the experiment. The measured ^{8}B neutrino fluxes from the first phase of measurement are (in units of 10^6 cm^{-2}s^{-1})[3]:

$$\phi_{CC} = 1.76^{+0.06}_{-0.05}(\text{stat.})^{+0.09}_{-0.09}(\text{syst.}) \tag{1.5}$$

$$\phi_{ES} = 2.39^{+0.24}_{-0.23}(\text{stat.})^{+0.12}_{-0.12}(\text{syst.}) \tag{1.6}$$

$$\phi_{NC} = 5.09^{+0.44}_{-0.43}(\text{stat.})^{+0.46}_{-0.43}(\text{syst.}) \tag{1.7}$$

The measurement by NC reactions of a total active neutrino flux in agreement with the Standard Solar Model and the inequality of the fluxes determined from the CC, ES and NC reactions provides a strong evidence for a non-ν_e component in the ^{8}B solar neutrinos. Figure 1.1 summarizes SNO's CC, NC and ES measurements. To make this fit, a change of variable was performed:

$$\phi_{CC} = \phi(\nu_e) \tag{1.8}$$

$$\phi_{ES} = \phi(\nu_e) + 0.1559\phi(\nu_{\mu\tau}) \tag{1.9}$$

$$\phi_{NC} = \phi(\nu_e) + \phi(\nu_{\mu\tau}) \tag{1.10}$$

where $\phi(\nu_{\mu\tau}) = \phi(\nu_\mu) + \phi(\nu_\tau)$. The factor of 0.1559 is the ratio of the ES cross section for ν_e and $\nu_{\mu\tau}$ for an effective kinetic energy $T_{eff} > 5$ MeV.

1.1.2 Super-Kamiokande

Super-Kamiokande (SK) is a solar and atmospheric neutrinos experiment started in 1996. SK is a water Čerenkov cylindrical detector containing 50 kt of ultra pure water. The detector is subdivided by an optical barrier into a cylindrical primary detector region (the Inner Detector, or ID) and a surrounding shell of water (the Outer Detector, or OD), serving as a cosmic-ray veto [4]. Both the Inner and Outer detector are equipped with photomultipliers capable to measure the Čerenkov light generated by the charged particles produced in neutrino CC interactions with the water nuclei (in the case of ID) or by cosmic-rays (mainly in the OD). The water Čerenkov technique had been pioneered by the smaller Kamiokande [5] and IMB [6] detectors which had been built for the proton decay search but highlighted the anomaly in the atmospheric neutrino fluxes which could be interpreted in terms of neutrino oscillations. Kamiokande also allowed for the first observation of neutrinos from the supernova 1987a and confirmed, at higher energy, the solar neutrino deficit observed by the Homestake chlorine experiment since 1968. These results were awarded by the 2002 Nobel Prize in Physics.

Events in SK are classified as *fully contained* events (FC), with no significant activity in the OD, and *partially contained* events (PC): events which have the vertex in the ID, but at least a primary particle exits the detector without releasing all its energy. Fully contained

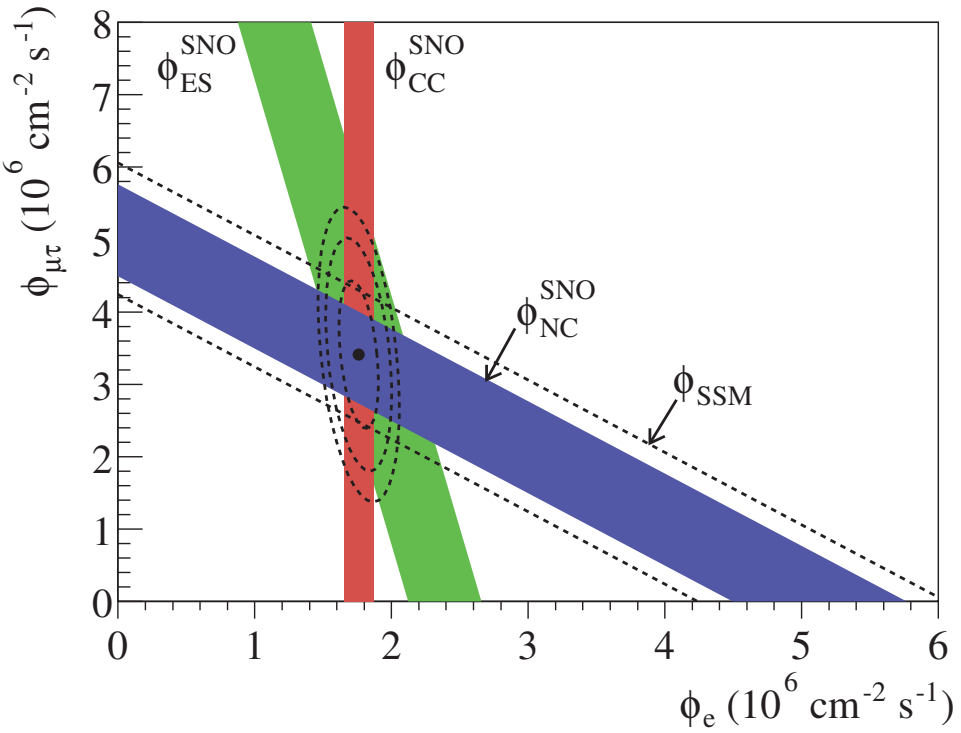

Figure 1.1: Flux of ^{8}B solar neutrinos which are μ or τ flavor vs flux of electron neutrinos deduced from the three neutrino reactions in SNO [3].

events can be further subdivided in two subsets, the so-called *sub-GeV* and *multi-GeV* events, with energies below and above 1.33 GeV respectively. Finally, *upward going* muons are produced by neutrino interactions in the rock below SK. Particle identification in SK is performed by using a likelihood function to parametrize the sharpness of the Čerenkov rings. These rings have well defined contours for muons while they are fuzzy for electrons.

SK observes a significant deficit in muon-like atmospheric neutrino events: this deficit is strongly zenith-angle dependent, as shown in Figure 1.2, with a large effect for upward-going muon neutrinos (negative $\cos\vartheta$) and little or no deficit for downward going neutrinos of either flavor. Downward-going neutrinos have travelled a distance $\sim$ 20 km or less, while upward-going neutrinos have travelled up to 13000 km through the earth. It has to be noticed that the sub-GeV muon sample is depleted over the entire spectrum; on the other hand, for the multi-GeV muons the spectrum of neutrino coming from above ($\cos\vartheta > 0$) is very little changed with respect to the prevision without oscillation. This is consistent with ν_μ oscillations occurring for low energy neutrinos (sub-GeV), while for high energy neutrinos the effect of oscillations becomes sizable only for a large baseline.

The distributions of electron neutrinos agree with the expected fluxes, while the distributions of muon neutrinos show a deficit which is dependent on the zenith angle and which is stronger for neutrinos which have been travelling over longer distances. Down-going

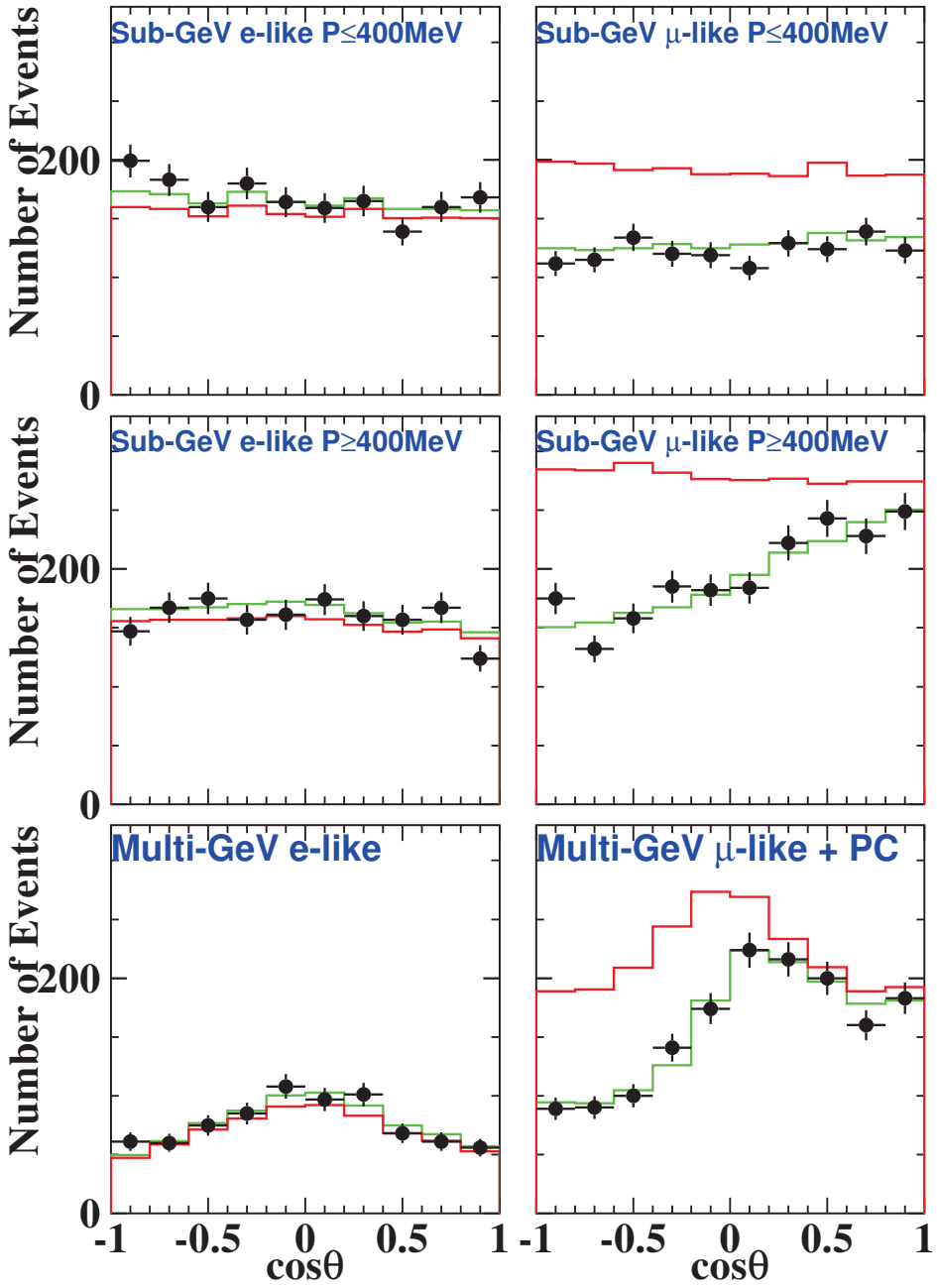

Figure 1.2: Atmospheric neutrino zenith angle distribution in SK (data points). Red lines represents the expectation for no oscillations, green line the expectation for best-fit oscillation parameters.

neutrinos which have been produced in the atmosphere just above the detector agree with the expected fluxes. The zenith angle measurement is a self-normalizing measurement and clearly shows a disappearance effect on muonic neutrinos which is dependent on the travelled path. This effect can be interpreted in terms of neutrino oscillations among muonic and tau neutrinos. The disappearance effect of muonic neutrinos in Super-Kamiokande was also reproduced with an artificial neutrino beam with the K2K experiment [7], which has been the first long-baseline experiment.

1.2 Oscillations

It is known that there are three active flavors of neutrino: ν_e, ν_μ and ν_τ. It is possible to define the neutrino of a given flavor in terms of the charged current interaction mediated by a W-boson exchange. This interaction produces a charged lepton, which may be an e, μ or τ. It is defined the ν_e as the neutrino interacting when the charged lepton in the final state is an e, the ν_μ as the neutrino producing a μ and the ν_τ as the one coupled with a τ. Several experiments (the most important are described above) have provided evidence for neutrino oscillations between the different flavors ν_e, ν_μ and ν_τ, caused by nonzero neutrino masses and neutrino mixing. It is possible to write the three flavor eigenstates ν_α ($\alpha = e,\, \mu\, \tau$) as a linear combination of the three mass eigenstates ν_i ($i = 1,\, 2,\, 3$), using the Pontecorvo-Maki-Nakagawa-Sakata (PMNS) [8, 9] matrix U as:

$$|\nu_\alpha\rangle = \sum_{i=1}^{3} U_{\alpha i} |\nu_i\rangle \tag{1.11}$$

U is a 3×3 unitary matrix generally parametrized by the three mixing angles θ_{12}, θ_{23} and θ_{13} and by the phase δ_{CP}:

$$\begin{aligned} U &= \begin{pmatrix} U_{e1} & U_{e2} & U_{e3} \\ U_{\mu 1} & U_{\mu 2} & U_{\mu 3} \\ U_{\tau 1} & U_{\tau 2} & U_{\tau 3} \end{pmatrix} \\ &= \begin{pmatrix} 1 & 0 & 0 \\ 0 & c_{23} & s_{23} \\ 0 & -s_{23} & c_{23} \end{pmatrix} \begin{pmatrix} c_{13} & 0 & s_{13}\, \mathrm{e}^{\imath\delta} \\ 0 & 1 & 0 \\ -s_{13}\, \mathrm{e}^{\imath\delta} & 0 & c_{13} \end{pmatrix} \begin{pmatrix} c_{12} & s_{12} & 0 \\ -s_{12} & c_{12} & 0 \\ 0 & 0 & 1 \end{pmatrix} \end{aligned} \tag{1.12}$$

where c_{ij} and s_{ij} represent $\cos\theta_{ij}$ and $\sin\theta_{ij}$, respectively. The parameter δ_{CP} is the phase that controls the CP asymmetry.

The probability that a neutrino generated in the flavor eigenstate ν_α can be observed

in the flavor eigenstate ν_β after a travelled distance L is given by:

$$\mathcal{P}(\nu_\alpha \to \nu_\beta) = \delta_{\alpha\beta} - 4\sum_{j>k} \Re\left\{U_{\alpha j}U^*_{\beta j}U^*_{\alpha j}U_{\beta k}\right\} \sin^2\left(1.267\frac{\Delta m^2_{jk}[\mathrm{eV}^2]L[\mathrm{km}]}{E_\nu[\mathrm{GeV}]}\right) + \\ + 2\sum_{j>k} \Im\left\{U_{\alpha j}U^*_{\beta j}U^*_{\alpha j}U_{\beta k}\right\} \sin\left(1.267\frac{\Delta m^2_{jk}[\mathrm{eV}^2]L[\mathrm{km}]}{E_\nu[\mathrm{GeV}]}\right) \quad (1.13)$$

where $\Delta m^2_{jk} = m^2_j - m^2_k$, with $m_{j,k}$ and E_ν is the neutrino energy.

In conclusion, neutrino oscillations are regulated by 7 parameters: 3 mixing angles (θ_{12}, θ_{23} and θ_{13}), one phase δ_{CP} and 3 masses squared differences (Δm^2_{12}, Δm^2_{23} and Δm^2_{31}). The sum of the 3 masses squared differences is zero so only 2 out of them are really independent parameters.

The "solar sector" is driven by θ_{12} and Δm^2_{21}: it has been measured by solar and reactor neutrino experiments (Chlorine, Gallex, SAGE, Super-Kamiokande, SNO, Borexino, KamLAND, CHOOZ, Palo-Verde, Double-Chooz, Daya-Bay, Reno). On the other hand, the "atmospheric sector", driven by θ_{23} and $|\Delta m^2_{23}|$ has been probed by atmospheric (Super-Kamiokande) and accelerator (MINOS, T2K, NOνA) neutrino experiments. Experimental data indicate that $\Delta m^2_{21} \ll |\Delta m^2_{31}| \simeq |\Delta m^2_{32}|$: the sign of Δm^2_{32} is not yet known: if ν_3, the mass eigenstate which has the largest ν_τ component, is the heaviest mass eigenvalue (normal hierarchy, NH, $\Delta m^2_{32} > 0$) or if ν_3 is the lightest one (inverted hierarchy, IH, $\Delta m^2_{32} < 0$) remains to be experimentally determined in the future: this is called the *mass hierarchy problem*. A schematic representation of two mass hierarchy cases is shown in Figure 1.3.

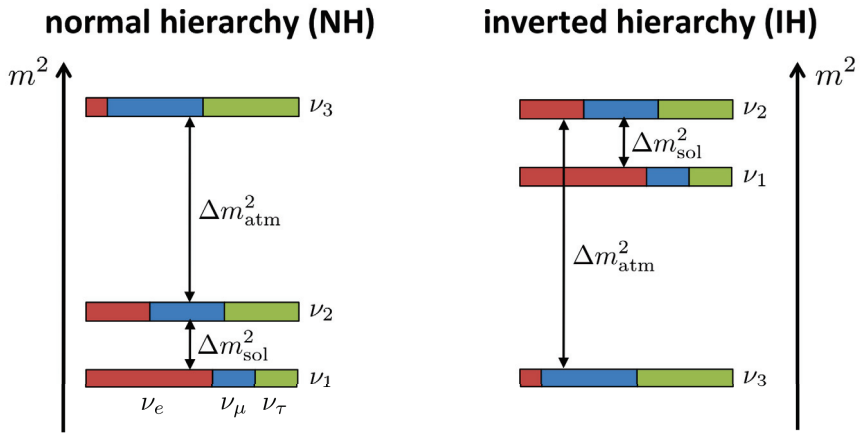

Figure 1.3: Normal hierarchy (NH) with $\Delta m^2_{32} > 0$ (left) and inverted hierarchy (IH) with $\Delta m^2_{32} < 0$ (right).

Recently, the reactor experiments Daya Bay [10], RENO [11] and Double-CHOOZ [12], have provided a precise measurement of θ_{13} by studying the disappearance effect of electron anti-neutrinos given by the sub-leading $\nu_\mu \to \nu_e$ oscillation in the atmospheric neutrinos domain.

The data sets collected by solar neutrino experiment (Chlorine [13], Gallex [14], SAGE [15], Super-Kamiokande [16, 17, 18, 19, 20], SNO [21] and Borexino [22, 23, 24]), long baseline accelerator experiments (MINOS [25, 26], T2K [27, 28], NOνA [29]), reactor experiments (KamLAND [30], CHOOZ [31], Palo Verde [32], Double Chooz [33], Daya-Bay [34], RENO [35]) have been analysed by NuFIT 3.0 [36]: the results of this analysis are shown in Figure 1.4 and all the values for the NH and IH are listed in Table 1.1.

	Normal Hierarchy	Inverted hierarchy
$\sin^2\theta_{12}$	$0.306^{+0.012}_{-0.012}$	$0.306^{+0.012}_{-0.012}$
$\sin^2\theta_{23}$	$0.441^{+0.027}_{-0.021}$	$0.587^{+0.020}_{-0.024}$
$\sin^2\theta_{13}$	$0.02166^{+0.00075}_{-0.00075}$	$0.02179^{+0.00076}_{-0.00076}$
δ_{CP} $(^\circ)$	261^{+51}_{-59}	277^{+40}_{-46}
$\frac{\Delta m^2_{21}}{10^{-5}\ \mathrm{eV}^2}$	$7.50^{+0.19}_{-0.17}$	$7.50^{+0.19}_{-0.19}$
$\frac{\Delta m^2_{3\ell}}{10^{-3}\ \mathrm{eV}^2}$	$+2.524^{+0.039}_{-0.040}$	$-2.514^{+0.038}_{-0.041}$

Table 1.1: Best fit values of NUFIT [36] from the fit to global data at 1σ. In the last raw $\Delta m^2_{3\ell} \equiv \Delta m^2_{31}$ for NH and $\Delta m^2_{3\ell} \equiv \Delta m^2_{32}$ for IH.

Despite the precision results obtained recently on neutrino oscillations parameters, several questions are still open, as why neutrino masses are so small, or why neutrino mixing angles are so large with respect to the quark mixing angles. Providing answers to these questions could give a key to explore new physics beyond the Standard Model.

The next experimental challenges in neutrino physics are to provide an absolute measurement of the lightest neutrino mass state, to determine the neutrino nature (*i.e.* if it is a Majorana or Dirac particle), to assess the mass hierarchy and to search for CP violation in the neutrino sector. This last subject could be needed to explain the matter-antimatter asymmetry in the Universe.

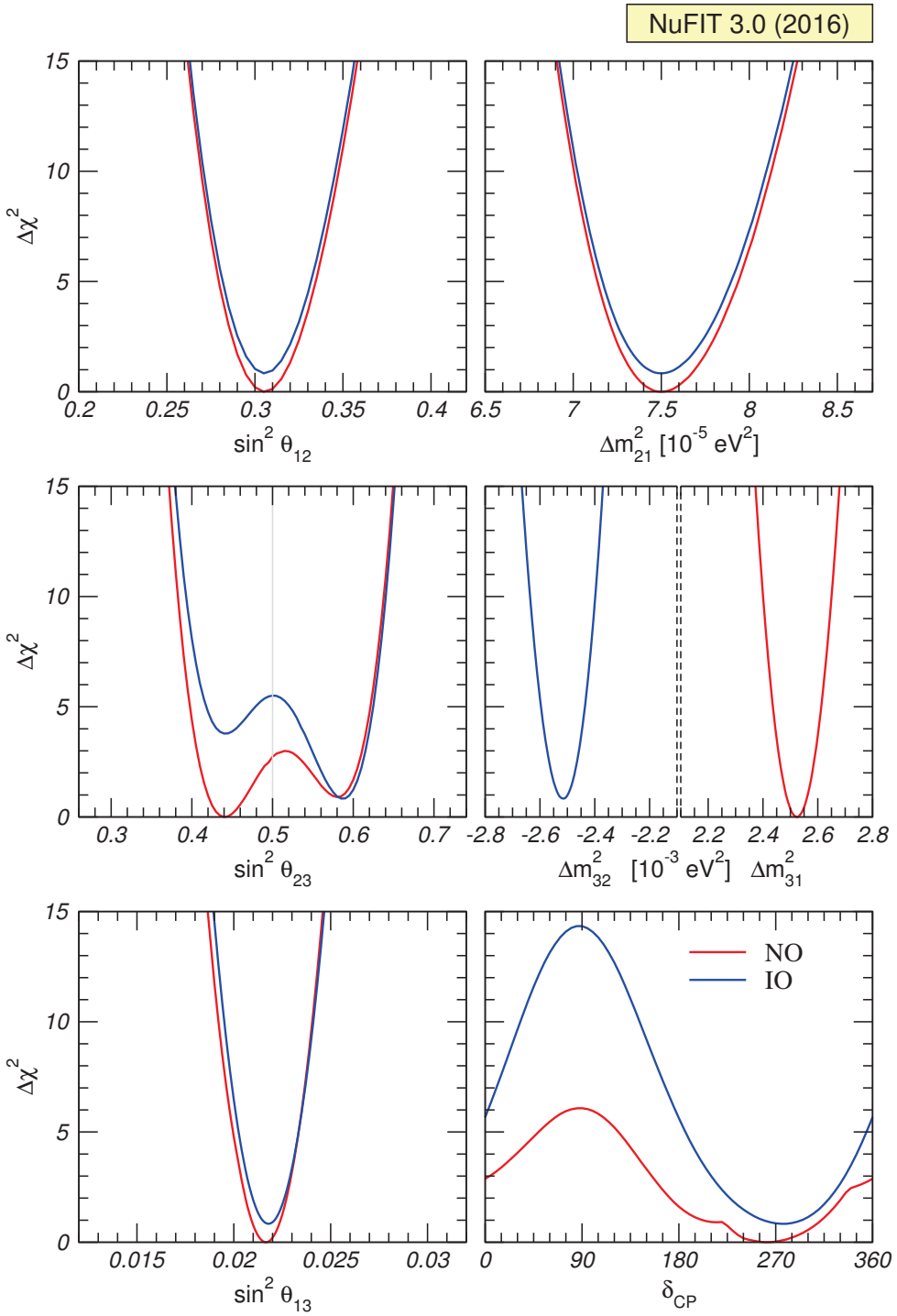

Figure 1.4: Global 3ν analysis. The red (blue) curves correspond to Normal (Inverted) Hierarchy [36].

1.3 CP violation

Thanks to the recent results about θ_{13}, corresponding to a high value just close to the upper limit which had been set by the CHOOZ experiment, it will be possible to perform studies on CP violation by using neutrino oscillations with conventional neutrino beams running at very high power. These beams are produced by shooting proton beams with a power of the order of a MW on a light target, producing many secondary charged pions. The pions exiting the target are then focused in a parallel beam and left decaying and producing mainly muonic neutrinos in a long pipe pointing in the direction of the far detector.

Assuming CPT conservation, direct evidence for CP-violation must be searched, as well as the determination of the mass hierarchy, by studying with high accuracy in appearance mode the sub-leading oscillations channel of atmospheric neutrino oscillations $\nu_\mu \to \nu_e$ (and $\overline{\nu}_\mu \to \overline{\nu}_e$) mainly governed by the parameter θ_{13}. The detection of a ν_e requires the detection of an electron out-coming from the interaction of the ν_e with the medium in the detector. It means that it is crucial to use a detector capable of providing very good performance in electron identification, energy resolution and background rejection.

Including higher order terms and the effects of neutrino oscillation in matter, $\nu_e \to \nu_e$ oscillations probability can be written in the following way [37]:

$$\begin{aligned}\mathcal{P}(\nu_\mu \to \nu_\mathrm{e}) = 4\sin^2\frac{\Delta m^2_{31}L}{4E}c^2_{13}s^2_{13}s^2_{23}\left\{1+\frac{a}{\Delta m^2_{31}}\cdot 2(1-2s^2_{13})\right\} \\ 2\frac{\Delta m^2_{31}L}{2E}\sin\frac{\Delta m^2_{31}L}{2E}c^2_{13}s_{13}s_{23}\left\{-\frac{a}{\Delta m^2_{31}}s_{13}s_{23}(1-2s^2_{13})+\right. \\ \left.+\frac{\Delta m^2_{21}}{\Delta m^2_{31}}s_{12}(-s_{13}s_{23}s_{12}+c_\delta c_{23}c_{12})\right\} \\ 4\frac{\Delta m^2_{21}L}{2E}\sin^2\frac{\Delta m^2_{31}L}{4E}s_\delta c^2_{13}s_{13}c_{23}s_{23}c_{12}s_{12} \quad (1.14)\end{aligned}$$

where $c_{ij} = \cos\theta_{ij}$, $s_{ij} = \sin\theta_{ij}$, $c_\delta = \cos\delta$, $s_\delta = \sin\delta$ and $a = 2\sqrt{2}G_F n_e E$, with G_F the Fermi constant, n_e the electron density of the traversed medium and E the neutrino energy. The corresponding probability for $\overline{\nu}_\mu \to \overline{\nu}_e$ is obtained by replacing $\delta_{CP} \to -\delta_{CP}$ and $a \to -a$.

It is useful to define the asymmetry $\mathcal{A}_{\mathcal{CP}}$ between the probability of oscillation of neutrino and antineutrino [37]:

$$\begin{aligned}\mathcal{A}_{\mathcal{CP}} \equiv (\mathcal{P}(\nu) - \mathcal{P}(\overline{\nu})) \\ = 16\frac{a}{\Delta m^2_{31}}\sin^2\frac{\Delta m^2_{31}L}{4E}c^2_{13}s^2_{13}s^2_{23}(1-2s^2_{13}) \\ -4\frac{aL}{2E}\sin\frac{\Delta m^2_{31}L}{2E}c^2_{13}s^2_{13}s^2_{23}(1-2s^2_{13}) \\ -8\frac{\Delta m^2_{21}L}{2E}\sin^2\frac{\Delta m^2_{31}L}{4E}s_\delta c^2_{13}s_{13}c_{23}s_{23}c_{12}s_{12} \quad (1.15)\end{aligned}$$

Calling $\Delta\mathcal{P}_1$ the first term in Equation (1.15), $\Delta\mathcal{P}_2$ the second one and $\Delta\mathcal{P}_3$ the third one, it is possible to make a distinction: $\Delta\mathcal{P}_1$ and $\Delta\mathcal{P}_2$, depending on a, are due to effect of the matter along the path travelled by neutrino. $\Delta\mathcal{P}_3$, which is proportional to $\sin\delta$, is due to the pure CP violation.

The matter asymmetry (*i.e.* $\Delta\mathcal{P}_1 + \Delta\mathcal{P}_2$) can disentangle the normal and inverted hierarchies by measuring neutrino and antineutrino events. Figure 1.5 shows the oscillations probability of $\nu_\mu \to \nu_e$ (blue line) and $\overline{\nu}_\mu \to \overline{\nu}_e$ (red-dashed line) for $L = 2300$ km. The plots show qualitatively that the spectral information provides an unambiguous determination of the mass hierarchy. Once the sign of Δm^2_{31} has been determined, matter effects which can interfere with the search for CP violation can be accurately subtracted and the same data sets of neutrinos and anti-neutrinos interactions can be used for the measurement of CP violation.

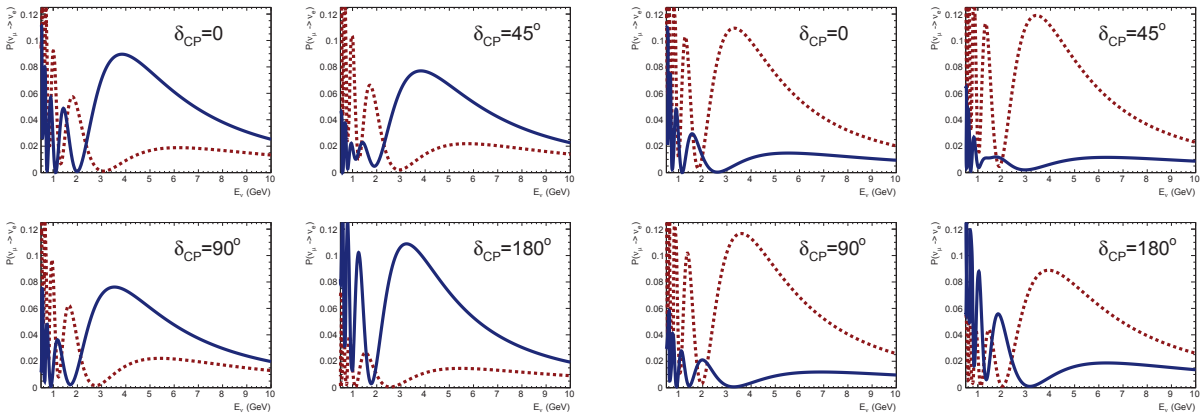

Figure 1.5: Oscillations probability of $\nu_\mu \to \nu_e$ (blue) and $\overline{\nu}_\mu \to \overline{\nu}_e$ (red-dashed) for different values of δ_{CP} for normal hierarchy (NH) $\Delta m^2_{31} > 0$ (left) and inverted hierarchy (IH) $\Delta m^2_{31} > 0$ (right) with $\sin^2 2\theta_{13} = 0.09$ and $L = 2300$ km [38].

Considering the energy dependence of a, it is possible to affirm that $\Delta\mathcal{P}_1/L$, $\Delta\mathcal{P}_2/L$ and $\Delta\mathcal{P}_3$ depend on the variable L/E alone: each term has a characteristic envelope, as shown in Figure 1.6. $\Delta\mathcal{P}_1/L$ decrease monotonously with the distance L, $\Delta\mathcal{P}_2/L$ is limited and $\Delta\mathcal{P}_3$ increases linearly. For large L/E the asymmetry $\mathcal{A}_{CP}$ is dominated by the term $\Delta\mathcal{P}_3$. The measurement of $\mathcal{A}_{CP}$ at large L/E is more sensitive to pure CP violating effects.

1.4 Deep Underground Neutrino Experiment

The Deep Underground Neutrino Experiment (DUNE) is a joint European-USA neutrino physics program which has as goals the measurement of the still unknown parameters of the neutrino mixing matrix and the search for new phenomena.

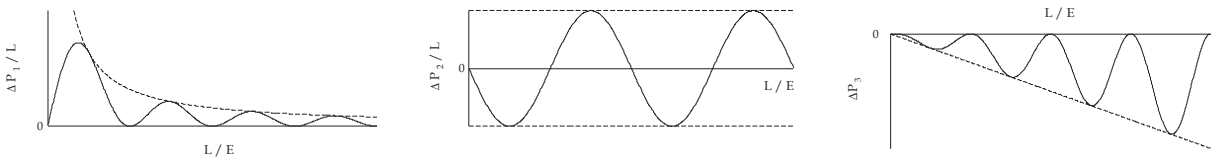

Figure 1.6: Matter effect term $\Delta\mathcal{P}_1/L$ (left), $\Delta\mathcal{P}_2/L$ (center) and $\Delta\mathcal{P}_3$ (right) as a function of the ratio L/E.

The DUNE far detector will be a 40 kt modular Liquid Argon Time Projection Chamber neutrino target located at the Sanford Underground Research Facility in South Dakota, at a distance of 1300 km from Fermilab. The PIP-II proton accelerator at Fermilab will produce a new neutrino beam-line at Fermilab with a beam power of 1.2 MW, with a planned upgrade of the accelerator complex designed to provide up to 2.4 MW of beam power by 2030 [39].

The primary goals of this experiment are:

- precision measurement of the parameters that govern $\nu_\mu \to \nu_e$ and $\overline{\nu}_\mu \to \overline{\nu}_e$ with the aim of measuring the CP violation phase δ_{CP}, determining the neutrino mass hierarchy and performing precision tests of the three flavor neutrino oscillation paradigm;
- search for proton decay in several important decays modes, for example $p \to K^+\overline{\nu}$: the observation of proton decay would represent a direct evidence of new physics expected at the Grand Unification scale;
- detection and precise measurements of the neutrinos from a core-collapse supernova within our galaxy.

In Figure 1.7 are shown the electron neutrino (left) and antineutrino (right) appearance probabilities as a function of neutrino energy for several values of δ_{CP} at a baseline of 1300 km. It is interesting to observe how different values of δ_{CP} change the shape of the observed oscillatory pattern. The difference in probability amplitude for different values of δ_{CP} is more important, at larger L/E around the second oscillation maximum, for energies lower than 1.5 GeV. It means that the DUNE far detector should be capable to observe oscillations down to energies of at least 500 MeV.

As mentioned above, the neutrino oscillation channels studied to search CP violation effects are $\nu_\mu \to \nu_e$ and $\overline{\nu}_\mu \to \overline{\nu}_e$: the detector used for this experiment has to be capable to detect electron neutrinos. To do this the interaction exploited is the ν_e CC interaction. Figure 1.8 shows possible Feynman diagrams for this interaction. On the left is shown a quasi-elastic scattering: this is the most probable interaction for low neutrino energies below 1 GeV: the neutrino interacts with a neutron of the argon nucleus and the final state includes a proton and an electron.

Other possible ν_e CC interactions at low energy go via the production of resonances. As example it is shown the resonant production of Δ^+ (Figure 1.8 center), which consequently

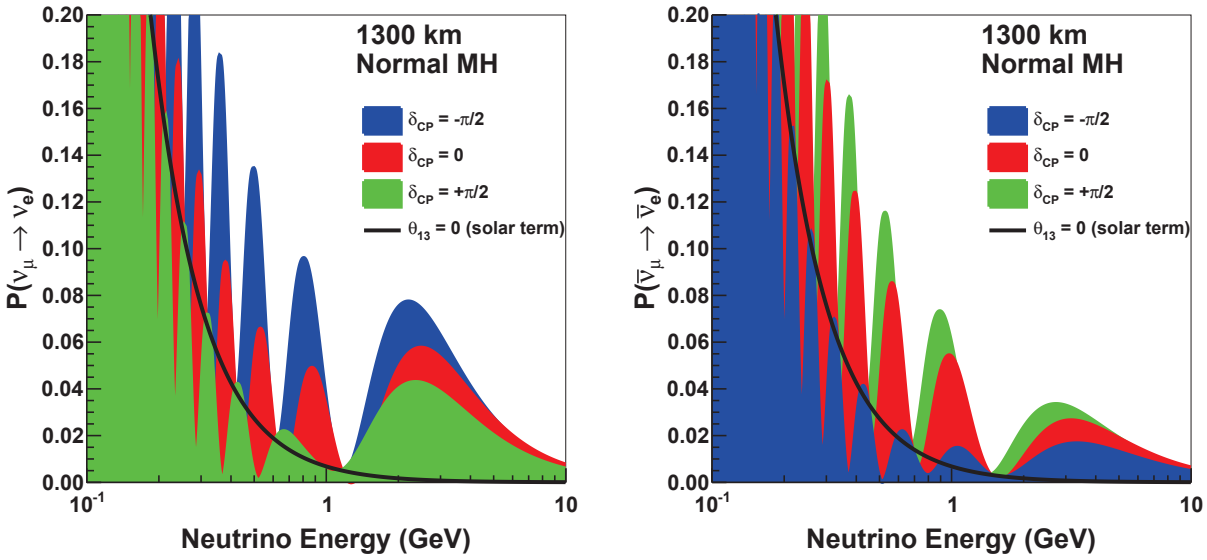

Figure 1.7: The appearance probability at a baseline of 1300 km, as a function of neutrino energy, for $\delta_{CP} = -\pi/2$ (blue), 0 (red), and $\pi/2$ (green), for neutrinos (left) and anti-neutrinos (right), for normal hierarchy. The black line indicates the oscillation probability if θ_{13} were equal to zero [39].

decays in π^0 and proton. The final state includes an electron, a π^0 and a proton. Finally at higher energies electron neutrinos mainly interact with argon nuclei via CC deep inelastic scattering interactions (Figure 1.8 right), producing in the final state an electron and several particles coming from the hadronization process of the struck quark and spectator quarks system.

In all these processes the electron detection proves the presence of an incoming electron neutrino while an accurate measurement of the electron energy and of the energy of the other particles in the final state are essential for the measurement of the impinging neutrino energy.

The background to the study of $\nu_\mu \to \nu_e$ oscillations is represented by all the processes which may produce electrons or other particles possibly misidentified as electrons in a final state characteristic of ν_e charged current interactions.

An important background source is represented by the small fraction of electron neutrinos already present in the neutrino beam at its production. These electron neutrinos (and anti-neutrinos) are produced by muon (or anti-muon) decays following the decays of the pions or by 3 body decays of charged kaons produced at the same time as the pions in the target. The intrinsic beam contamination in terms of electron neutrinos represents a background to the electron neutrinos component coming from the oscillation of muonic neutrinos. It must be accurately measured with a near detector, extrapolated to the far detector and subtracted from the analysis sample.

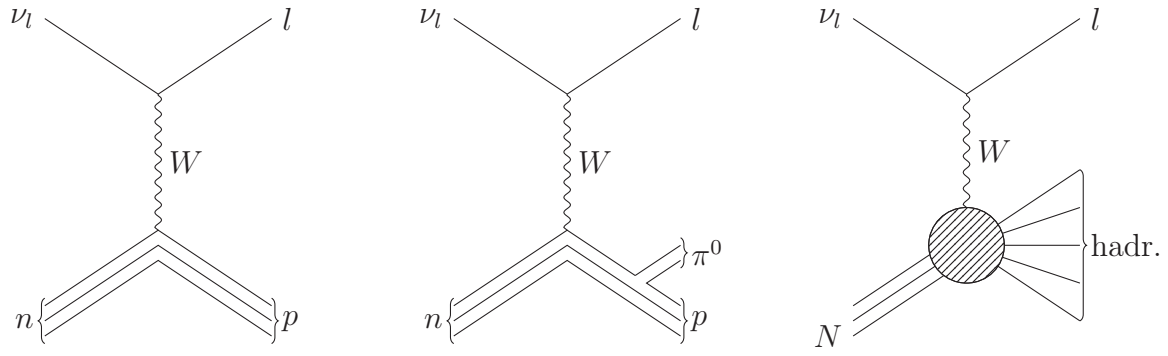

Figure 1.8: Feynman diagrams for three ν CC scattering: quasi elastic (left), resonance with Δ^+ production (center) and deep inelastic scattering (right).

Muonic neutrinos can have NC interactions with the argon nucleus, giving in the final state a muon neutrino (non detectable) and other hadronic particles which could generate electromagnetic showers, as the π^0 which decays in a pair of photons: the shower initiated by the conversion of one of the two photons could be misidentified as a shower originated by a primary electron at the neutrino interaction vertex. Also CC interactions of muonic neutrinos with muon mis-identification can contribute to this background.

Finally a small contribution to the background is given by the CC interactions of ν_τ (or $\overline{\nu}_\tau$), coming from the leading oscillation mechanism in the atmospheric neutrinos sector, which produce τ that decay into an electron and two neutrinos.

In Figure 1.9 are shown the expected rates for ν_e appearance, including expected flux, cross section and oscillation probabilities as a function of neutrino energy at a baseline of 1300 km. The spectra are shown for a 150 kt MW year exposure each for neutrino and anti-neutrino beam mode, for a total 150 kt MW year exposure. The signal is composed by ν_e and $\overline{\nu}_e$ CC events. The background is represented by ν_e and $\overline{\nu}_e$ CC events from the beam, NC events, $\nu_\mu + \overline{\nu}_\mu$ $\nu_\tau + \overline{\nu}_\tau$ CC events

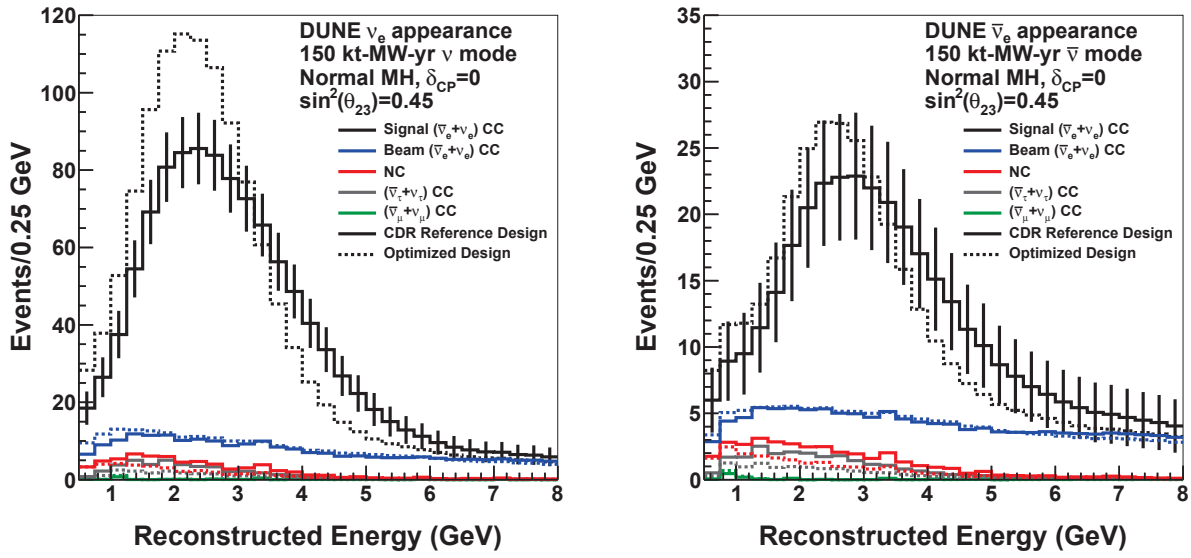

Figure 1.9: Reconstructed energy distribution of selected ν_e CC-like events assuming a 150 kt MW year exposure in the neutrino-beam mode (left) and anti-neutrino beam mode (right), for a total 300 kt MW year exposure. The plots assume normal mass hierarchy and $\delta_{CP} = 0$ [39].

Chapter 2

Liquid Argon Time Projection Chamber (LAr TPC)

The original idea of a Liquid Argon Time Projection Chamber (LAr TPC) was proposed by C. Rubbia in 1977 [40].

The Time Projection Chamber is a detector which provides a large amount of detailed information on the topology of the events, like a bubble chamber. In addition, when filled with liquid argon, it allows reaching large massive target volumes. Liquid argon can be considered an ideal target material as medium in a TPC because it is dense ($\rho = 1.39$ g/cm^3) and having vanishing electronegativity it does not reabsorb the electrons created by ionizing radiation. In addition it has a high electron mobility and it allows drifting ionization electrons with a high drift speed (2 mm/μs at 1 kV/cm) and small diffusion ($<$ 1 mm for 1 m) over large distances up to several meters without significant degradation of the imaging quality. Liquid argon is also easy to obtain from the distillation of air where it is present at 1% level, it is therefore relatively cheap and available in large quantities.

In a gas TPC with charge readout based on Multi-Wire Proportional Chambers (MWPC) the ionization signal is amplified at the end of the drift volume in avalanches occurring in proximity of the readout wires of the MWPC. Instead a LAr TPC with wires readout works as a ionization chamber, since no charge multiplication is possible around the wires at the electric field values normally achievable in LAr due to the short mean free path of the electrons. The ionization collected by the wires must be then amplified by the readout electronics in order to produce practically exploitable signals. Despite the use of low noise amplifiers with an Equivalent Noise Charge (ENC) around 1000 electrons the typical signal to noise ratio of a readout channel, for a particle at the ionization minimum, corresponds to $S/N \sim 10$. A new technique called *dual-phase Liquid Argon Time Projection Chamber* (DP LAr TPC) introduces multiplication in the vapor phase present above the liquid phase: in this way it is possible to increase the signal collected by the readout charge system located at the top of the detector: this allows obtaining typical $S/N \sim 100$.

This Chapter provides a general description of the LAr TPC and describes the physical processes involved in a dual-phase LAr TPC, whose knowledge is fundamental for the charge readout analysis. First a conceptual description of a LAr TPC is given. Then

the ionization process is presented, describing also recombination effects and the light production processes. Subsequently the dual-phase concept is presented: the electrons extraction process from the liquid to the gas phase and the charge readout are described. Finally a comparison between the dual-phase and the single-phase designs is shown, and the future dual-phase detectors are described.

2.1 Basic concept of a Liquid Argon Time Projection Chamber

The Time Projection Chamber was invented by Nygren in the 1970s [41]. A uniform electric field $\mathcal{E}$, drifts the clouds of electrons produced along the tracks of charged particles traversing a detection medium, either gas or liquid, towards the side surface of the active volume segmented into 2D readout electrodes. The field uniformity is in practise defined by a cathode and an anode planes separated by a field cage with external rings at degrading voltages corresponding to the equipotential surfaces. The knowledge of the constant drift velocity (related to the electric field) and the measurement of the drift time provide the coordinate perpendicular to the 2D readout plane making possible a full 3D measurement of the particle trajectory. This makes the TPC the only tracking detector where for each point of a particle track the three spatial coordinates can be measured simultaneously with high spatial resolution. In Figure 2.1 is shown a schematic representation of a TPC.

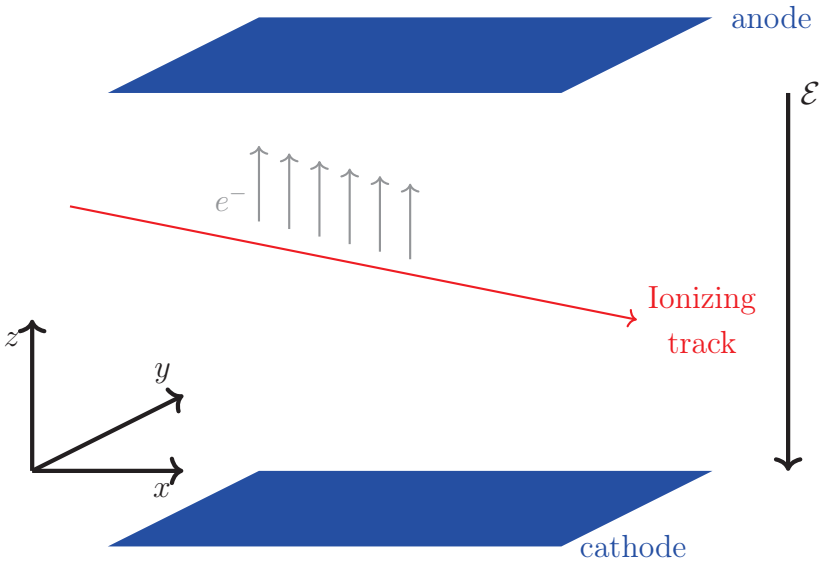

Figure 2.1: Schematic representation of a Time Projection Chamber. An electric potential difference is applied between the anode and the cathode, in order to create a uniform electric field $\mathcal{E}$. The electric field drifts ionization electrons to the anode plane.

In Figure 2.2 it is shown an example of ν_μ CC interaction in the ICARUS LAr TPC. The detector is capable to provide a very detailed view of the charged particles coming out from the primary vertex (on the right of the Figure) and the subsequent particle generation. It also allows to identify each type of particles in the event and to characterize them.

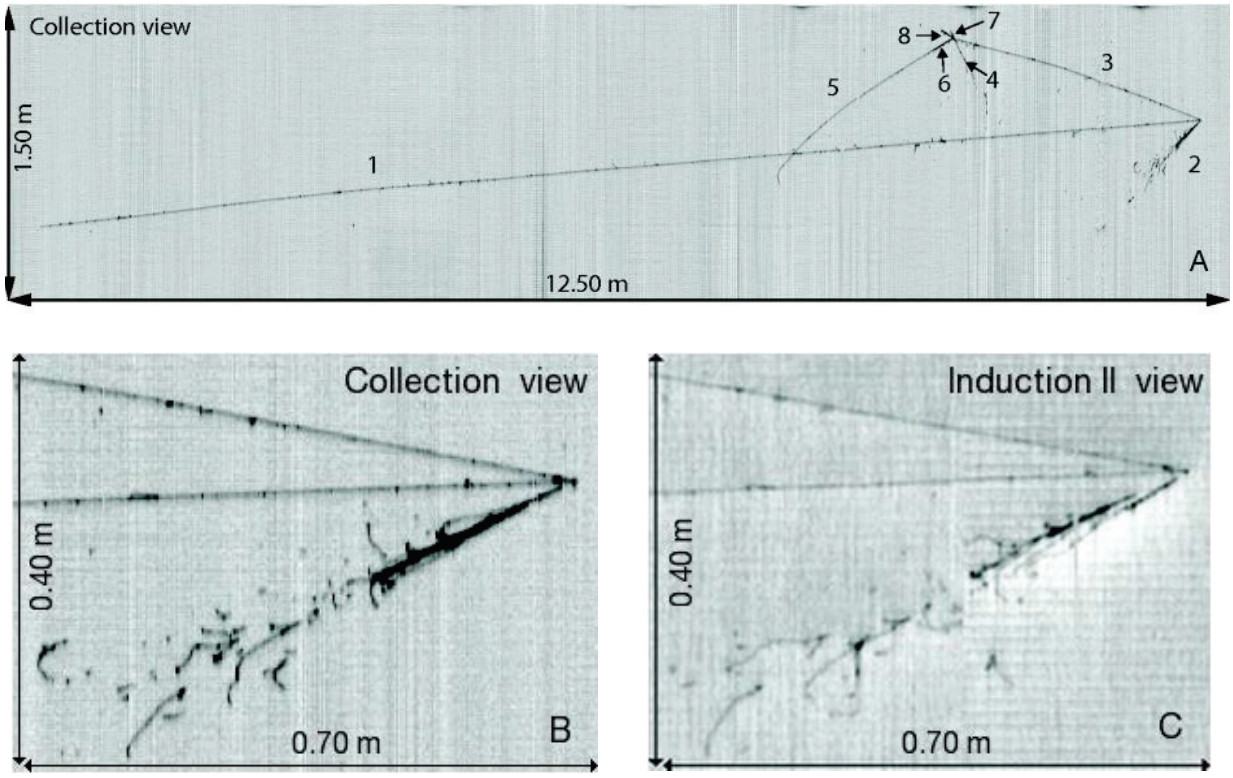

Figure 2.2: Top: an example of ν_μ CC interaction in ICARUS TPC. It is possible to recognize a muon (1), an electromagnetic shower originating by a photon from π^0 decay (2), a π (3) having a secondary hadronic interaction and generating multiple tracks (4-8) among which a a kaon (6) decaying in μ (5) then decaying in an electron. [42]. Bottom: a close-up view of the primary vertex for the Collection (left) and Induction-2 (right) projections allow solving completely the event topology.

The LAr TPC is also a very good calorimeter for completely contained events where all particles in the final state dissipate their energy inside the active volume by ranging out or by producing hadronic showers (in the case of hadrons) or electromagnetic showers (in the case of electrons or photons).

Furthermore the collected charge in the segmented readout system allows measuring the specific energy losses ($\mathrm{d}E/\,\mathrm{d}x$) of the ionizing particle (see Section 2.2). It is then possible to perform also particle identification.

Figure 2.3 shows particle identification by measuring the energy losses in a gas TPC,

in a LAr TPC it is possible to perform similar measurements for particle identification, as it will be shown later.

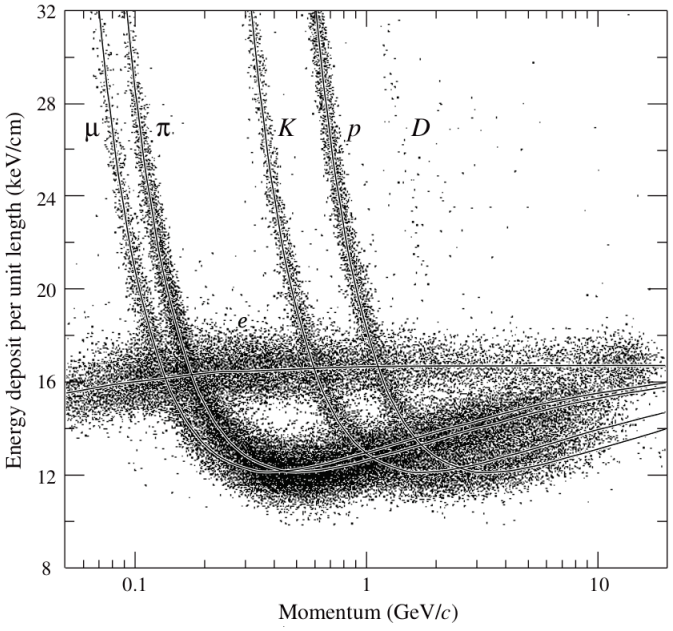

Figure 2.3: The PEP4/9-TPC energy deposit measurements (185 samples, 8.5 atm Ar-CH_4 80 : 20) [43].

2.2 Ionization process

When a moderately relativistic charged heavy particle travels through the detector medium, it looses its energy via collisions with the electrons of the medium atoms. The mean rate of energy loss is well-described by the *Bethe equation* [44] (for details see Chapter 4).
The energy deposited by travelling particles generates electron-ion pairs. Except for of very strong ionization, the total amount of electrons produced by the ionization depends linearly on the energy deposited by the travelling particle. The relation between the total charge Q produced by an energy deposition E is given by the relation:

$$Q = \mathcal{R}\frac{E}{W_{ion}} \tag{2.1}$$

where $\mathcal{R}$ is the recombination factor (a detailed explanation is given later) and W_{ion} is the average ionization energy (in the case of liquid argon $W_{ion} = 23.6$ eV). An incoming particle at m.i.p. has an average energy loss $\langle \mathrm{d}E/\,\mathrm{d}x\rangle_{m.i.p.} = 2.096$ MeV/cm; the number of electrons produced in 3 mm before the recombination is 26644.

2.2.1 Recombination

Several models have been developed on the local recombination of the electrons and the ions occurring immediately after ionization but none of those describes all the experimental data in liquid argon. However these models provide the basis for its understanding and for all phenomenological approaches.

$\mathcal{R}$ represents the fraction of the produced ionization charge which do not recombines; it depends on the applied electric field $\mathcal{E}$ and on the density of the initial ionization. This dependence is usually expressed as a function of the mean energy losses $\mathrm{d}E/\,\mathrm{d}x$ for the ionizing particle.

The Onsager theory [45] is based on the concept of "initial recombination" of the electron-ion pairs. The limit of this model is that it does not take into account the dependence on the ionization density: it explicitly assumes a single electron-ion pair. A better description of the measured data is given by Jaffé [46]: the assumption of this model is that the initial ionization charge is distributed in a column around the trajectory of the ionizing particle. Other models [47] are based on the columnar theory, with different assumptions. All these models assume a direct proportionality between the electron drift velocity and the applied electric field: this approximation is not true in liquid argon electric fields higher than 100 V/cm.

Usually, Jaffé formulation is approximated by the so called Birks law [48]:

$$\mathcal{R} = \frac{A}{1 + \dfrac{k}{\mathcal{E}} \dfrac{\mathrm{d}E}{\mathrm{d}x}} \tag{2.2}$$

with $A = 0.800 \pm 0.003$ and $k = 0.0486 \pm 0.0006$ (kV/cm)(g/cm^2)/MeV, as measured by the ICARUS collaboration [49]. This parametrization is valid in the range $0.1 < \mathcal{E} < 1.0$ kV/cm and $1.5 < \mathrm{d}E/\,\mathrm{d}x < 30$ MeV/(g/cm^2) and it will be used for all the calculations performed in this thesis work. Figure 2.4 shows the inverse of the recombination factor as a function of $\mathrm{d}E/\,\mathrm{d}x$ with the data taken with the 3 ton ICARUS TPC. It is possible to note that a greater electric field $\mathcal{E}$ gives larger $\mathcal{R}$ values, *i.e.* a greater number of electrons available to drift.

For a minimum ionising particle in LAr, in a drift electric field $\mathcal{E} = 1$ kV/cm, about 25% of the produced ionisation electron-ion pair undergo recombination ($\mathcal{R}_{mip} = 0.75$). This means that if a particle at the ionization minimum produces 26644 electrons in 3 mm (as stated above) the total number of electrons which survive to recombination is 19983: this is the amount of electrons which are then drifted towards the anode by the electric field.

2.2.2 Scintillation

The ratio of ion-electrons pairs which recombine $(1 - \mathcal{R})$ contributes to the scintillation process. The basis of the scintillation process in LAr is the formation of excited dimers (*excimers*) Ar_2^*. There are two ways to produce the excited dimers [50]:

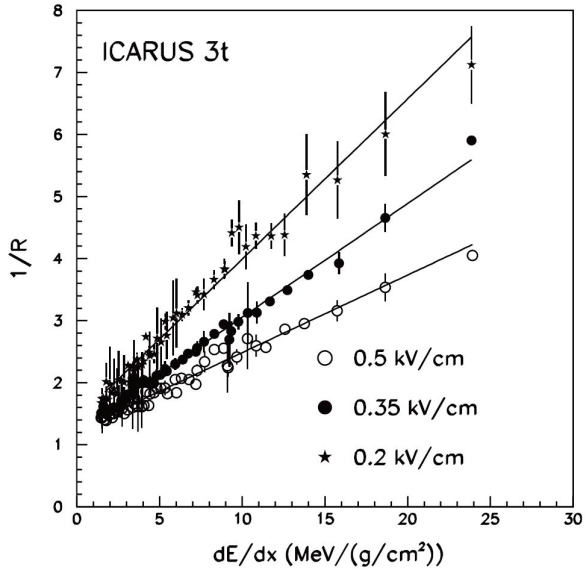

Figure 2.4: Birks fit of the inverse of the recombination factor as a function of stopping power. Data are from the 3 ton prototype of ICARUS at different electric fields [49].

- by *excitation*: it leads through collisions with neighbouring atoms to neutral excimers Ar_2^* which decay radiatively into two argon atoms:

$$\begin{aligned} Ar^* + Ar &\rightarrow Ar_2^* \\ Ar_2^* &\rightarrow 2Ar + h\nu \end{aligned} \tag{2.3}$$

- by *ionization*: it leads to the formation of charged excimers which are neutralized by electrons generated during the ionization process and that have not recombine:

$$\begin{aligned} Ar^+ + Ar &\rightarrow Ar_2^* \\ Ar_2^* + e &\rightarrow Ar^{**} + Ar \\ Ar^{**} &\rightarrow Ar^* + \text{heat.} \\ Ar^* + Ar &\rightarrow Ar_2^* \\ Ar_2^* &\rightarrow 2Ar + h\nu \end{aligned} \tag{2.4}$$

where $h\nu$ is an ultraviolet photon and the process $Ar^{**} \rightarrow Ar^* + \text{heat.}$ corresponds to a non-radiative transition.

The argon excimers are created in three nearly degenerate spin states, two singlets ($^1\Sigma_u^-$ and $^1\Sigma_u^+$) and a triplet ($^3\Sigma_u^+$). The $^1\Sigma_u^-$ can not decay radiatively by parity conservation, and $^3\Sigma_u^+$ is expected to have a much longer lifetime than the $^1\Sigma_u^+$ since it has to decay into two spin-0 argon atoms [51]. The photons produced have then two characteristic time constants (fast and slow component) of $\tau_f \approx$ ns and $\tau_s \approx 1.6$ μs.

The wavelength of these photons is the same, and it is peaked in a ≈ 10 nm band at 128 nm. These photons are not absorbed by atomic argon and can be detected and used as a prompt trigger for an interaction occurring in the active volume.

To detect the scintillation light cryogenic photomultiplier tubes (PMTs) are installed in the bottom part of the chamber, under the cathode. The 128 nm wavelength is not detectable by standard PMTs: it is necessary to shift the wavelength to the visible range. This is possible by using a wavelength shifter, as described in [52]: coating the PMT window with the wavelength shifter *Tetraphenyl-Butadiene* (TPB), it is possible to shift the wavelength from 128 nm to ≈ 400 nm.

Since the fast scintillation time constant is several orders of magnitude smaller than the typical electrons drift time which is sampled in units of 400 ns, the scintillation light provides the absolute time of an event (t_0), making the LAr TPC a self-triggering device.

2.3 Drift and diffusion processes

The accuracy of the drift coordinate depends on the measurement of the drift time t_d, *i.e.* the time between t_0 (described above) and the time when the drift electrons reach the readout plane, and on the accuracy on the knowledge of the drift velocity v_d. The drift velocity depends primarily on the electric field $\mathcal{E}$; the temperature of liquid argon can influence at a lower level the drift velocity. In addition, the presence of molecules in the liquid, such as carbon hydroxides, can increase v_d. On the other side, electronegative impurities like oxygen do not change the drift velocity. Walkowiak [53] performed a very accurate measurement of drift velocity in liquid argon for an electric field in the range 0.5 kV/cm $\leq |\mathcal{E}| \leq$ 12.6 kV/cm and temperatures in the range 87 K $\leq T \leq$ 94 K. The empirical polynomial function which fitted the data points is:

$$v_d(T,\ |\mathcal{E}|) = (P_1(T - T_0) + 1)\left(P_3|\mathcal{E}|\ln\left(1 + \frac{P_4}{|\mathcal{E}|}\right) + P_5|\mathcal{E}|P^6\right) + P_2(T - T_0) \qquad (2.5)$$

where T_0 is the reference temperature and the parameters P_1, P_2, P_3, P_4, P_5, P_6 are obtained from the fit. All the parameters values are reported in Table 2.1.

As said above, the presence of electronegative impurities, like oxygen molecules, does not influence v_d, but reduces the number of drifting electron. A fundamental requirement for the performance of a LAr TPC is to collect a maximum number of ionisation electrons since the output signal depends on the quantity of charge deposited on the readout planes. The number of electrons for a particle at the ionization minimum is already small at the production level after recombination. When compared to the readout electronics noise it is about a factor 10 larger. Thus, the purity of the medium is crucial in order to limit additional losses and possible contamination has to be kept at an extremely low level.

It is possible to describe the number of surviving charge $Q(t_d)$ after the drift time t_d by the following differential equation:

$$\frac{\mathrm{d}Q(t)}{\mathrm{d}t} = -k_s N_s Q \qquad (2.6)$$

Parameter	Value
P_1	-0.01481 ± 0.00095 K^{-1}
P_2	-0.0075 ± 0.0028 K^{-1}
P_3	0.141 ± 0.023 (kV/cm)$^{-1}$
P_4	12.4 ± 2.7 (kV/cm)
P_5	1.627 ± 0.078 (kV/cm)^{P_6}
P_6	0.317 ± 0.021 K^{-1}
T_0	90.371 ± 0.00095 K

Table 2.1: Result of the fit of parametrization using equation (2.5).

where k_s is the impurity attachment rate constant and N_s is the impurity concentration. Assuming that N_s remains constant, the solution of Equation (2.6) is

$$Q(t_d) = Q_0 \, \mathrm{e}^{-\frac{t_d}{\tau_e}} \tag{2.7}$$

where Q_0 is the initial charge produced by ionization and τ_e is the electron lifetime and it is related to the rate constant and the impurities by

$$\tau_e = \frac{1}{k_s N_s} \tag{2.8}$$

Assuming that all the impurity is oxygen, for electric field up to ≈ 1 kV/cm, Equation (2.8) can be written as [54]:

$$\tau_e[\mu\mathrm{s}] \approx \frac{300}{\rho_{O_2}[\mathrm{ppb}]} \tag{2.9}$$

where ρ_{O_2} is is the amount of impurities of oxygen with respect to the amount of argon. This implies that a level of impurity of 0.1 [ppb] give an electron lifetime $\tau_e \approx 1$ ms. Figure 2.5 shows the charge attenuation for different electron lifetimes and two drift field values 0.5 kV/cm and 1.0 kV/cm. In the case of WA105, for a 3 ms lifetime or 100 ppt O_2 equivalent contamination the maximal charge attenuation is ≈ 0.3 at the nominal 0.5 kV/cm drift field strength [55]. The figure of 3 ms lifetime is conservative, larger lifetimes values (up to 12 ms) have been obtained by ICARUS [56] and Microboone [57].

A point-like charge deposition will spread during the drift due to diffusion effects The magnitude of the charge spread depends on the drift time t_d. The size of the electron cloud arriving at the anode in the longitudinal (along the drift direction) and transverse direction follows a bi-dimensional Gaussian distribution:

$$Q(r,\, z) = Q_f \, \mathrm{e}^{-z^2/(4D_L t_d)} \, \mathrm{e}^{-r^2/(4D_T t_d)} \tag{2.10}$$

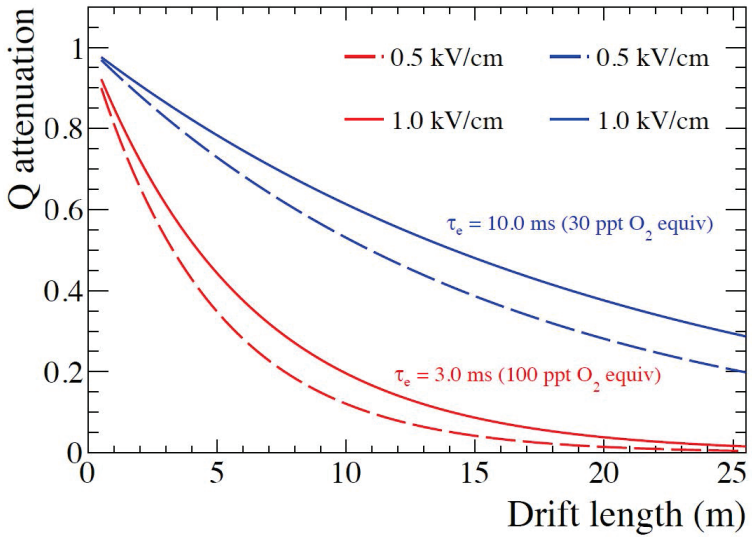

Figure 2.5: Electron survival probability as a function of drift distance for different electric field strengths and purity conditions [55].

where Q_f is the final charge after the drift (given by Equation (2.7)), $r = \sqrt{x^2 + y^2}$ and D_L, D_T are respectively the coefficient for longitudinal and transverse diffusion.

As shown in Figure 2.6 the diffusion coefficients depend on the electric field. It is interesting to note that for low electric fields the diffusion in the transverse direction is almost one order of magnitude bigger than the one in longitudinal direction.

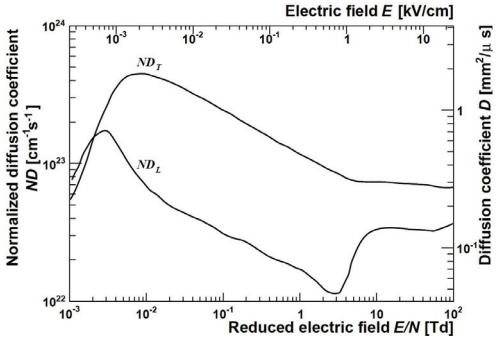

Figure 2.6: The normalized longitudinal and transverse diffusion coefficient ND for gaseous argon [58]. The Figure is normalized to a reduced electric field E/N with Townsend unit (Td = $[E/N] = 10^{-17}$ Vcm^2, where $\mathcal{E}$ is the electric field and N the molecular density).

For electrons in liquid argon, the ratio between the diffusion coefficient D and the

mobility μ is given by the Einstein's relation:

$$\frac{eD}{\mu} = kT = \frac{2}{3}\langle\varepsilon\rangle \tag{2.11}$$

where e is the electron charge, k is Boltzmann's constant, and T is the electron temperature. Figure 2.7 shows the ratio eD/μ as a function of the electric field [59]. These data are fitted with a simple power law, $eD/\mu = 0.064 \cdot \mathcal{E}^{0.77}$, where $\mathcal{E}$ is the electric field in kV/cm.

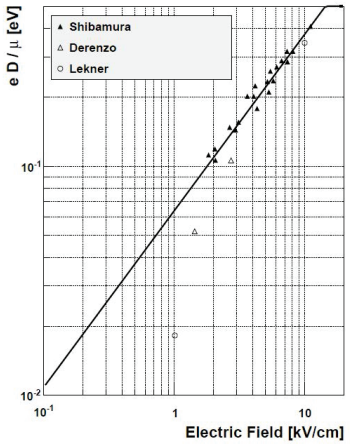

Figure 2.7: Field dependence of the ratio eD/μ in liquid argon [59].

In Figure 2.8 are reported the longitudinal (left) and the transverse (right) size of the electron cloud as a function of the drift distance. The calculation is based on the following values of the diffusion coefficients: $D_L = 4$ cm^2/s and $D_T = 13$ cm^2/s and $\mathcal{E} = 0.5$ kV/cm. There are large experimental uncertainties on these coefficients, direct measurements are planned with the WA105 detector.

The longitudinal diffusion is shown in time units (μs) to reflect the fact that the charge will be spread between nearby time bins in a given channel. The transverse diffusion is shown in mm unit as the original charge is shared among adjacent channels. In the case of WA105, for a 6 m drift, σ_T is comparable to the readout pitch of 3 mm.

2.4 Dual-phase readout

Since for a LAr TPC it is crucial to have a large amount of ionization electrons reaching the readout plane, in order to build detectors with long drift regions it has been developed a novel readout technique called dual-phase (liquid-vapor) Liquid Argon Time Projection Chamber (DP LAr TPC). The basic idea is to drift the ionization electrons from the liquid into the vapor phase, where they can be further multiplied. The original idea of a dual-phase detector was developed in 1970s by Dolgoshein and others [60]. A detailed study

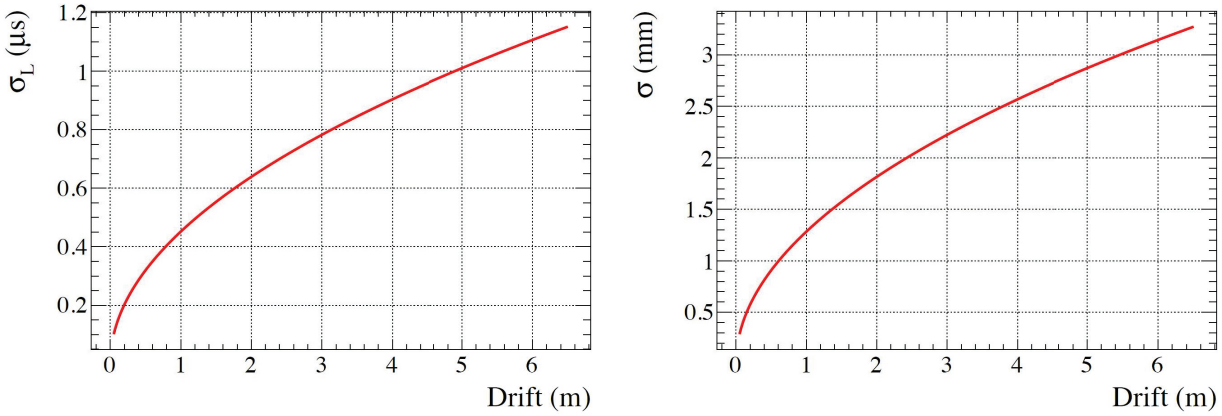

Figure 2.8: Size of the diffusion $\sigma = \sqrt{2Dt_d}$ along (left) and transverse (right) to the drift direction as a function of the drift distance for $D_L = 4$ cm^2/s, $D_T = 13$ cm^2/s and $\mathcal{E} = 0.5$ kV/cm [55]. The longitudinal diffusion σ_L is shown in time units.

about the emission of "hot" electrons was performed by Gushchin and others [61]: the extraction happens by applying across the interface liquid-vapor an electric field produced by two electrodes of which one has to be a submersed grid. They observed that an electric field $\mathcal{E}_{ext} \gtrsim 2.5$ kV/cm gives an extraction efficiency close to 100%.

2.4.1 Large Electron Multiplier (LEM)

After the extraction of the electrons from the liquid, once in the vapor phase, the multiplication of the electrons can occur in avalanches occurring in a micropattern structure, the Large Electron Multipliers (LEM) as shown in Figure 2.9.

The use of the LEM for the charge amplification is motivated by several facts [62]: a wide range of gains is achievable, from ~ 10 to $\sim 10^3$; the gain is easily adjustable to a large spectrum of physics requirements, the avalanches occur in confined spaces (holes in a printed circuit board) which provide a mechanical quenching of the UV photons (in pure argon it is not possible to introduce quenching molecules like in gas mixtures normally used in gas detectors). It is a detector capable of cryogenic operation and large surfaces can be covered as a collection of individual $\sim 1 \times 1$ m^2 elements.

The LEM consist of copper cladded epoxy plates with a thickness of a millimeter and with mechanically drilled holes. It can be produced by the industry with the same technology used for printed circuit boards. The holes have diameters of 500 μm and a pitch of 800 μm. There are ~ 200 holes per cm^2. The copper around the drilled hole is removed in a etched rim of 80 μm in order to avoid edge effects and sharp points which would favor discharges [63] (see Figure 2.10).

The gain $\mathcal{G}$ in the LEM can be described by $\mathcal{G} = e^{\alpha\, d}$ where d is the gap thickness and α is the Townsend coefficient (for a detailed description of Townsend avalanche see Chapter 3). In order to compute the amplification inside the holes, it is necessary to replace the

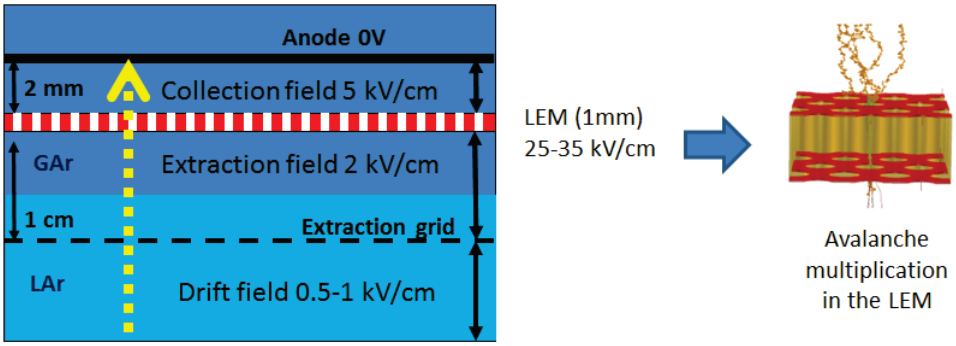

Figure 2.9: Schematic representation of the dual-phase charge readout technique based on the extraction of the electrons from the liquid phase, their amplification in avalanches occurring in the gas phase within the LEM detectors and the final charge collection on a segmented anode.

gap thickness d by the effective amplification path length within the holes, called x, which can be related to the length of the field plateau along the hole. The effective gain is then expressed as:

$$\mathcal{G}_{eff} = T \exp\left[A\rho x \, \mathrm{e}^{(-B\rho/(\kappa E_0)}\right] \tag{2.12}$$

where A and B are parameters depending on the gas, ρ is the gas density, $E_0 = V/d$ is the nominal electric field and d the LEM thickness, κE_0 the effective field, and T is the transparency (some electrons, in part due to the large diffusion in pure argon, may be collected on the grids or on the electrodes of the LEM). Electrostatic calculations of the LEM-hole geometry give a maximum field in the hole which is lower than the naive V/d, consistent with a value of $\kappa = 0.95$ [64].

2.4.2 Anode charge collection

The amplified charge is then collected by two independent charge readout *views* combined in a single plane providing x and y coordinates with a 3 mm readout pitch [65]. In Figure 2.11 it is shown the geometry of the strips which are defined by a complicated pattern of gold plated copper tracks on 0.1 mm width and 1.56 mm pitch. In order to solve the topological problem of having two crossing views electrically insulated on the same plane, some continuity connections among tracks belonging to the same view are performed on the other side of the printed circuit board by using vias. The pattern of the copper tracks defines overall strips of 3.125 mm pitch. This particular pattern has been chosen after several studies in order to ensure an even sharing of the collected charge among the two views without biases related to particular track angles with respect to the strips orientation. Once corrected for the angular dependence of the track path seen by each view the charge sharing per unit of length is perfectly symmetric [65]. The measured capacitance per unit of length of the strips amounts to 150 pF/m.

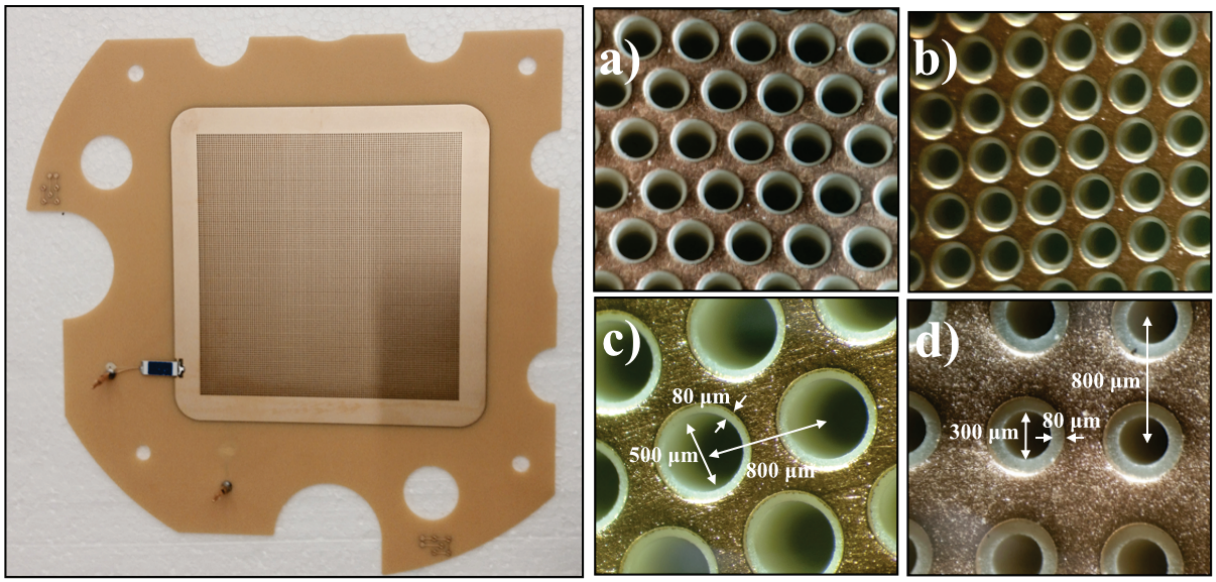

Figure 2.10: Picture of a prototype LEM (left). A microscope view of some LEM samples (right) with an the hexagonal hole arrangement (a) and a square arrangement (b). On the bottom zooms (c) and (d) on two samples with different hole sizes are shown [63].

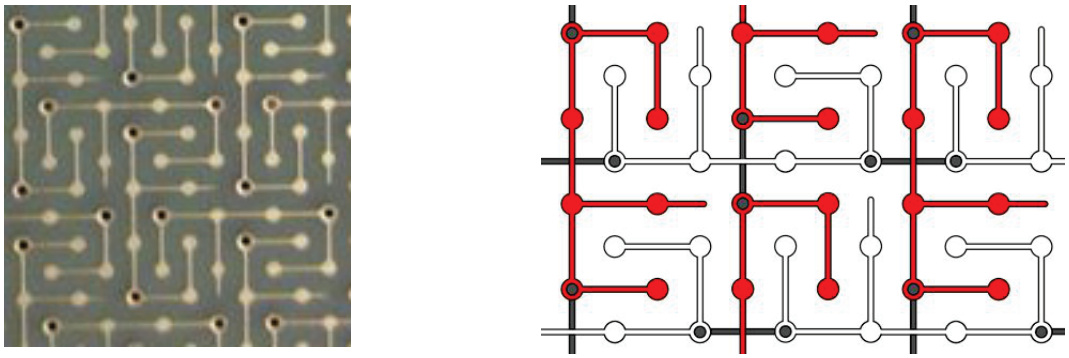

Figure 2.11: Picture of the anode showing the copper track pattern that allows a 2 views readout on the same circuit board (left) and schematic representation of the interconnection between both views (right): View 0 is filled in red and view 1 in white. The continuity connections performed on the other side of the printed circuit board are in solid black. [65].

2.5 Differences between single-phase TPC and dual-phase TPC

The dual-phase TPC provides several advantages with respect to a single-phase LAr TPC. They can be summarized in this way:

- the LEM allows a tunable gain typically in a range between 20 and 100. As shown above (see Equation (2.12) the gain $\mathcal{G}_{eff}$ is a function of the electric field. Varying the potential difference across the two faces of the LEM around 3 kV it is possible to tune the gain as function of the purity conditions or to provide an additional safety margin with respect to the noise;

- the charge amplification process passing from the liquid phase to the vapour and the consequent gain obtained in the LEM permits to reach a high signal-to-noise ratio typically greater than 100 and in a low detection threshold (smaller than 100 keV) at 3 sigmas above the noise RMS. In Figure 2.12 it is shown a comparison between the event display of ICARUS T600 (left) and a 3 liter dual-phase chamber (right). For a single-phase TPC the typical ratio S/N is ~ 5 for the inductions planes and ~ 10 for the conduction plane. For a dual-phase TPC the ratio is $S/N \sim 100$ in both cases;

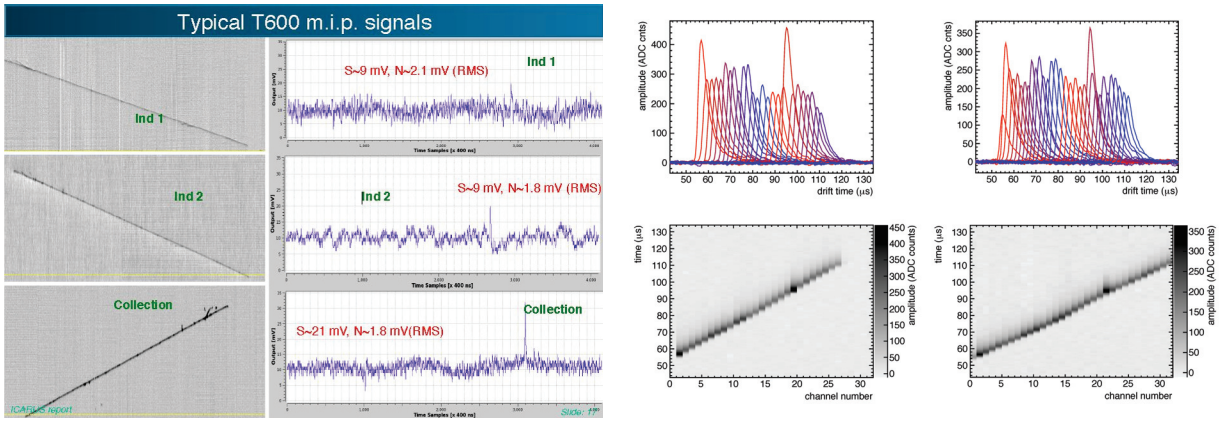

Figure 2.12: Event display for ICARUS (left): on the left is shown the reconstructed image for the induction planes (top and center) and for the conduction plane (bottom). Event display in a 3 liter dual-phase chamber (right): on the top is shown the raw waveform showing the amplitude of the signal on both views. On the bottom the drift time versus channel number of the reconstructed hits.

- the dual-phase TPC readout is based on two collection views: each plane collects the same quantity of charge, and so it is possible to have a good reconstructed image in each view. On the contrary, single-phase TPC has two induction planes and a collection plane: on the induction planes the S/N is worse than the one the collection

plane and the signals are bipolar, resulting in a signal cancellation in case of long signals along the drift coordinate as in the case of dense electromagnetic showers. In addition, the use of two collection views limits ambiguities in the bi-dimensional localisation compared to more complex schemes based on induction views like the one designed for DUNE single-phase version where one of the induction views consists of wires making a zig-zag pattern around the x and y wires by wrapping on the borders of the wire chamber.

- a high signal-to-noise ratio allows to have a fully active long drift projective geometry with no dead materials embedded. It makes then possible to reduce the number of readout channels needed to cover the active volume.

- the number of readout channels is still smaller than an equivalent single phase TPC even with a finer strip pitch: for a very large detector design as in DUNE a dual-phase TPC can use a 3 mm pitch, compared to the 5 mm size in the single-phase case still having a number of channels smaller by a factor two. This choice has a strong impact on the resolution of the detector;

- in a dual-phase TPC the electronic readout is placed at the top part of the detector: this allows even the cryogenic electronics to be accessible and easily replaceable without contaminating the pure liquid argon volume. The digital electronics can be completely at warm temperature and based on high bandwidth and cheap technologies without the requirements of a digital electronics immersed in the liquid argon as for a SP equivalent detector.

2.6 Future experiments

2.6.1 DUNE

The Deep Underground Neutrino Experiment (DUNE) will consist of two neutrino detectors: a near detector at the Fermi National Accelerator Laboratory in Batavia, Illinois, and a second detector, much larger, will be installed more than one kilometer underground at the Sanford Underground Research Laboratory in Lead, South Dakota, 1300 km downstream of the source. The neutrino beamline will be provided by the Long-Baseline Neutrino Facility at Fermilab (see Figure 2.13). As far detector, DUNE is developing two different options, a single-phase TPC and a dual-phase TPC (see Figure 2.14). The two options will exploit the same cryostat design with an inner volume of 14 m high, 14.1 m wide and 62 m long [66]. The crucial difference between the two choices is the orientation of the electric field (and consequently the drift direction and the readout plane position):

- in the case of the dual-phase TPC the drift length is 12 m: the anode is the top part of the detector and the cathode close to the cryostat floor (the electric field is along the vertical direction). The total number of channels in the readout system will be 153600, with a pitch size of 3 mm;

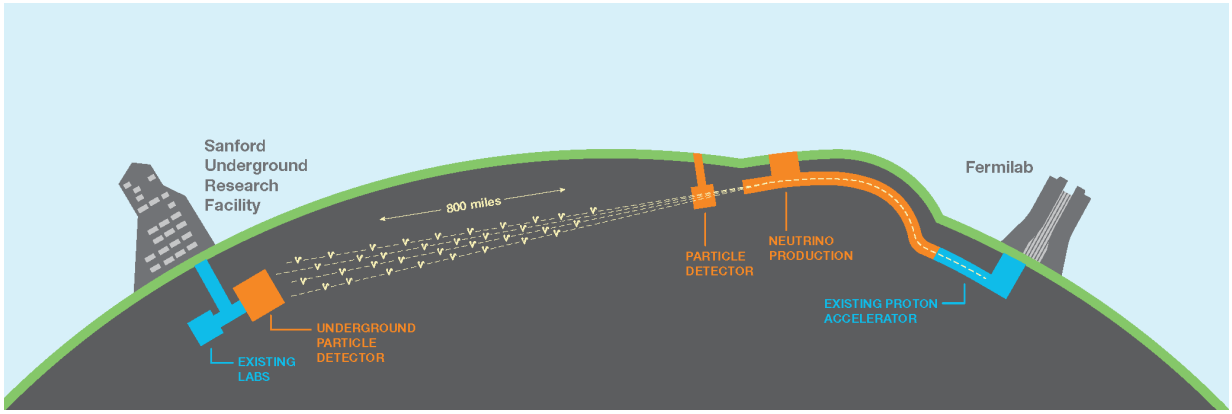

Figure 2.13: Schematic representation of DUNE experiment.

- in the case of the single-phase TPC the drift length is 3.6 m: the active volume is segmented in 4 drift regions constructed by placing alternating high-voltage cathode planes and anode readout planes inside the active volume (see Figure 2.14 top left). In this configuration the total number of channels is 384000, with a pitch size of 5 mm.

2.6.2 WA105/ProtoDUNE dual-phase

The WA105/ProtoDUNE [65] dual-phase experiment aims at demonstrating the operation of the novel large liquid argon dual-phase time projection chamber: it is a full scale demonstrator for DUNE 10 kt dual-phase. The active volume of this prototype is $6 \times 6 \times 6$ m^3 and the total number of readout channel is 7680.

The LEM and anode printed circuit boards employed for the dual-phase readout have dimensions of 50×50 cm^2. They are integrated in 4 Charge Readout Planes (CRP) of 3×3 m^2, covering side by side a total detection surface at the top of the detector of 6×6 m^2. The position of the 4 CRP units with respect to the liquid level can be individually adjusted in order to match the configuration shown in Figure 2.9, having the liquid level at the middle of the gap in between the submersed extraction grid and the bottom face of the LEM. For this purpose each CRP is suspended by 3 cables and equipped with capacitive level meters which allow measuring the LAr level with sub-millimetric accuracy. Figure 2.15 shows a schematic view of the 4 CRP units in WA105.

The CRP units have the same design as those foreseen to equip the 10 kt DUNE dual-phase modules which will have a drift of 12 m and an anode active area of 60×12 m^2 covered by 80 CRP units. WA105 will operate in typical condition corresponding to a LEM gain of 20 and a S/N ratio greater than 100.

A 3D model of the WA105 detector is shown in Figure 2.16. It is possible to see the cryostat iron exoskeleton (green), the insulation layers (yellow) terminating on the inner side with the *GTT Co.* corrugated stainless steel membrane (gray) and the field

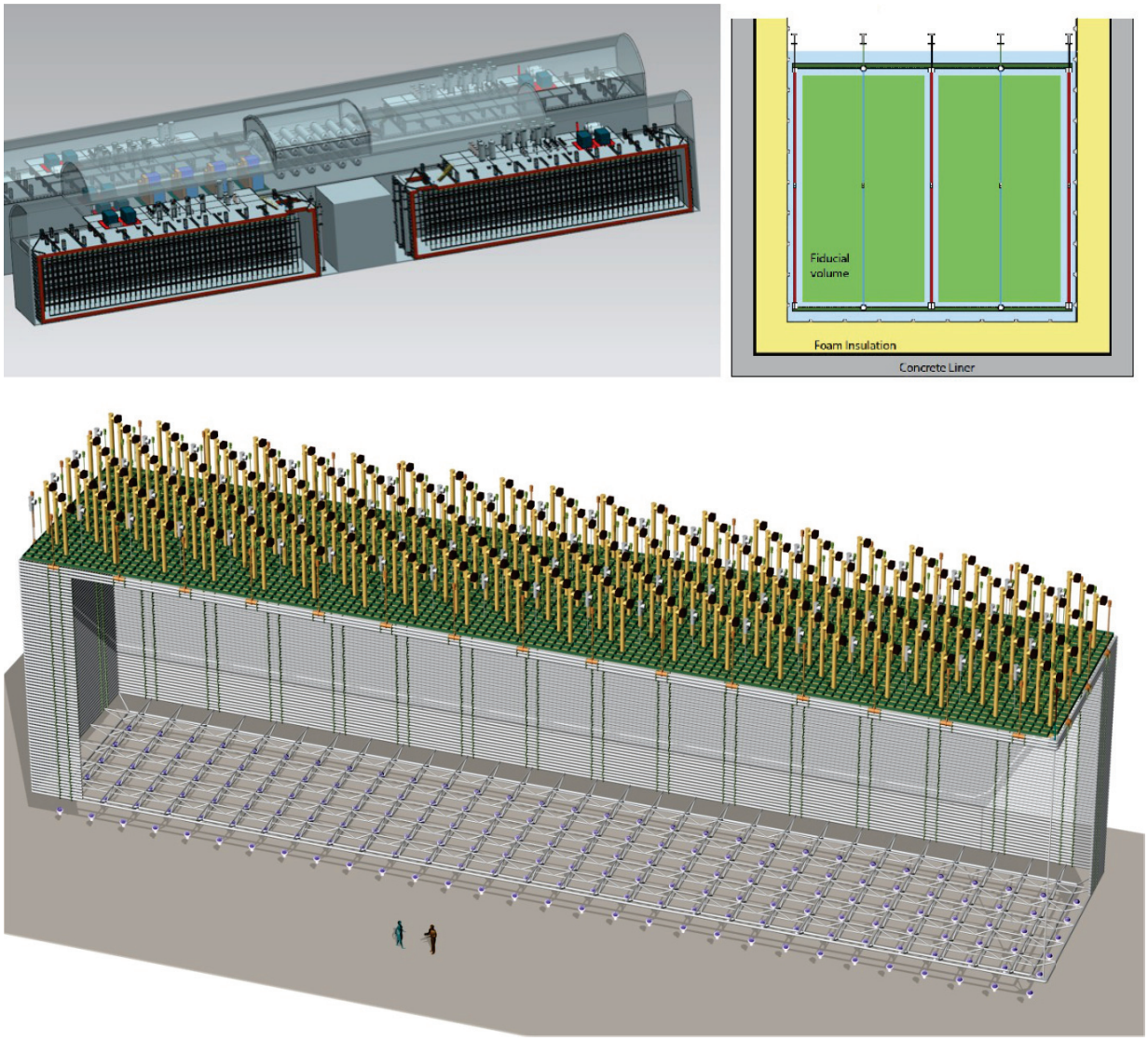

Figure 2.14: Top: 3D models of two DUNE 10 kt far detectors using the single-phase design (left) and schematic view of the detector elements (cathode and anode planes) of the single-phase TPC design inside the detector. Bottom: 3D model of a 10 kt DUNE far detector module based on the dual-phase design. Each 10 kton dual-phase module has an active LAr volume of $60 \times 12 \times 12$ m^3 delimited by the field cage.

cage containing the liquid argon active volume. The total LAr volume inside the tank is $7.9 \times 8.5 \times 8.5$ m^3. An array of cryogenic photomultipliers for the detection of the scintillation light is located below the transparent cathode located at the bottom of the field cage. The CRP planes are located at the top of the detector and they are not visible in the picture. The digital readout electronics is installed in μTCA crates on the roof of the detector. A beam pipe is used to bring charged particles coming from a dedicated test-beam line inside the field cage, crossing the insulation layers and the non-active liquid

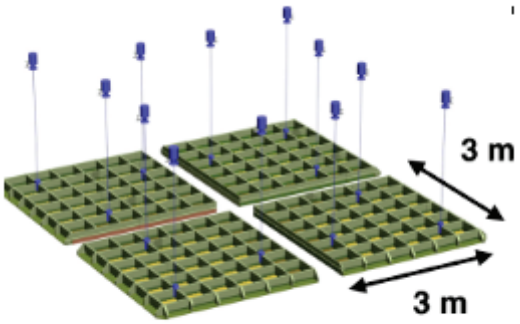

Figure 2.15: Exploded view of the anode plane of WA105 including 4 dual-phase CRP units, individually suspended by 3 cables and placed side by side with a dead space of 1 cm in order to cover a detection surface of 36 m^2.

argon volume around the field cage.

WA105 has several goals, both from the technical and the physics points of view.

The technical issues to be addressed include:

- test the cryostat design derived from the LNG tanks industry (GTT corrugated membrane and insulation design);
- obtain a very high liquid argon purity, ($<$ 100 ppm for O_2 for instance correspond for an electron lifetime of about 10 ms), the minimal target is to achieve 3 ms;
- instrument a large surface (36 m^2) dual-phase readout plane with the same units foreseen for the DUNE detector;
- build and test a large field cage and cathode structures;
- build and operate a very high voltage system ($300 - 600$ kV);
- test the accessible cold front-end charge readout electronics and the associated very high bandwidth warm digital electronics;
- test the long-term behaviour of the wavelength shifter coating of photomultipliers;
- test the integrated light readout electronics.

The main goal of WA105 from the physics point of view is to exploit the exposure of the detector to a dedicated test-beam line which will be providing charged hadrons and electrons beams in a range between 1 GeV/c and 12 GeV/c. WA105, which is actually in construction, will collect of the order of 100 millions on beam triggers during its operation in

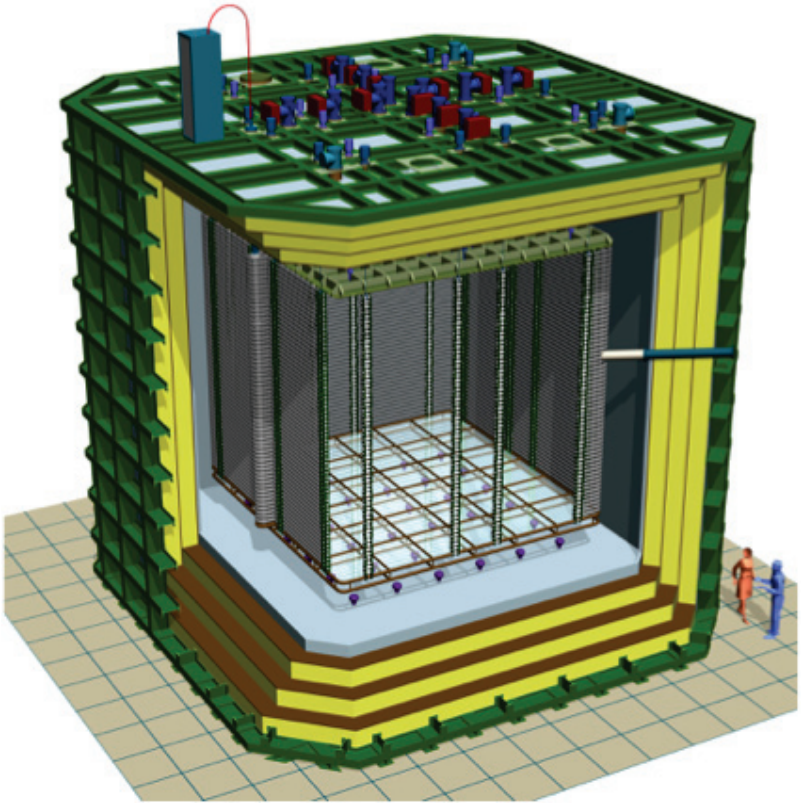

Figure 2.16: 3D model of the WA105/ProtoDUNE dual-phase demonstrator at CERN.

2018. This will allow calibrating the detector for what concerns the response to electrons and to the hadronic system of neutrino interactions (which is always the most difficult part to reconstruct in order to measure the energy of the impinging neutrino). Interactions of charged hadrons of known energy will allow cross-checking the reconstruction of the hadronic system as well as the PID performance. More generally WA105 will perform studies of hadronic calorimetry with unprecedented resolution and statistics of general interest for high energy physics. The analysis of its data sample will allow as well studying several systematics for the DUNE long-baseline experiment such as the study of hadronic cross-sections to be employed in nuclear re-scattering models; the energy scale calibration; the electron identification efficiency; the background from neutral pions decay to electron identification by using a sample of neutral pions produced in hadronic interactions. In general terms this large data sample will allow testing and improving all the neutrino event reconstruction algorithms.

The studies on the charge readout analysis developed in this thesis have been performed in preparation of the WA015 operation in order to develop algorithms which will be then tested on beam data sample such as the calibration of the energy losses measurements, particle identification and electron/photon separation.

Chapter 3

Verification of the Paschen law in ultrapure argon gas at cryogenic temperatures

The operation of the LEM in the Dual Phase liquid argon TPC requires a good knowledge of the maximal voltage that can be applied to the LEM before starting an electric arc. A systematic study of breakdown behaviour in pure gas argon at cryogenic temperatures is crucial for the understanding of the operational limits of micro pattern gas detectors used to get amplification in the charge readout.

In 1889, F. Paschen [67] states that breakdown tension of a gap is a non linear function of the product of the gas pressure and the gap size, usually written as $V = f(dp)$, where d is the gap distance and p is the pressure. Extensive additional experiments for different pressure ranges and gases and a variety of electrode shapes have expanded the data set involved. In the literature it is possible to find several works on the empirical verification of the Paschen law in gaseous argon: Ledernez [68] suggests a modification to the classical form of the law and proposes to add a separate parameter which depends on the distance between the electrodes.

In this Chapter is presented an experimental study aimed at verifying the Paschen law in pure gaseous argon at cryogenic temperatures. This study was performed by using the LAr TPC prototype setup at IPNL Lyon. A structure which contained two parallel plates at adjustable distance was installed in the top part of the cryostat, in a totally controlled environment. The analysis was performed on data collected during four days, at different temperature and pressure conditions. The four different data-sets were then used to provide a new formulation for the Paschen law, including a linear dependence on the distance between the plates. Following an idea proposed by Sili [69], a non linear dependency has been proved of the breakdown tension on density condition.

In this Chapter first a derivation of the Paschen law is discussed. Then the experimental apparatus in Lyon used to take the data is described. Subsequently the data analysis is presented: the validation of the model which includes a linear dependence on the distance between the plates is shown and then the choice of a non linear correction related to the

density of the gas is discussed. Finally a global fit of the four data-sets is presented.

3.1 The Paschen law derivation

The purpose of this Chapter is to analyse the generic breakdown behaviour between two parallel metallic plates at a distance d. The number $\mathrm{d}n$ of the electron per unit of length in the avalanche between the cathode and the anode can be expressed in the following way:

$$\mathrm{d}n = \alpha\, n\, \mathrm{d}x \tag{3.1}$$

where α is the probability to ionize a neutral gas by collision per unit of length. This probability is known as the *first Townsend ionization coefficient*:

$$\alpha = \frac{1}{\lambda_e}\, \mathrm{e}^{-\frac{E_i}{E_e}} \tag{3.2}$$

with λ_e the electron mean free path, E_i the ionisation energy of the gas and E_e the electron energy colliding with the gas neutral. If before the avalanche there are n_0 free electrons (produced by thermal emission), after the avalanche the number n of the electrons is:

$$n = n_0\, \mathrm{e}^{\alpha d} \tag{3.3}$$

The ions created in the avalanche bombard the cathode and create new ions-electrons pairs with a probability γ (called *second Townsend ionization coefficient*). The number n_0' of the electrons created by bombardment is:

$$n_0' = \gamma\,(n - n_0'') \tag{3.4}$$

where n_0'' is the total number of electrons emitted by the cathode, *i.e.* $n_0'' = n_0 + n_0'$. Using the Equation (3.3) it is possible to compute the total number of electrons reaching the anode:

$$\begin{aligned} n &= n_0''\, \mathrm{e}^{\alpha d} \\ &= (n_0 + n_0')\, \mathrm{e}^{\alpha d} \\ &= \left(n_0 + \frac{\gamma(n - n_0)}{1+\gamma}\right) \mathrm{e}^{\alpha d} \end{aligned} \tag{3.5}$$

Using the Equation (3.5) is now possible to write:

$$n = \frac{n_0\, \mathrm{e}^{\alpha d}}{1 - \gamma(\mathrm{e}^{\alpha d} - 1)} \tag{3.6}$$

The spark happens when $1 - \gamma(\mathrm{e}^{\alpha d} - 1) \to 0$. Since normally $\mathrm{e}^{\alpha d} \gg 1$, the Equation (3.6) can be rewritten in the following way:

$$n = \frac{n_0\, \mathrm{e}^{\alpha d}}{1 - \gamma\, \mathrm{e}^{\alpha d}} \tag{3.7}$$

Thus the breakdown condition becomes:

$$e^{\alpha d} \sim \frac{1}{\gamma} \tag{3.8}$$

It implies

$$\alpha = \frac{1}{d} \ln\left(\frac{1}{\gamma}\right) \tag{3.9}$$

Since the mean free path $\lambda_e = k_B T/(\sigma_{ei} p)$ (where k_B is the Boltzmann constant, σ_{ei} is the electron impact ionization cross section, T and p respectively gas temperature and pressure) and $E_e = e\lambda_e \mathcal{E}$, it is possible to combine Equation (3.2) with Equation (3.9), obtaining:

$$\frac{1}{d} \ln\left(\frac{1}{\gamma}\right) = Ap \; e^{-\frac{Bdp}{V_b}} \tag{3.10}$$

with the assumption that the electric field is uniform before the gas breakdown ($E = V_b/d$). It is now possible to write a relation between the breakdown tension V_b and the product dp:

$$V_b = \frac{B\,dp}{C + \ln(dp)} \tag{3.11}$$

with:

$$A = \frac{\sigma_{ei} p}{k_B T} \qquad B = \frac{E_i \sigma_{ei}}{e k_B T} \qquad C = \ln\left(\frac{A}{1/\gamma}\right) \tag{3.12}$$

3.2 Experimental apparatus

The measurements for the Paschen law were performed in the cryostat available in Lyon (shown in Figure 3.1) in a controlled environment from the point of view of pressure temperature and purity. This cryostat consists in an hermetic vessel in electro-polished steel of 250 L filled with pure liquid argon; this inner vessel is contained in a larger thermal vessel bath containing non-purified boiling liquid argon at atmospheric pressure. The thermal bath contains also the pure argon recirculation circuit including a pump actioned by gaseous nitrogen and the purification cartridge. The thermal bath vessel is vacuum insulated with respect to the external environment in order to minimize the heat input. The pure liquid argon is kept at constant temperature by the evaporation of the non-purified liquid argon in the external bath, which is automatically refilled, and by the pure gas re-condensation operated by a helium cryo-cooler. The pure argon gas pressure is adjusted by the operation of the cryo-cooler and by the height of the thermal bath liquid argon level. A cryogenic photomultiplier Hamamatsu R5912-02-mod coated with TPB placed at the bottom of pure liquid argon vessel below the cathode of the TPC allowed for the detection of the UV scintillation light and the monitoring of the liquid argon purity conditions.

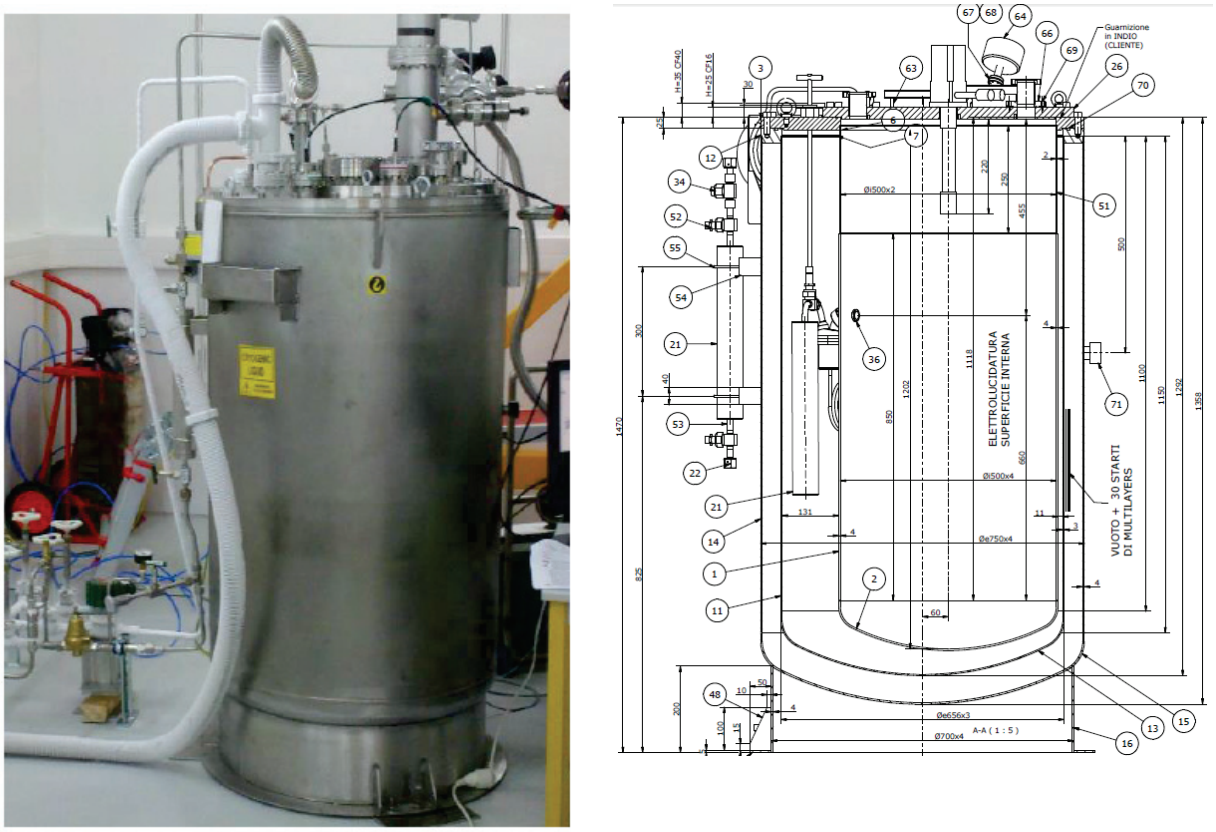

Figure 3.1: Cryostat installed in Lyon (left) and its project design (right).

As preliminary operation the pure argon vessel inside the cryostat was evacuated at the pressure of 10^{-6} mbar; then it was filled with liquid argon. The argon purity, at 0.1 ppb oxygen equivalent impurities level, was guaranteed by purification performed during the filling with an external purification cartridge and by the purification continuously operated by the recirculation system.

The purification of the argon has been monitored by scintillation light measurements since the slow component of the scintillation light is sensitive to the level of electronegative impurities: no considerable variations of the slow component have been noted with time during the Paschen measurements. Figure 3.2 shows a waveform recorded by the photomultiplier during the measurements. An exponential fit of the second part of the slope allows to compute the slow time constant (in this example $\tau_s = 1.56$ μs).

Figure 3.3 represents the structure containing the parallel plates used to measure the breakdown voltage. The plates are made of electro-polished stainless steal and are inserted in a plastic structure. The plates have smoothed corners in order to guarantee the maximal electric field is achieved in the inner flat region and not affected by sharp edges.

The movement of the plates is provided by an external precision rotating feed-through: the mechanical setup transforms a rotatory movement in a linear translation allowing to

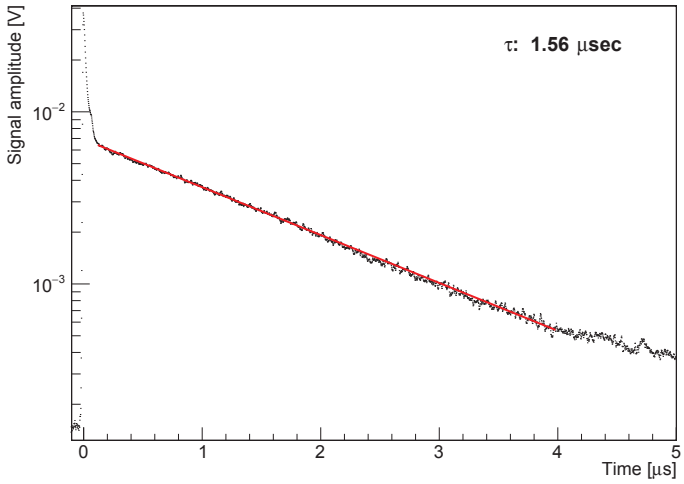

Figure 3.2: Example of waveform recorded during the Paschen measurements.

change the gap between the plates by rotating the feed-through. During the installation of the structure, a calibration was performed in order to verify the relation between the rotation angle and the plates distance. The contact point between the plates is defined as the point which makes a short circuit measured with an ohmmeter: this was set as $\vartheta = 0$ point. Starting from $\vartheta = 0$ the angle was increased progressively to the maximum gap by measuring the distance between the plates. After this measurement, in order to check that there were no hysteresis effects in the rotation, the distance between the plates was put to the maximum, the angle ϑ was decreased progressively to 0 and the measurement of the gap was taken.

In order to have enough precision in the gap measurement, the region $0 - 50$ mm was sampled, assuming a linear relation between the angle ϑ and the distance d between the plates:

$$d = a\,\vartheta + b \tag{3.13}$$

The uncertainty on the angle measurement is given by the angular scale accuracy of the rotary feed-through (1 division, *i.e.* 5°). The uncertainty on the gap value is given by the accuracy of the calliper (0.05 mm) employed for this measurement. This is a conservative choice, given the fact that the calliper used for these measurements is an electronic model, providing measurement down to 0.01 mm.

In Figure 3.4 are reported the results of the calibration measurements: on the left, data and interpolation for the measurements made increasing the distance between the plates and on the right the results of the measurements performed decreasing the gap. As expected the two measurements (increasing and decreasing the gap between the plates) are very similar. Some discrepancies appear between the data and the fit for big values of ϑ: they are not going to affect the rest of the analysis because these large gap values are not

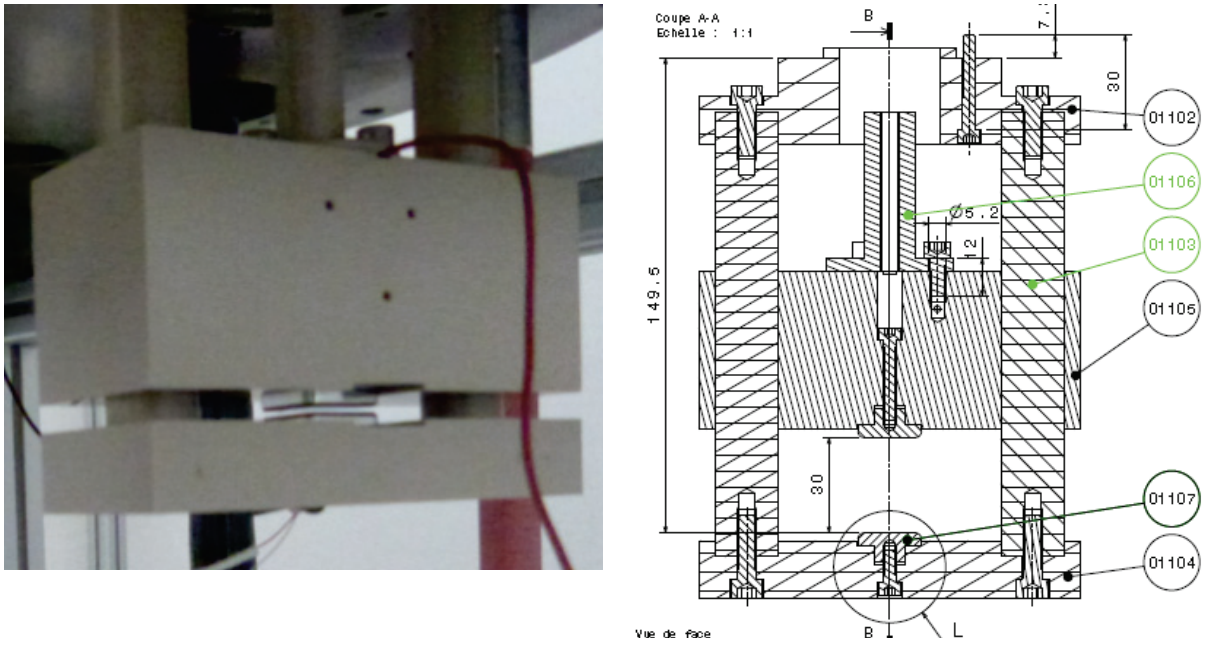

Figure 3.3: Plastic structure that contains the plates (left) and the project design (right).

used for the Paschen measurements.

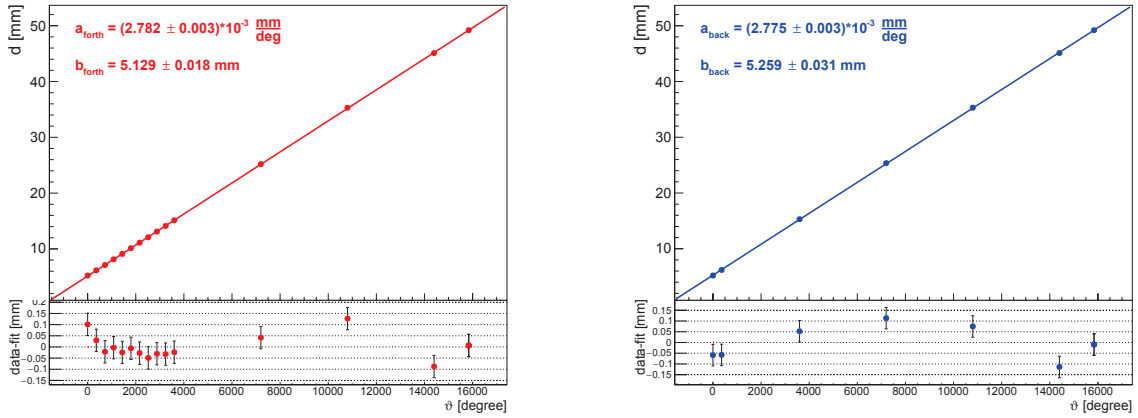

Figure 3.4: Linear fit by increasing the angle from 0 to 50 mm (left) and by decreasing the angle from 50 mm to 0 (right).

The values used for this analysis are the results of the fit performed by decreasing the distance between the plates (see Table 3.1). This choice is due to the procedure used during the data taking: after checking $\vartheta = 0$ by short circuit, the distance between the plates was brought to the maximum and reduced to 0.

a	$2.775 \cdot 10^{-3}$ mm/deg
b	5.259 mm

Table 3.1: Parameters to convert angle measurement in distance using Equation (3.13).

During the data taking which lasted four days, the gas pressure and temperature conditions were continuously monitored by using an DPG4000 pressure gauge and PT1000 sensors. The measurements were recorded using a LabView slow control system as shown in Figure 3.5. The achieved accuracy was of 0.01 mbar for the pressure and 0.1 K for the temperature.

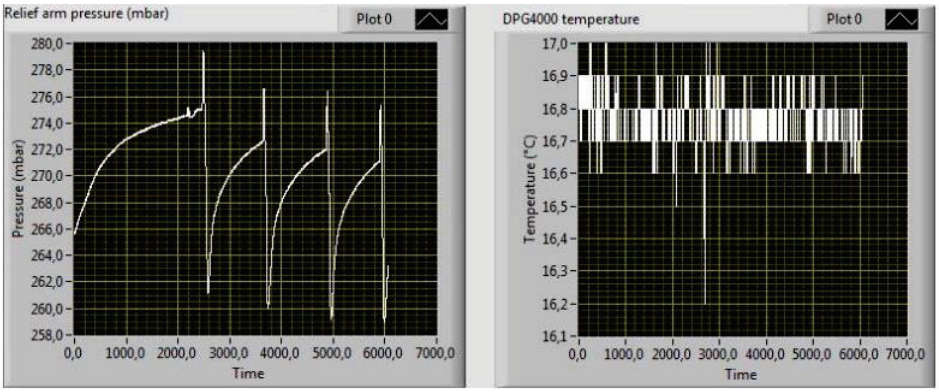

Figure 3.5: Example of LabView output for pressure (left) and temperature (right) measurement during the data taking.

The voltage difference applied to the parallel plates was generated with a CAEN N470 high voltage power supply operating with negative polarity. Tension was increased very slowly in steps of 5 V per second in the initial range starting from 0 V and in steps of 1 V per second in the last 100 V before reaching the breakdown voltage. The breakdown was detected simultaneously by three events: the trip on the HV power supply, which was set at the lowest trip sensitivity; the spark noise which was clearly audible outside the cryostat and by an electrical signal detected by a pickup system placed inside the cryostat and connected to a digital oscilloscope operating in single trigger mode. The breakdown voltage recorded in the measurement corresponds to the last value reached by the HV power supply before the trip and it has 1 V uncertainty.

3.3 Paschen measurements analysis

Looking at the typical behaviour of the breakdown voltage V_b as a function of the product dp (Figure 3.6), the region explored during the measurements in Lyon corresponds to the

rising right branch after Paschen minimum.

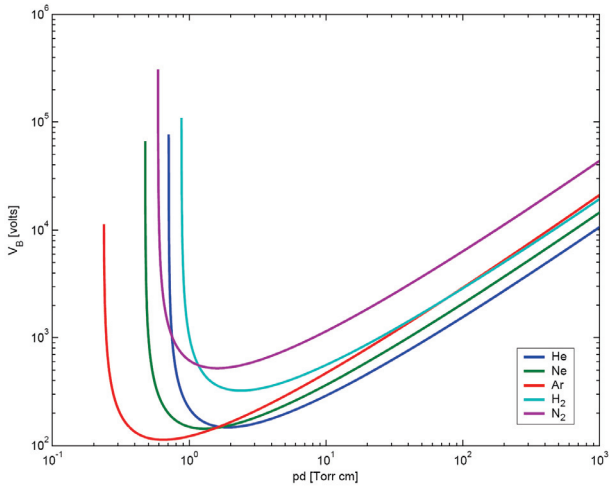

Figure 3.6: Typical Paschen curves at room temperature for different gases.

Looking at the raw data values in Figure 3.7 plotted before any analysis treatment it is possible to notice that the points follow a regular path with very small fluctuations. This regularity as a function of the distance among the plates shows that the measurements were not driven by occasional short circuits.

For each measurement temperature and pressure of the gas were monitored. The temperature was measured by a probe placed nearby the parallel plates of the Paschen setup. In Figure 3.8 are shown the temperature values for each measurement during the four days. Even if the mean value of temperature was quite different from one day to the other, the fluctuations within each day were negligible. These temperature variations from one day to the other were induced by changing the liquid argon level inside the cryostat and consequently the temperature gradient inside the gas. In Figure 3.9 are instead shown the pressure values which were fluctuating due to the periodical refilling of the external cooling bath of the cryostat.

In the case of the measurements performed for this work the temperature variations were more important than pressure variations (maximal temperature variation $\approx$ 40%, maximal pressure variation $\approx 0.6\%$, as it can be seen in Figures 3.8 and 3.9.

In a first approximation in this analysis argon is considered as an ideal gas. To verify the validity of this assumption it is necessary to compare this modelization to the one for a real gas. For an ideal gas the relation between the pressure p, the volume V and the temperature T is given by the equation $pV = nRT$, where n is the amount of substance of the gas and R is the gas constant. The relation between the temperature and $\overline{\rho} = n/V$ is:

$$T = \frac{p}{R\overline{\rho}} \tag{3.14}$$

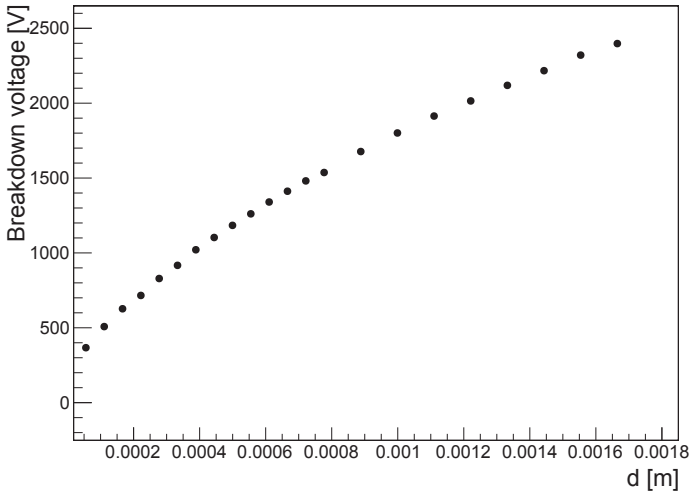

Figure 3.7: Breakdown tension V_b as a function of the distance d between the plates.

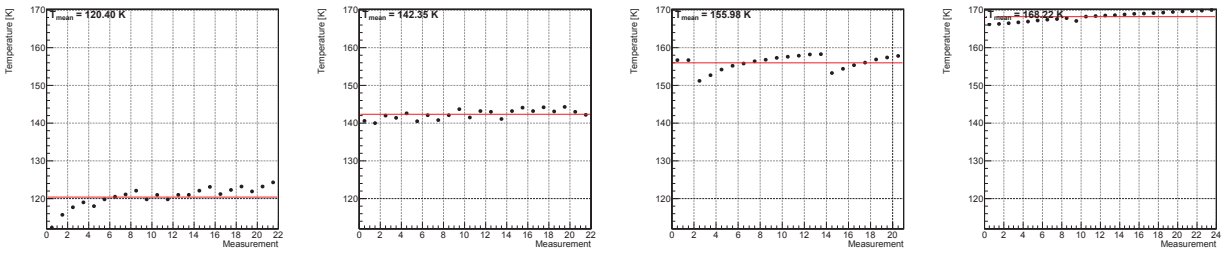

Figure 3.8: Temperature values during the four days of the Paschen measurements: first day (left), second day (center left), third day (center right) and fourth day (right).

On the other hand, the behaviour of a real gas can be described by the van der Waals equation:

$$\left(p + a\frac{n^2}{V^2}\right)(V - nb) = nRT \tag{3.15}$$

where a and b parameters depend on the gas (for argon $a = 1.355$ bar $\mathrm{L}^2\,\mathrm{mol}^{-2}$ and $b = 0.0320$ $\mathrm{L\,mol}^{-1}$ [70]). It results that:

$$T = \frac{p}{R\overline{\rho}}\left(1 - b\overline{\rho} + \frac{a}{p}\overline{\rho}^2 - \frac{ab}{p}\overline{\rho}^3\right) \tag{3.16}$$

As shown in Figure 3.10 left, the two models are very similar, with some discrepancies for high values of $\overline{\rho}$. The pressure value used to compute Equations (3.14) and (3.16) is $p = 1.26$ atm, the mean pressure of the first day of measurements: this choice does not affect the argument, since $\Delta p/p = \Delta T/T$ for both model.

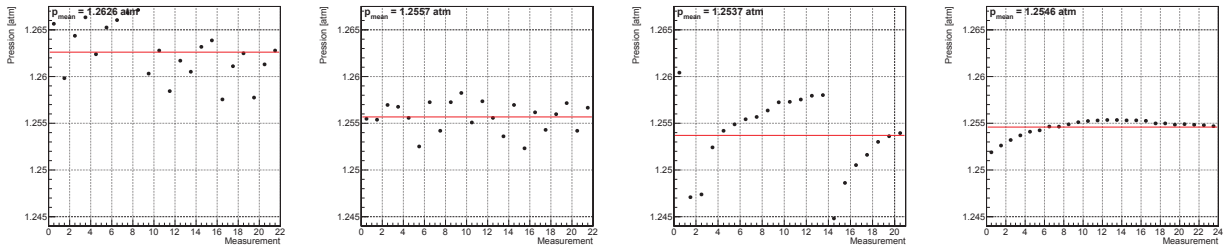

Figure 3.9: Pressure measurements during the four days of the Paschen measurements: first day (left), second day (center left), third day (center right) and fourth day (right).

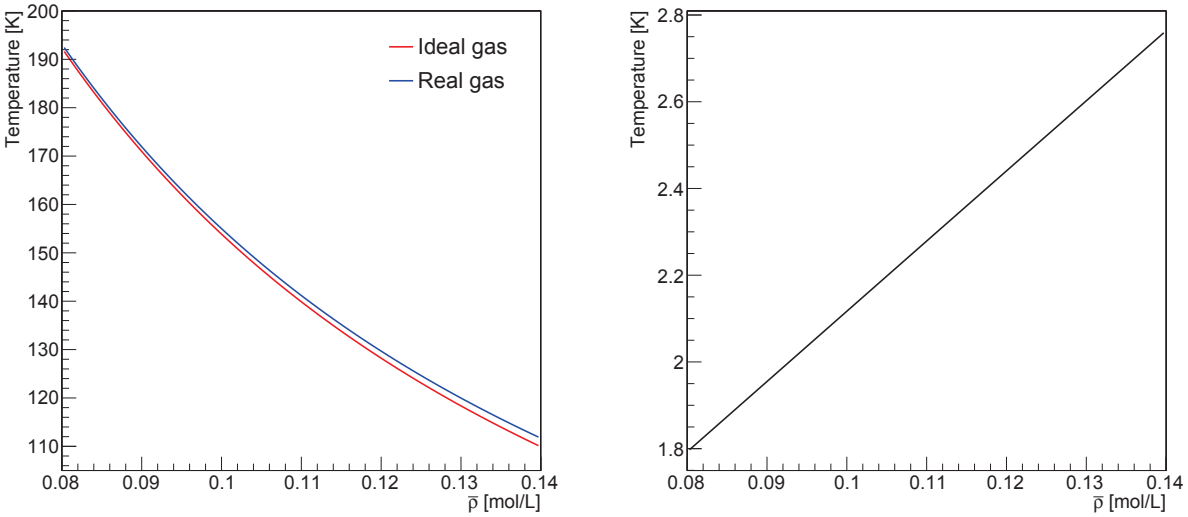

Figure 3.10: Temperature behaviour as a function of $\overline{\rho} = n/V$ for an ideal gas (red line) and a real gas (blue line) (left) and difference between the two parametrizations (right).

The gas temperature during the measurements varies from $\approx$ 120 K to $\approx$ 170 K (see Figure 3.8), it means that $\overline{\rho}$ varies between ≈ 0.13 mol/dm^3 and ≈ 0.09 mol/dm^3. In this interval of $\overline{\rho}$ the difference between the real gas model and ideal gas model is between 2 and 2.5 K (Figure 3.10 right). Approximating the gas as an ideal gas implies an error $\approx 2\%$, smaller than the temperature variation during the measurements.

Hence, under the assumption of ideal gas, one can write the gas density ρ as function

of temperature T and pressure p as:

$$\begin{aligned} \rho &= \frac{m}{V} \\ &= \frac{n\,M}{V} \\ &= \frac{M\,p}{R\,T} \end{aligned} \tag{3.17}$$

where m and n are respectively the mass and the number of the moles of the gas, V the volume occupied by the gas, M its molar mass and R is the ideal gas constant.

Temperature and pressure variations throughout the four days correspond to density variations. Gas density variations imply a different breakdown voltage points for the same distance among the plates. In Figure 3.11 are shown the breakdown tension values as a function of the product of distance and pressure dp for the four different days: it is obvious that a higher temperature (*i.e.* lower density) corresponds to lower breakdown tension. For this reason in this study a density correction will be discussed.

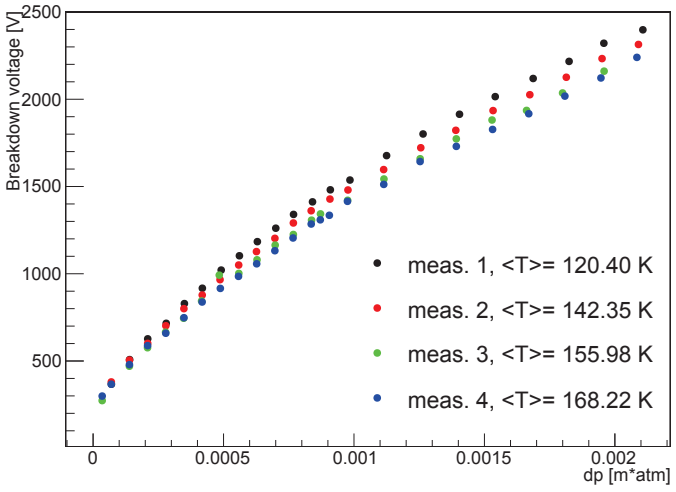

Figure 3.11: Breakdown tension as a function of dp for the four days. An higher value of temperature implies a lower breakdown tension.

Before applying a density correction factor a study of the best parametrization to describe the breakdown tension as a function of dp has been undertaken. First of all a fit using the standard formula (see Equation (3.11)) reported in literature has been performed. The results of this fit are reported in Figure 3.12. It is evident that a simple parametrization $V = f(dp)$ cannot provide a good description of breakdown behaviour in the data set.

A way to improve this model, as proposed by [68], is to modify Equation (3.11) introducing a linear dependence on the distance between the plates. The new function used to

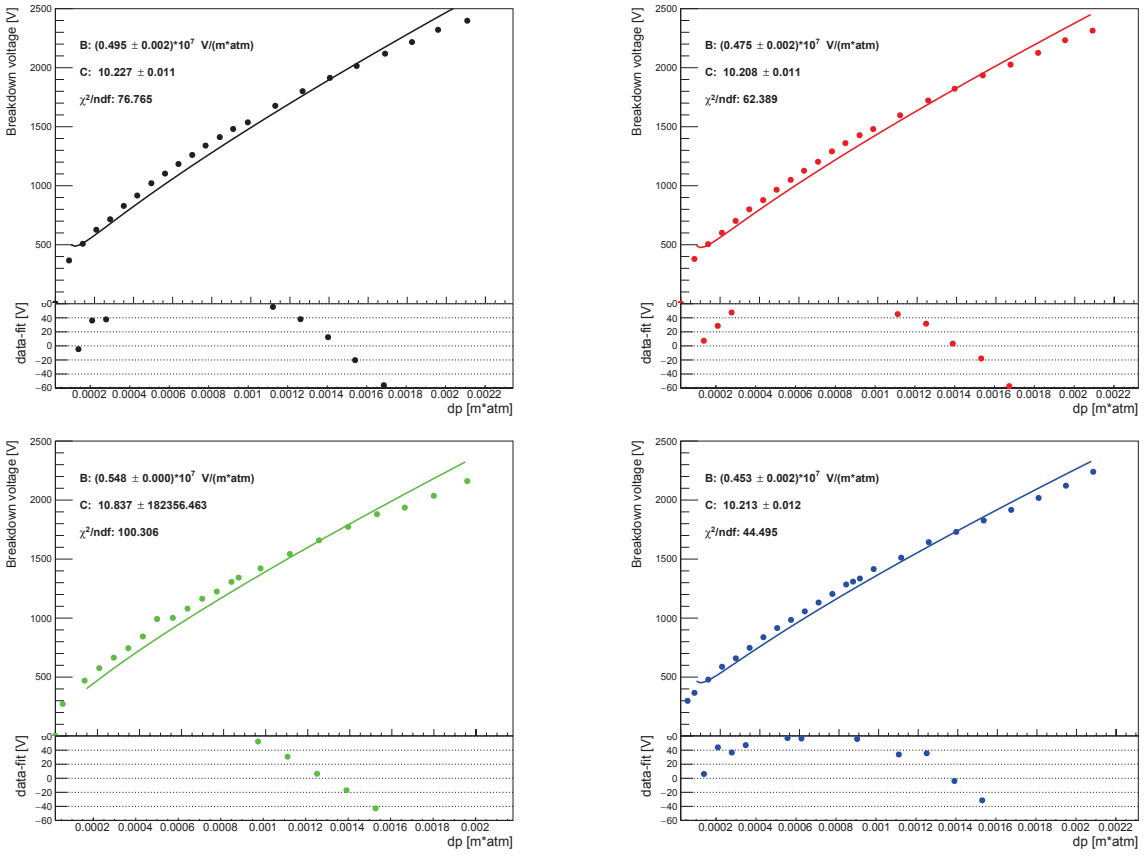

Figure 3.12: Fit of the breakdown tension as a function of dp using the classical expression of the Paschen law (see Equation (3.11)). Top: first day (left) and second day (right). Bottom: third day (left) and fourth day (right).

fit the data corresponding to this model is then:

$$f(dp,\ d) = \frac{B\,dp}{C + \ln(dp)} + \alpha d \tag{3.18}$$

In Figure 3.13 are shown the fits realized using the new parametrization and in Table 3.2 are listed the results of the fits.

Once a suitable parametrization has been established, the goal is to find a unified interpretation of the data sets as a function of the gas density. In order to compensate for the temperature and pressure effects described before (see Figure 3.6), a correction factor δ representative of the gas density has been defined:

$$\delta = \frac{p_0}{p}\frac{T}{T_0} \tag{3.19}$$

where the reference values T_0 and p_0 have been chosen corresponding to the mean values

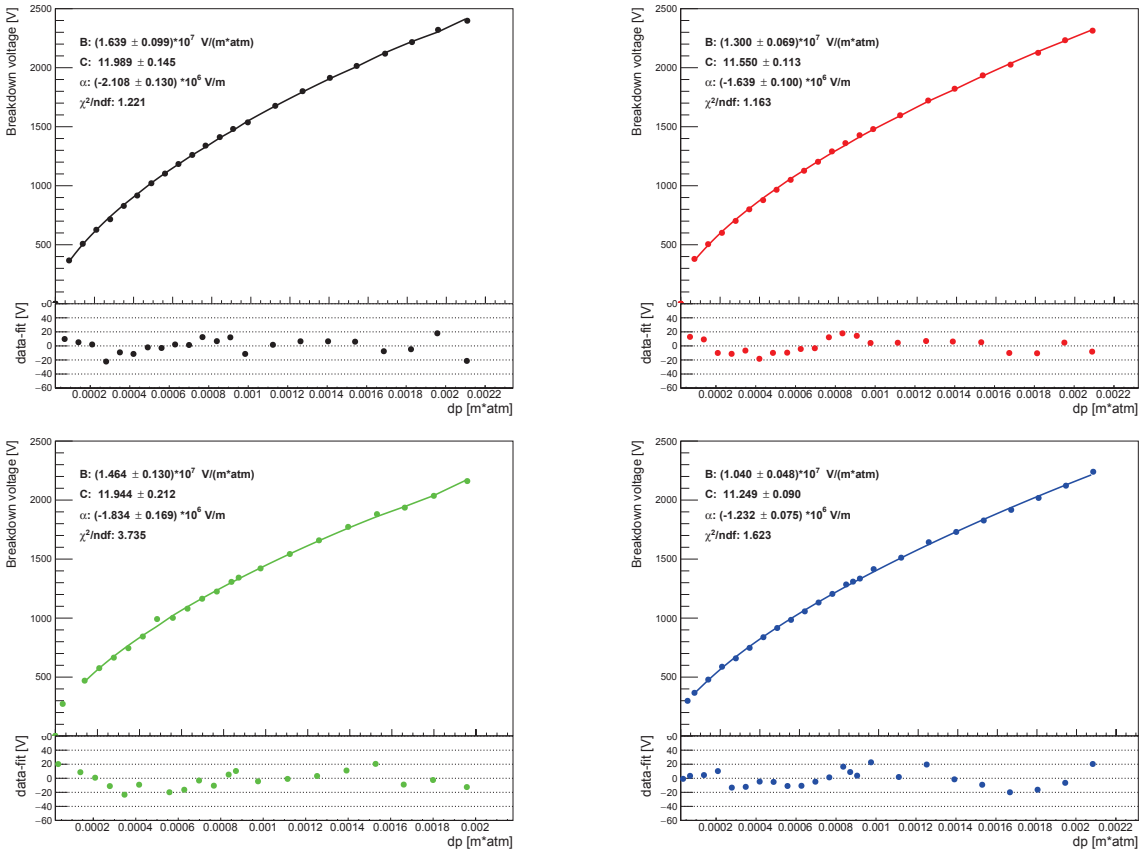

Figure 3.13: Fit of the breakdown tension as a function of dp using the modified expression of the Paschen law including a linear dependence term on the distance (see Equation (3.18)). Top: first day (left) and second day (right). Bottom: third day (left) and fourth day (right).

for the first set of measurements:

$$T_0 = 120.4 \text{ K} \qquad p_0 = 1.26 \text{ atm} \tag{3.20}$$

In the analysis it has been checked the effect of the δ correction in two different ways: by applying it either to the dp value or to the breakdown tension V. In the literature other works have studied both correction methods and shown that the corrections applied to V generally work better. For instance, a new empirical expression of the breakdown voltage for combined variations of temperature and pressure is given by [69].

If the correction is applied to the dp values, the corresponding transformation is $dp \rightarrow dp/\delta$. The effects of this correction are shown in Figure 3.14 left: there is no reduction of spread between points at different temperatures. This correction produces a shift in the right direction, but it is overestimating the physical effects.

If the correction is instead applied to the breakdown tension: ($V_b \rightarrow V_b \cdot \delta$, Figure 3.14 right). In this case the data sets at higher temperature assume higher breakdown tension

	Day 1	Day 2	Day 3	Day 4
B ($\times 10^7$ V/m atm)	1.639	1.300	1.464	1.040
C	11.989	11.550	11.944	11.249
α ($\times 10^6$ V/m)	-2.108	-1.639	-1.834	-1.232

Table 3.2: Fit parameters for the four different data sets. The parameters are referred to the function described in Equation (3.18).

values. In addition it results in a larger dispersion of the curves. This correction produces a shift in the top direction as expected, but, as previously, it overestimates the physical effects.

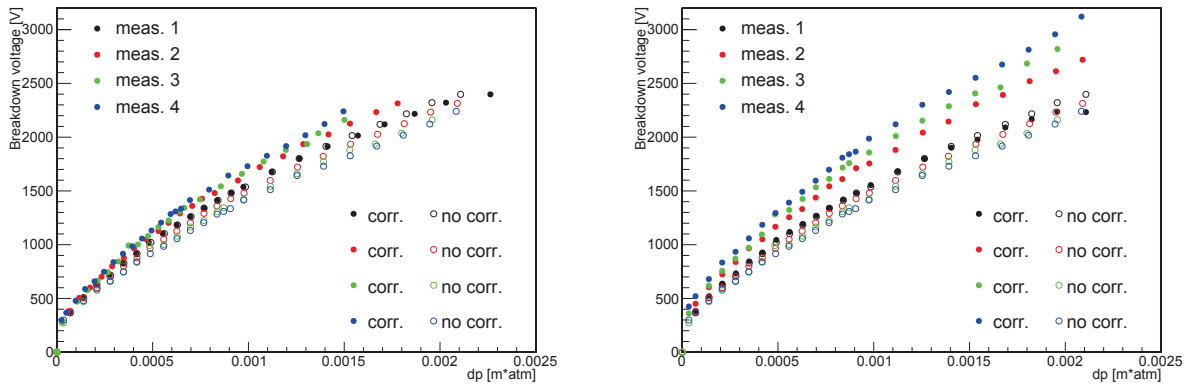

Figure 3.14: Comparison of Paschen curves before (empty dots) and after (full dots) the linear correction δapplied to dp values (left) and to the breakdown tension V_b (right). It is evident that a linear correction overestimates the physical effects in both cases.

As proposed by [69], it is interesting to evaluate the effect of a non linear correction factor following the law:

$$V_b = a\left(\frac{p}{T}\right)^b \tag{3.21}$$

where a and b are parameters to be determined.

In Equation (3.21) only the ratio between pressure and temperature has been taken into account in order to explicit the dependence on the gas density. To find the parameters of Equation (3.21), the relation between the breakdown tension and the ratio p/T for the same gap distance has been studied. In Figure 3.15 left are reported the breakdown tension values as a function of the ratio p/T. Each color corresponds to a different gap measurement.

To estimate the exponent b in the Equation (3.21) the distribution of the b value from the fit in Figure 3.15 left has been plotted and interpolated with a constant function. The result of this fit is shown in Figure 3.15 right.

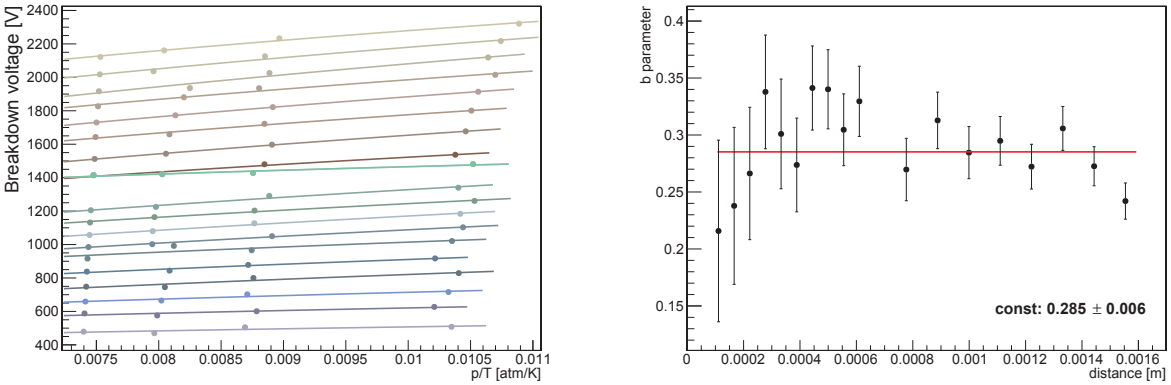

Figure 3.15: Breaking tension V_b as a function of the ratio p/T (left): each color corresponds to a different gap measurement. The data are fitted with a power law function. Distribution of the b values for different gaps with fit errors (right). The result of the fit is the value used in the analysis.

The non linear density correction can be then expressed in the following way:

$$\delta' = \left[\left(\frac{p_0}{p}\right)\left(\frac{T}{T_0}\right)\right]^{0.285} \tag{3.22}$$

As in the linear case hypothesis, the correction factor has been applied either to the abscissa values or to the breakdown tensions. In Figure 3.16 are shown the results of this new correction (full dots) with respect to the data without correction (empty dots). On the left it is shown the result of transformation $dp \to dp/\delta'$. The data shift goes in the right direction and the spread is reduced with respect to the linear correction, but differences persist for high values of dp. The origin of this problem could depend on the fact that there is a double counting of pressure effects: p is accounted in dp and δ'.

Figure 3.16 right shows the result of correction applied to the breakdown tension $V \to V \cdot \delta'$: in this case the spread is very much mitigated and the curves at different temperatures are very close.

After having obtained a good correction method for pressure and temperature variations, it is now possible to perform a single fit of all the experimental points taken during the four days of measurements. In Figure 3.17 are shown all the points after the correction $V \to V \cdot \delta'$ fitted with the function parametrized in Equation (3.18). Table 3.3 shows the fit results.

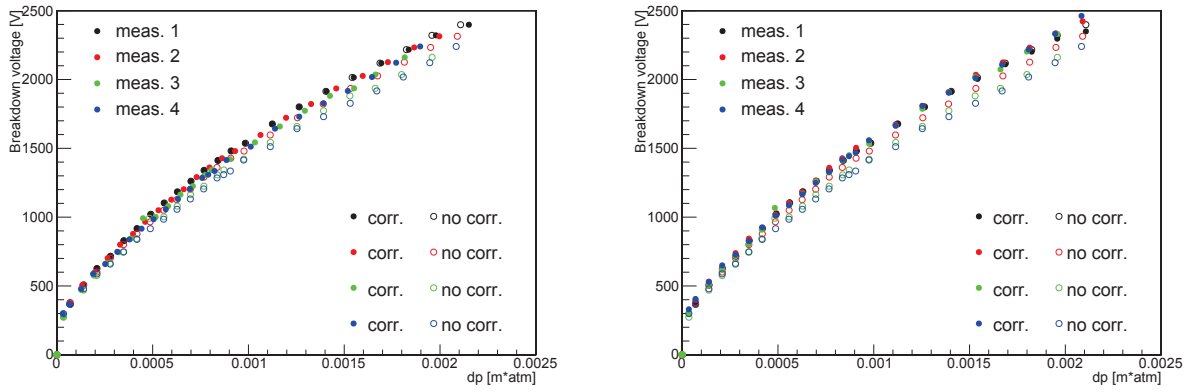

Figure 3.16: Comparison of Paschen curves before (empty dots) and after (full dots) the power law correction δ' applied to dp values (left) and to the breakdown tension V_b (right).

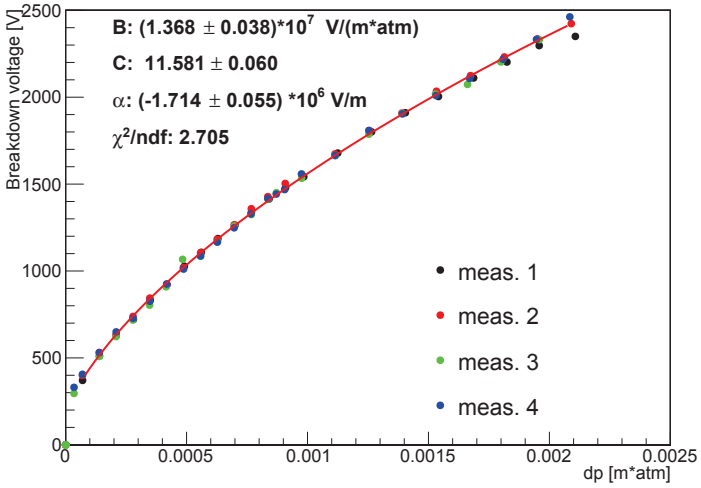

Figure 3.17: Final fit over the four data sets after the correction $V \to V \cdot \delta'$.

B ($\times 10^7$ V/m atm)	1.368
C	11.581
α ($\times 10^6$ V/m)	-1.714

Table 3.3: Fit parameters for the four different data sets after density correction. The parameters are referred to the function described in Equation (3.18).

3.4 Application of the results

The parametrization obtained in Section 3.3 refers to specific gas conditions, *i.e.* to the temperature $T_0 = 120.4$ K and to the pressure $p_0 = 1.26$ atm, since the breakdown tension values have been normalized by the factor δ'.

Furthermore, an additional complication has to be taken into account, since the parametrization contains a linear term which depends on the real distance d which was measured for the data set used to extract the parametrization. This information cannot not be directly extracted from the x axis of the plot in Figure 3.17 which refers to the product $d \times p$ and it has been computed for data sets normalized to 1.26 atm. In the plot a value of $dp = 0.001$ m atm read on the x axis, by assuming $p = 1.26$ atm corresponds to a gap of 0.001/1.26 m. For these values, through Equation (3.18) and with the parameters from Table 3.3, one obtains a breakdown voltage of 1564.4 V (corresponding to the following conditions: a gap of 0.79 mm, 120.4 K and 1.26 atm).

If for instance one wants to extract from the parametrization the information corresponding to a gap of 1 mm at 1 atm and 88 K, some addition corrections to the value extracted from the plot will be needed. For the wanted gap of 1 mm, still at 120.4 K and 1.26 atm the breakdown tension increases to 1800.6 V. At this point one will have to correct for the different temperature and pressure conditions (1 atm and 88 K), this correction is obtained by dividing the breakdown tension given by the parametrization by δ'. For these numerical values $\delta' = 0.977$ and therefore:

$$V_b(88 \text{ K},\ 1 \text{ atm}) = \frac{V_b(T_0, p_0)}{\delta'} = 1843.4 \text{ V} \tag{3.23}$$

This value of 1843 V is the breakdown voltage predicted by the parametrization for a parallel gap of 1 mm with gas conditions corresponding to 1 atm and 88 K. The LEM can be operated under the same gas temperature and pressure conditions up to an applied voltage of 3.5 kV before seeing breakdown discharges. This breakdown value is higher than the parallel plates configuration with an equivalent gap of 1 mm.

In the case of the LEM the situation is quite different. The study presented in this Chapter has been performed, consistently with the definition of the Paschen law, by using an uniform electric field between the plates. In the LEM the electric field inside the holes is always weaker than the equivalent electric field E_0 computed from the voltage difference applied to the two faces and from the LEM thickness. Furthermore it is not uniform and it reaches its maximal value only at the center of the holes. A calculation of the field along the LEM hole axis shown in Figure 3.18 indicates that the field is larger at the center of the hole [63].

Since Paschen law provides a local modeling for uniform electric fields, the way to apply this elementary model from experimental data is to integrate the parametrization obtained along the local field conditions, for instance by using GARFIELD, inside the LEM holes in order to compute a discharge model of the LEM.

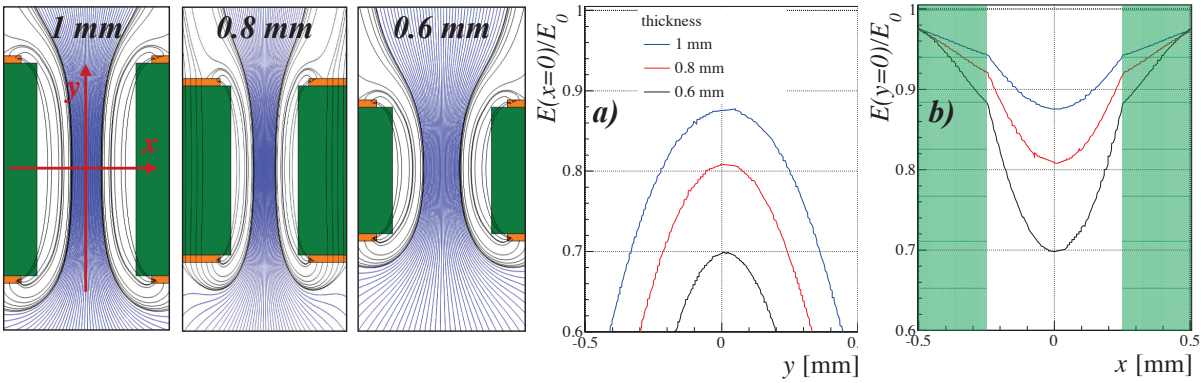

Figure 3.18: Computation of the electric field lines inside a LEM hole for three different thickness of the insulator indicated on the figure (all the LEMs have a rim 80 μm and a hole diameter of 500 μm). The field lines followed by the drifting charges are shown in blue. The two graphs, a) and b), show the ratio of the intensity of the electric field at the center of the hole ($x = 0$, resp. $y = 0$) to the field applied across the electrodes (E_0) as a function of the y (resp. x) coordinates. The shaded green area delimits the hole edges [63].

Chapter 4

Charge readout analysis and study of energy losses in Liquid Argon

The charge readout is crucial for a neutrino experiment seeking for rare events using a liquid argon TPC. The ionization charge deposition depends on the energy losses by the charged particles passing through the active medium. This allows reconstructing the energy of charged current neutrino interactions with argon nuclei. For instance in a charged current interaction of an electronic neutrino the final state will include an electron plus other charged and neutral particles. Neutral particles can interact with the liquid argon or decay by producing secondary charged particles for which it is possible to measure the energy losses. For example photons produced in the decays of neutral pion will produce electromagnetic showers in which all the energy of the initial photon is converted in ionization. For each charged particle ranging out in the active liquid argon volume the integral of the energy losses along its track length will be equivalent to the initial kinetic energy of the particle. By measuring the kinetic energy of all charged particles in the final state after ranging out in liquid argon, it is possible to reconstruct the incoming neutrino energy. In a liquid argon TPC it is possible to measure a particle's energy in three different ways: by measuring the energy deposited in electromagnetic showers by electrons or photons (with a typical resolution $\Delta E/E = 0.33/\sqrt{E[\mathrm{MeV}]} + 0.01$ [71]), by measuring the energy deposition in hadronic showers (typical resolution of $\sigma(E)/E = 0.30/\sqrt{E[\mathrm{GeV}]}$ [42]) or by integrating the energy losses of non showering particles along their tracks (for instance for muons or hadrons not originating hadronic showers the resolution varies from 3.3% up to 1% [72]).

In addition, the measurement of energy losses is very important for the π^0 rejection in the selection of a sample of charged current interactions of electron neutrinos. It allows understanding if an electromagnetic shower is generated by the conversion of a photon resulting from π^0 decay or by a prompt electron. Photon conversions represent the most dangerous background to ν_e CC identification and the measurement of energy losses is an important handle to reject them.

Finally the $\mathrm{d}E/\mathrm{d}x$ measurement can be used for particles identification, essential for identification of exclusive final states and search for proton decay. This can be done

for passing through particles by sampling their trajectory or for stopping particles by measuring the ionization losses in proximity of their stopping point.

In this Chapter it is presented a study of the charge readout analysis: the knowledge of the detector response is critical for this analysis and it requires a deep understanding of several basic aspects, like for instance how the Monte Carlo software simulates energy losses, the charge transport mechanism to the anode plane and the electronic response of the readout apparatus.

First a comparison between a theoretical parametrization of energy loss and the `GEANT` simulation employed for the detector simulation is presented. Then the simulation of detector response is discussed, describing the charge digitization, the effects of the drift and the diffusion, the response of the electronics, the hits reconstruction and the reconstructed energy calculation. Finally a comparison between Monte Carlo production and reconstructed energy is presented: the final analysis is performed for four different levels of the simulation at progressively increased complication in order to appreciate the interplay of different effects.

4.1 The Qscan software

Qscan is a software package based on the `Root` framework and C++, created with the purpose of simulating, reconstructing and visualizing particle trajectories in liquid argon TPC detectors. It was at the base of the ICARUS experiment simulation and reconstruction software and in the last 13 years it has followed a parallel development for dual-phase prototypes applications [72, 73, 74].

Qscan uses `GEANT` to provide Monte Carlo particle simulation: this toolkit simulates particles generation and interaction with matter. `GEANT` provides a large set of physics processes. Depending on the level of detail and physics models, it is possible to enable or disable different electromagnetic or hadronic processes and particle decays via physics list. Concerning interactions with matter a detailed description of the algorithm used to calculate energy losses is discussed in Section 4.2.

Using `Root` geometry package, Qscan can define the geometry of the experimental setup. It can be easily adapted to simulate and reconstruct events in various detector geometries going from DUNE to WA105 and other prototypes. Figure 4.1 shows for example a muon event in the TPC prototype at IPNL, an environment often used for this study for the understanding of basic aspects of charge readout.

After particle and interaction generation via `GEANT`, Qscan deals with the simulation of all physical processes taking place in the detector (for a liquid argon TPC they are described in Chapter 2), including the charge readout effects related to the electronics. The final step of this simulation process is the generation of electrical waveforms and their digitization. All this part of simulation is discussed in detail in Section 4.3.

Finally, data are processed by several reconstruction algorithms, in order to identify physical objects like hits, tracks, showers and events vertexes. Despite the fact each detector can be different from each other, the reconstruction process follows always the following

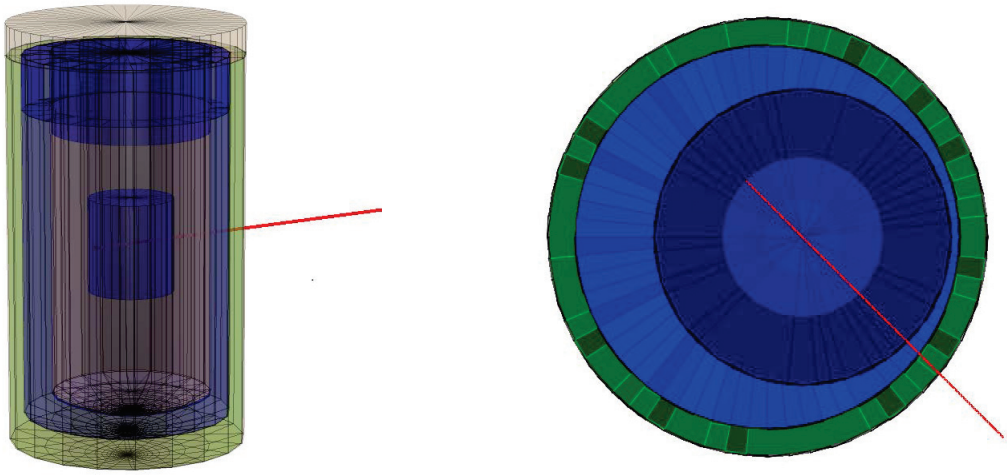

Figure 4.1: Event display of Qscan, showing the 3D (right) and xy (left) views of the prototype at IPNL and a muon passing through the detector.

steps:

1. Reduction of noise and subtraction of baseline processing the raw waveforms.

   In order to suppress noise without modifying too much the signal, two different algorithms may be used: the *Fast Fourier Transform* (FFT) filter and the *coherent noise* subtraction algorithm.

   The FFT filter exploits the fact that induced noise is often dominated by specific frequencies. By applying the Fourier transform to the waveform $V(t)$ it is possible to analyse its transformed waveform $\hat{V}(\omega)$ in order to reduce the noise components. The final waveform, purged from the noise, $V_{filt}(t)$ is obtained applying an inverse Fourier transform to the spectrum of frequencies $\hat{V}_{filt}(\omega)$ after the noise subtraction [75].
   The coherent noise filter is implemented to remove identical noise patterns that are seen on larger sets of readout channels: ideally, this filter subtracts only the noise while keeping the signal unchanged.

2. Hit reconstruction and identification.

   The *hit* is the smallest sub-unit of the reconstructed event: it corresponds to a track segment sampled by a strip. It is built from a group of drift samples having an high level in terms of ADC counts which distinguishes them from the background. A detailed description of the hit reconstruction algorithm is given in Section 4.3.4.

3. Definition of clusters.

   Once hits have been defined, Qscan searches for clusters, regions of densely populated hits that are good candidates for particle trajectories. The hit clustering is the first

step towards a more global reconstruction of the event.

The cluster algorithm is based on the search of directly adjacent hits: starting from a single hit, the *nearest neighbor* (NN) algorithm iterative expands the cluster adding close hit.

4. 2D Track finding.

   After clusters identification, tracks may be built from these. A track is a chain of hits organized in a linear fashion that represents a particle trajectory in a view.

   The basic idea for tracks reconstruction is to convert the problem of finding aligned hits into the trivial problem of finding the highest peak in an histogram representing the fit parameters space. The *Hough Transform* [76] associates each hit in a 2D plane with a curve in a space defined by the parameters ρ and ϑ. For a hit with a given (x, y) it is possible to express a family of lines passing through this point by a set of (ρ, ϑ), as shown in Figure 4.2.

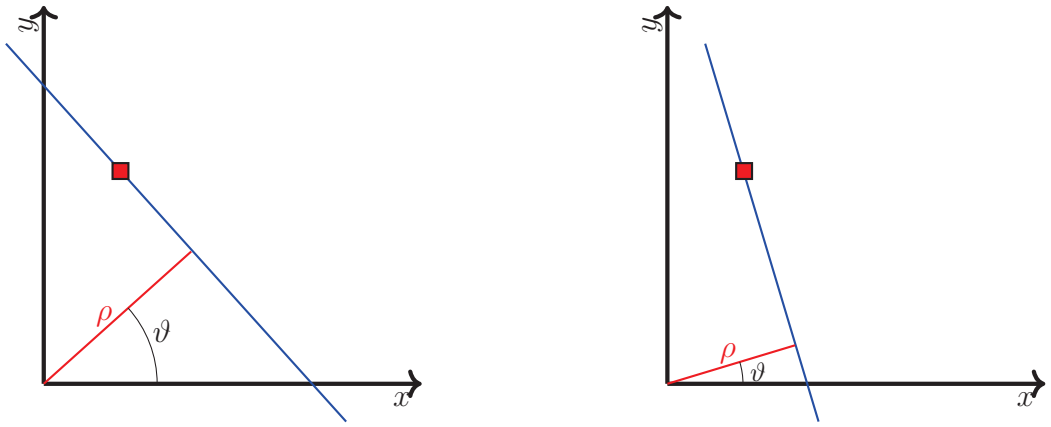

Figure 4.2: (ρ, ϑ) pairs describes two possible lines that pass through a given hit (red box).

A given line can be parametrized by the angle ϑ and the minimal distance to the origin ρ in the following way:

$$\rho = x \cos \vartheta + y \sin \vartheta \tag{4.1}$$

From this, it is possible to conclude that a given point in the image space (x, y) describes a curve in the transformed (ρ, ϑ) space. Furthermore, a point in the transformed space fully defines a line in the image space. Thus, if many hits are brought into the transformed space, the $(\rho_{max}, \vartheta_{max})$ bin where many of the curves intersect are the (ρ, ϑ) values describing lines on which many hits lie.

5. Three dimensional track reconstruction. Finally, an algorithm provides a three dimensional reconstruction of the track by comparing the drift time of the first hits of

track and looping over all two dimensional track candidates until a unique pair of tracks from both views is found.

Figure 4.3 shows an example of Qscan display of an event recorded on a dual-phase prototype 40×80 cm^2 at CERN [77].

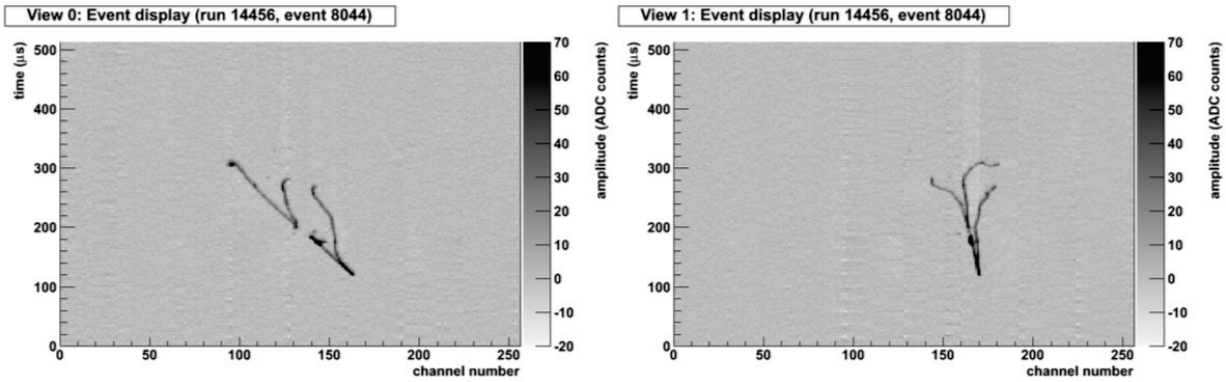

Figure 4.3: Qscan display of an event recorded on a 40×80 cm^2 dual-phase prototype [77].

The studies discussed in this thesis have been performed without using the FFT filter neither the coherent noise filter which were developed in Qscan in order to deal with real data taken in non optimized noise conditions.

At the level of reconstructed events, the only information used in the studies of this thesis is the one provided at the level of hits reconstruction, neglecting the information available from clusters and tracks. The reason of this approach is that the goal of this study is the understanding at the basic level of the source of uncertainties during the energy losses measurements: using the basic information of the reconstruction is possible to understand better the uncertainties related to the charge readout system without being affected by further reconstruction biases at the level of the tracking.

4.2 Energy losses simulation

Simulation and reconstruction of energy losses of a particle passing through liquid argon are fundamental for the particle identification using the mean energy losses $\langle \mathrm{d}E/\,\mathrm{d}x \rangle$. In this paragraphs we will focus on the understanding of the simulation effects which is at the base of the next analysis steps on the charge readout.

As said in Chapter 2 liquid argon is an ideal target material as medium in a TPC because it is dense and that is suitable for rare events searches; in Table 4.1 a summary of the most relevant parameters of LAr as detector medium is presented.

For this study on the energy losses in liquid argon, the reference particles that have been used are obviously muons: in the few GeV energy range of interest for neutrino experiments they loose energy essentially via the continuous ionization losses without radiative losses

Atomic number Z, standard atomic weight	18, 39.948 g/mol
Liquid density	1.40 g/cm^3
Mean excitation energy I	188.0 eV
Average ionization energy W_{ion} (1 MeV e^-)	23.6 eV
Average energy loss for m.i.p.s ($\langle \mathrm{d}E/\mathrm{d}x \rangle_{mip}$)	1.508 MeV cm^2/g
Radiation length X_0	19.55 g/cm^2

Table 4.1: Principal physical properties of liquid argon, from [78].

or interactions. Their large lifetime ($c\tau$ = 658.64 m) ensures that the particle does not decay in the volume where the measurement is performed (a muon with a momentum $p = 100$ MeV/c travels a distance ≈ 627 m before decaying).

Precise measurements of muon energy losses in various materials including liquid argon are easily available as well as their parametrization [79]. The mean stopping power for high energy muons in a material can be described by

$$-\left\langle \frac{\mathrm{d}E}{\mathrm{d}x} \right\rangle = a(E) + b(E)E \tag{4.2}$$

where E is the total energy of the muon. $a(E)$ is the electron stopping power, and $b(E)$ is the term due to radiative processes, including bremsstrahlung, pair production, and photonuclear interactions.

In this study only the electron stopping power term has been taken into account: the radiative contribution start to be important only at high energies (for an incoming muon with $p = 80$ GeV/c, the losses due to bremsstrahlung are 5% of the losses due to ionization). The mean stopping power for muons can be parametrized by using the Bethe-Bloch equation [79]:

$$-\left\langle \frac{\mathrm{d}E}{\mathrm{d}x} \right\rangle = K\frac{Z}{A}\frac{1}{\beta^2}\left[\frac{1}{2}\ln\frac{2m_e c^2\beta^2\gamma^2 T_{max}}{I^2} - \beta^2 - \frac{\delta}{2} + \frac{1}{8}\frac{T_{max}^2}{(\gamma M c^2)^2}\right] + \Delta\left|\frac{\mathrm{d}E}{\mathrm{d}x}\right| \tag{4.3}$$

where $K = 0.307$ MeVcm/g, Z and A are respectively the atomic number and the atomic mass of the medium, I is the mean excitation energy. T_{max} is the maximum energy that can be transferred from the traversing particle with mass M to a single electron with mass m_e:

$$T_{max} = \frac{2m_e c^2\beta^2\gamma^2}{1 + 2\gamma m_e/M + (m_e/M)^2} \tag{4.4}$$

The term δ in Equation 4.3 is a density effect correction: when the particle energy increases its electric field flattens and extends, so distant collisions become more important. For low

energies the density effect is not relevant; the density effect correction is usually described by Sternheimer's parametrization

$$\delta(\beta\gamma) = \begin{cases} 2(\ln 10)x - \overline{C} & \text{if } x \geq x_1 \\ 2(\ln 10)x - \overline{C} + a(x_1 - x)^k & \text{if } x_0 \leq x < x_1 \\ 0 & \text{if } x < x_0 \end{cases} \tag{4.5}$$

where, in the case of liquid argon $x = \log_{10}\beta\gamma$, $x_0 = 0.201$, $x_1 = 0.196$, $k = 3$ and $\overline{C} = 5.217$.

The term $(1/8)(T_{max}/(\gamma Mc^2)^2)$ takes into account spin effects. Its contribution to the stopping power asymptotically approaches $0.038(Z/A)$ MeV cm/g.

For high energy muons, the radiative losses contribution is taken into account: this contribution is given by the last term in Equation (4.3):

$$\Delta\left|\frac{\mathrm{d}E}{\mathrm{d}x}\right| = \frac{K}{4\pi}\frac{Z}{A}\alpha\left[\ln\frac{2E}{Mc^2} - \frac{1}{3}\ln\frac{2T_{max}}{m_e c^2}\right]\ln^2\frac{2T_{max}}{m_e c^2} \tag{4.6}$$

This term is important at high energies, amounting to 2% of the electronic loss at 100 GeV/c. In Figure 4.4 is possible to see the effects of this term on the energy losses. This correction has the effect of increasing total energy losses for incoming particles beyond 10 GeV/c.

As mentioned in Section 4.1 the simulation of particles generation and interactions is implemented by `GEANT` software: in this work two different versions of `GEANT` had been compared for the muon energy losses in liquid argon: `GEANT3` and `GEANT4`.

To simulate energy depositions, `GEANT` divides the path traveled by the particle in equal steps and for each step it evaluates the amount of energy deposited. The size of the steps is tunable by the user: for this study, the step size used is 0.05 cm, the default value used by Qscan.

The energy losses calculation has some small differences between `GEANT3` and `GEANT4`.

`GEANT3` simulates the energy losses by using the following formula:

$$-\left\langle\frac{\mathrm{d}E}{\mathrm{d}x}\right\rangle = K\frac{Z}{A}\frac{1}{\beta^2}\times \left[\frac{1}{2}\ln\frac{2m_e c^2\beta^2\gamma^2 T_{upp}}{I^2} - \frac{\beta^2}{2}\left(1 + \frac{T_{upp}}{T_{max}}\right) - \frac{\delta}{2} - \frac{C_e}{Z}\right]\times \left(-\frac{4.993\dot{1}0^{-6}\ \text{GeV}}{T_\mu}\right) \tag{4.7}$$

The ionization energy I is defined as $I = 16(Z)^{0.9}$ eV $= 215.7$ eV: the little difference of this value with respect to the one reported in the literature is not relevant. $T_{upp} = \min\{T_{cut},\ T_{max}\}$, where T_{cut} is a tunable parameter and represents the cut-off energy for the simulation of δ-rays production. C_E/Z is a shell correction term which takes into account the fact that at low energies for light elements the probability of particle-electron collision

at deep electronic layers is negligible. Barkas [80] provided a semi-empirical formula which is applicable to all materials:

$$C_e/Z = \left(0.42237(\beta\gamma)^{-2} + 0.0304(\beta\gamma)^{-4} - 0.00038(\beta\gamma)^{-6}\right) \cdot 10^{-6} I^2 + \left(3.858(\beta\gamma)^{-2} - 0.1668(\beta\gamma)^{-4} + 0.00158(\beta\gamma)^{-6}\right) \cdot 10^{-9} I^3 \quad (4.8)$$

It is important to remark that Equation (4.7) is the formula implemented in the GEANT3 code, and it presents some small differences form the equation for energy losses presented in the GEANT3 manual [81].

In Figure 4.4 are shown the two different energy losses parametrizations as a function of muon momentum: the two equations give the same values in the range for low momentum values until $\approx$ 4 GeV/c. One can note that GEANT3 parametrization (black curve) does not take into account any radiative term: it is very close to the parametrization given by [79] without the corrective term (4.6) (dashed red line). The standard parametrization including the radiative term produces as result higher energy losses for high momentum values (continuos red line).

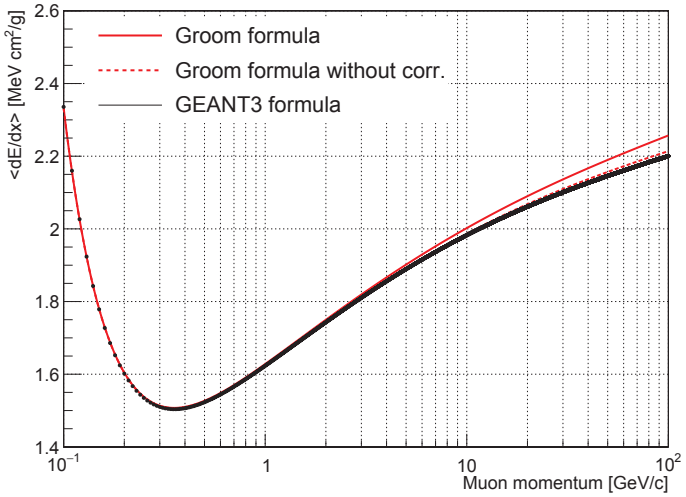

Figure 4.4: Comparison between standard parametrization of energy losses given by [79] including ionization and radiative term (continue red line), only ionization term (dashed red line) and energy losses calculated by GEANT3.

The energy losses computed in GEANT4 are quite different from those calculated by GEANT3 : in fact, in GEANT4 they are computed by a C++ class which constructs and fills in a table with the values for different particles and materials [82].

Both GEANT3 and GEANT4 allow selecting the type of energy loss to be used in the simulation: for this study it had been chosen to take into account only the losses due to ionization processes, deactivating all the radiative processes (bremsstrahlung, pair production and photo-nuclear interaction).

GEANT allows also simulating and managing energy loss fluctuations: three options are implemented:

- *No fluctuations*: this is the basic case: there are no fluctuations in the energy deposition;
- *Fluctuations*: the energy losses are affected by fluctuations. The energy loss probability distribution is adequately described by the Landau-Vavilov distribution [81];
- *δ-rays production*: muons in liquid argon produce δ-rays above the energy T_{cut} mentioned above.

For this study three sets of Monte Carlo samples had been produced, increasing progressively the complexity of the energy loss process: the first sample had been produced without fluctuations, in order to verify the correspondence between the GEANT production and the parametrization proposed by Groom. Then, in order to make the simulation realistic, fluctuations had been added and finally the cutoff value for the δ-rays production T_{cut} had been set to the minimum, corresponding to 10 keV.

The mean energy loss has been calculated as the energy deposited in the active volume divided by the distance travelled. The muons have been produced with the same initial position, parallel to the cathode and anode planes (*i.e.* parallel to the readout charge apparatus), at the beginning of the active volume, with a planar angle of 45° with respect to the strip orientation, in order to be symmetric for the two views. With these initial settings particles cross all the diameter of the active volume, equivalent to a distance of 27.15 cm. Muon samples have been produced at various initial momenta and for each momentum value the sample is composed by 1000 events.

In Figure 4.5 are shown the mean energy losses $\langle \mathrm{d}E/\,\mathrm{d}x \rangle$ as a function of muon momentum for the Monte Carlo simulation performed using GEANT3 (left) and GEANT4 (right). In the case of GEANT3 the production without fluctuations (red dots) agrees with the implemented Equation (4.7). The production with fluctuations (blue dots) follows the prevision until $p_\mu \approx 30$ GeV: at high energies fluctuations underestimate the mean value of energy loss.

When the δ-rays production (green dots) is activated the mean energy loss values is dramatically lower than in the other cases: this is due to the fact that to activate the δ-rays production, it is necessary to change the value of T_{cut}: for this production the value used is $T_{cut} = 10$ keV and this changes also the trend of the function described by equation (4.7). The Monte Carlo simulation performed using GEANT4 shows that the generation of the energy losses without fluctuation has some small differences with respect to GEANT3: this is due to the different way of generating the energy losses. The fluctuations sample presents no anomalies for high momentum values. Finally the δ-ray production is very similar to the one obtained with GEANT3.

It is interesting to note that the energy losses for $p_\mu = 200$ MeV/c do not follow the theoretical predictions: this is due to the fact that during its path in the liquid argon, the muon decreases its momentum and on this branch of the Bethe-Block curve this implies a considerable increase of the energy losses.

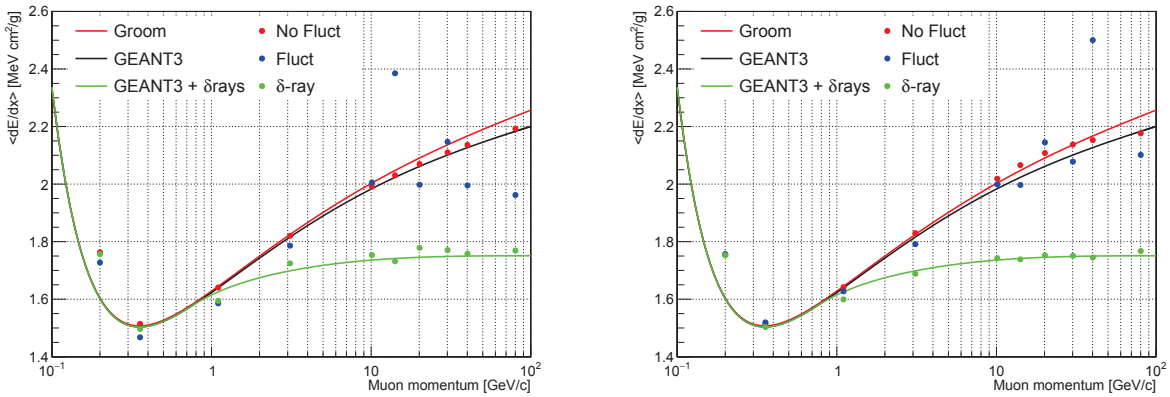

Figure 4.5: `GEANT3` (left) and `GEANT4` (right) Monte Carlo simulation in the case of no fluctuations (red dots), fluctuations (blue dots) and δ-rays production (green dots).

In what follows, all the results shown had been obtained using `GEANT4`: in fact, as Figure 4.5 shows, `GEANT4` manages better the fluctuation processes.

4.3 Simulation of detector response

After energy losses simulation, Qscan simulates all the physical processes which occur in the liquid argon TPC (described in Chapter 2). In addition it simulates also the charge detection by the readout and its digitization. In the following all the steps of the simulation of detector response are shown.

The goal of this work is to study just the charge reconstruction: for this reason the light production derived from scintillation in liquid argon is not taken into account. However it is assumed that its measurement can be used in order to know the time corresponding to the start of the drift t_0 in order to compute the drift distance in each event. This time can be known also from the beam trigger information in both WA105 and DUNE.

4.3.1 Charge digitization

The energy deposited in each step by a charged particle via ionization losses is converted by the simulation in a large number of electron-ion pairs by considering an effective ionization potential W_{ion}. Part of this charge undergoes an immediate recombination by producing the UV light which is then used for triggering. The remaining charges are then available for the drift and collection by the anode and cathode. The fraction of electron-ion pairs surviving recombination is a function of the electric field present in the drift region. This fraction has been measured by the ICARUS [49] experiment.

As described in Chapter 2 the ionization charge produced by a passing through particle is then practically proportional to the energy deposited: Qscan evaluates for each step the ionization charge Q_{step} produced:

$$Q_{step} = \mathcal{R}_{step} \frac{E_{step}}{W_{ion}} \tag{4.9}$$

where E_{step} are the energy losses in each single step and $\mathcal{R}_{step}$ is the recombination factor calculated for each step, evaluated using the Birks law [48]:

$$\mathcal{R}_{step} = \frac{A}{1 + \frac{k}{\mathcal{E}} \frac{E_{step}}{step}} \tag{4.10}$$

with the parametrization calculated by the ICARUS collaboration [49] and by replacing $\langle \mathrm{d}E/\,\mathrm{d}x \rangle$ with the rate of the energy deposited in each step with respect to the step size. The value of the electric field used for this study is $\mathcal{E} = 1$ kV/cm. Figure 4.6 shows the recombination factor $\mathcal{R}$ as a function of the mean energy loss $\langle \mathrm{d}E/\,\mathrm{d}x \rangle$ for two different values of electric field.

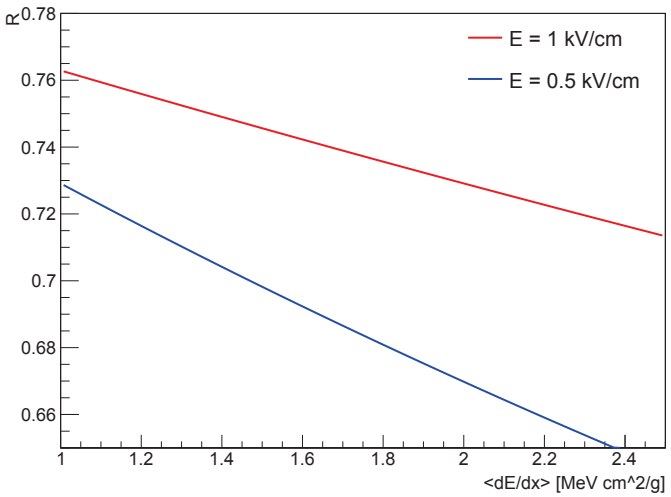

Figure 4.6: $\mathcal{R}$ as a function of energy losses $\langle \mathrm{d}E/\,\mathrm{d}x \rangle$ for an electric filed $\mathcal{E} = 1$ kV/cm (red line) and for $\mathcal{E} = 0.5$ kV/cm (blue line).

4.3.2 Drift and diffusion

This section discusses the transport of the electrons from the ionization point to the anode. The charge corresponding to the electrons which do not recombine at the production point

is attenuated, depending on the liquid argon purity and the drift distance to anode, since part of it is absorbed by the electronegative impurities found along the drift path. This charge is then diffused longitudinally and transversely and finally collected by the 2D anode readout plane.

As described in Chapter 2, the charge $Q(t_d)$ which survives after a drift time t_d is given by the equation:

$$Q(t_d) = Q_0 \, \mathrm{e}^{-\frac{t_d}{\tau_e}} \tag{4.11}$$

where Q_0 is the charge and τ_e is the mean electron lifetime. As shown by the equation (2.8) τ_e depends on the amount of impurities in liquid argon.

Figure 4.7 shows the charge distribution per strip in case on an infinite lifetime (blue histogram) and for a lifetime of 3 ms with the respective Landau fits to evaluate the most probable value of the distributions.

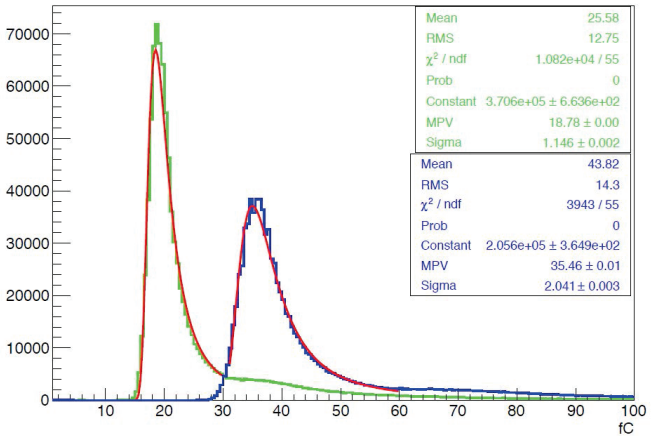

Figure 4.7: Charge distribution per strip in case of an infinite electrons lifetime (blue histogram) and for a lifetime of 3 ms (green histogram).

The distance travelled by the drifted electron influences then the quantity of charge reaching the readout plane. In Figure 4.8 are shown charge distributions corresponding to different drift distances of passing through muon.

The liquid argon purity can be precisely measured by dividing the length of cosmic ray tracks (with measured t_0) in samples at difference drift distances and then by fitting the attenuation profile with an exponential function describing the electrons lifetime. This procedure, with enough statistics, allows correcting completely for attenuation effects. It is important to stress that this procedure for the purity measurement is relevant for very high purity conditions (typically greater that the 3 ms assumed as the basic purity requirement for the operation of the WA105 and DUNE detectors). For lower purity conditions, which generate larger attenuation of the charges, the LAr purity is measured by dedicated purity monitors submersed at various heights in the liquid argon volume outside the field cage which provide information independently on the charge readout analysis. For very good

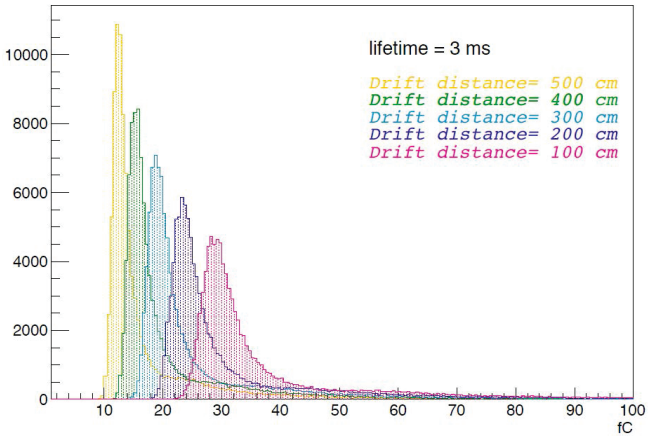

Figure 4.8: Reconstructed charge per strip for various drift distances. For this distribution $\tau_e = 3$ ms.

purity conditions the purity monitors measurements saturate and for this reason it is needed to use the information from the charge attenuation measurement along tracks which saturate at higher purity values.

Another important effect affecting the charge during the drift is the diffusion, which spreads the size of the electron cloud moving to the anode. As discussed in Chapter 2 the size of diffusion is calculated at the anode for a given drift time t_d as:

$$\sigma_{T,L}^2 = 2D_{T,L}t_d \tag{4.12}$$

and the size of the electron cloud arriving at the anode in the longitudinal (along the drift direction) and transverse direction is given by:

$$Q(r,\, z) = Q_f \, \mathrm{e}^{-z^2/(4D_L t_d)} \, \mathrm{e}^{-r^2/(4D_T t_d)} \tag{4.13}$$

In order to compute the charge collected by each strip, Qscan samples the drift in several slices and calculates a set of weights for each time slice:

$$w(t_i) = \frac{1}{\sigma_L/v_d\sqrt{2\pi}} \int_{t_i}^{t_i+T} \exp\left(-\frac{(t_0-t)^2}{2\sigma_T^2/v_d^2}\right) \mathrm{d}t \tag{4.14}$$

where t_0 is the nominal time expected for the drift, $T = 1/f_{ADC}$ is the sampling period and v_d is the nominal drift velocity. For each time slice the software calculates weights for spatial distribution in two steps. To calculate the weight for y i-th coordinate, for instance, first the weight on the y coordinate is calculated:

$$w_y(t_i) = \frac{1}{\sigma_T\sqrt{2\pi}} \int_{strip} \exp\left(-\frac{(y_0-y)^2}{2\sigma_T^2}\right) \mathrm{d}y \tag{4.15}$$

where y_0 is the nominal y coordinate expected and the integral is calculated over all the strip length. The weight for the x i-th coordinate is:

$$w_{x,j}(t_i) = w(t_i) \times w_y(t_i) \times \frac{1}{\sigma_T\sqrt{2\pi}} \int_{pitch} \exp\left(-\frac{(x_0 - x^2}{2\sigma_T^2}\right) \mathrm{d}x \tag{4.16}$$

where the integral is calculated over the strip width (*i.e.* the pitch size). The reason for choosing this integral region is that the strip which provides the x (or y) coordinate is sensitive to all the charge deposited in the strip. This is why the diffusion on the perpendicular coordinate needs to be taken into account. The charge collected on the j-th strip in the j-th time slice is:

$$Q^x_{j,i} = Q_f \cdot w_{x,j}(t_i) \tag{4.17}$$

Figure 4.9 shows the reconstructed track for a cosmic muon without (left) and with (right) diffusion effects.

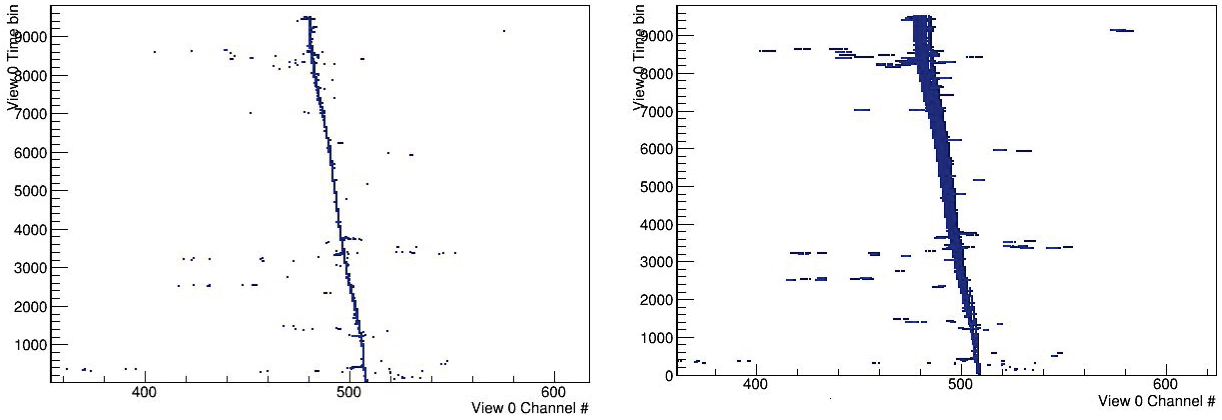

Figure 4.9: Cosmic muon track crossing the detector without (left) and with (right) diffusion effects.

Another factor which modifies the transported ionization charge during the travel to the anode is given by the presence of the LEM: it multiplies the drifting electrons through a probabilistic process, providing a tunable gain, depending on electric field in the LEM.

GARFIELD simulations with the LEM geometry allow reproducing the experimental results on the LEM gain as a function of the voltage difference applied on the two sides. In Figure 4.10 are represented the distributions of the number of secondary electrons exiting the LEM for a single electron in input for two different voltages applied 3 kV and 3.5 kV. Conventionally for voltage difference of 3 kV applied on a LEM printed circuit board of 1 mm thickness one speaks about an electric field of 30 kV/cm. However the field really present inside the LEM holes is not uniform and lower than this value which would correspond to a parallel plates capacitor geometry.

The number of secondary electrons produced in the simulation can be fitted with an exponential function. By defining the gain as the number of electrons transferred to the

collection region per input electron, it is possible to parametrize the gain shape for a fixed electric field with an exponential function with a constant corresponding to the average gain which is 12 for 3 kV and 106 for 3.5 kV. For a single electron in input the number of electrons produced by the avalanche has large variations, as shown by the exponential distribution. However in the real case the number of input electrons per hole is of the order of 1000 for a particle at the ionization minimum. So the fluctuations in the avalanche process are largely averaged over the electrons input statistics and the gain is quite well precisely defined and not affected by relevant statistical fluctuations. The LEM thickness affects the intensity of the electric field inside the holes, a thickness variation of 5% may induce a gain variation of 50%. Despite very stringent requirements on the LEM thickness (1 mm with 40 μm tolerance), the gain may have some small local variations depending on the LEM printed board thickness. These gain variation can be measured by using the same sample of tracks used for the purity measurement once the purity has been measured and corrected for.

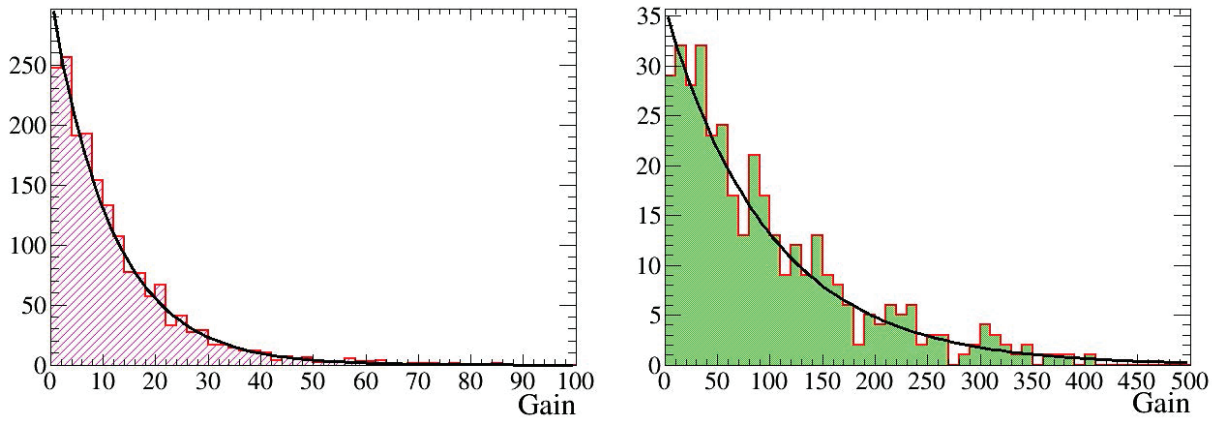

Figure 4.10: GARFIELD simulations of the LEM gain in avalanches with a single electron in input. The two distributions of the number of secondary electrons produced by the avalanches are computed for different values of the potential difference applied to the two faces of the LEM: 3 kV (left) and 3.5 kV (right).

In summary there is a well established procedure which has been set-up in WA105 in order to measure the attenuation losses during the drift and eventually after the LEM gain by using samples of cosmic ray tracks. This procedure can bring enough statistics to a measurement of the lifetime of the electrons in liquid argon and of the LEM gain and to the definition of related corrections which can be applied to the experimental data, so that these effects do not have significant impact at the level of systematic biases or resolution for the energy losses measurements. So these effects related to the transport of the charges from the production point to the anode can be neglected at the level of the evaluation of the other effects affecting the energy reconstruction. In order to perform a direct evaluation of the readout effects during the reconstruction, in this work the effects related to impurity

losses, diffusion and gain have been switched off assuming their complete correction by the dedicated experimental measurements.

4.3.3 ADC conversion

The charge readout is quantized in time: the simulated electronics divides the charge in time samples along the drift coordinate (of the size of 400 μs). The software evaluates the amplitude generated by the charge contained in each drift sample. The relation between the amplitude and charge is given by a response function which simulates the electronics used to amplify the collected charge. The response function used in this study is the one originally implemented in Qscan and given by the following equation:

$$f(t) = \begin{cases} \dfrac{q \cdot Cal}{\delta t(\tau_D - \tau_I)^2} \mathrm{e}^{-\frac{t}{\tau_I}} \{[t(\tau_D - \tau_I) + (2\tau_D - \tau_I)\tau_I] + \\ -\mathrm{e}^{-\frac{\delta t}{\tau_I}} [t(\tau_D - \tau_I) + 2\tau_D\tau_I + \delta t(\tau_I - \tau_D)] & \text{if } t - \delta t > 0 \\ \dfrac{q \cdot Cal}{\delta t(\tau_D - \tau_I)^2} \mathrm{e}^{-\frac{t}{\tau_I}} [t(\tau_D - \tau_I) + (2\tau_D - \tau_I)\tau_I] + \\ -\mathrm{e}^{-\frac{t}{\tau_D}} \left[\mathrm{e}^{\frac{t}{\tau_D}} (\tau_D - \tau_I)^2 - 2\tau_D^2 \mathrm{e}^{-\frac{\delta t}{\tau_D}}\right] & \text{if } t - \delta t < 0 \end{cases} \tag{4.18}$$

where q represents the charge (in fC), τ_D and τ_I are the differentiation and integration times of the CR-RC shaper, δt is a parameter which defines the waveform and Cal is the calibration term which converts the charge into ADC counts, namely $Cal = 65.0296$ ADC μs/fC.

This function implemented in Qscan simulates a typical front-end electronics response, like the one used for instance in the 3L ETHZ TPC prototype at CERN. New front-end electronics has been developed for WA105 but the response function is very similar to the one originally implemented in Qscan and therefore used for this study. The response function provides the amplitude in ADC counts, approximating the transfer function of the charge integrator with the RC feedback, the RC-CR shaper and the additional amplifier before the signal digitization [74]. Figure 4.11 shows the response of the simulated electronics using Equation (4.11) for a charge of 1 fC for different values of δt (the value used for this study is $\delta t = 0.5$ μs).

After the time digitization of the charge based on the response function, Qscan introduces the white noise generated by the electronics. This noise is parametrized as a Gaussian distribution with a tunable RMS. In this work two cases have been studied: the simplest one without noise generation, and the case with a variance equal to 3 ADC counts, which corresponds for unitary gain to a single-phase readout. After the noise addition, the signal is quantized in ADC counts by taking the integer part of the computed amplitude.

4.3.4 Hit reconstruction

Once the digitization process ends, Qscan provides the reconstruction of the event. The algorithm allows to build the hits by analysing the signal and by performing a loop over

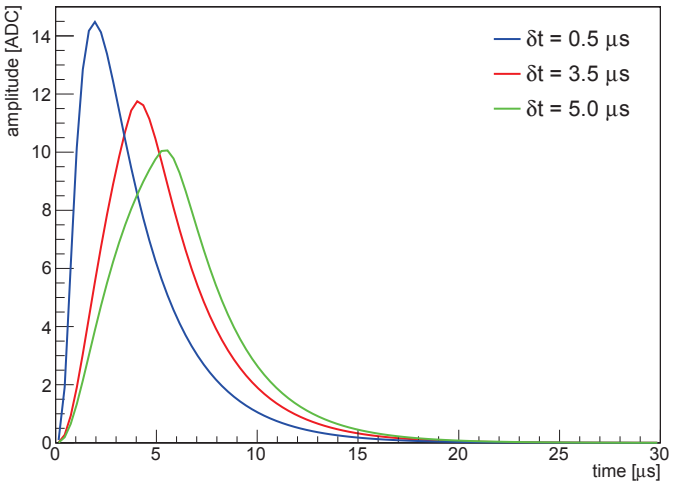

Figure 4.11: Response function (4.18) for different values of δt.

the drift samples for each strip:

- the first drift sample on the hit is the one whose ADC counts exceed a lower threshold th_1, which is set by the user. It is possible to set an absolute value for th_1, or a value relative to the RMS used to generate the noise;
- if the ADC counts for a drift sample fall below a second threshold th_2 (defined in the same way a th_1), the hit's final drift sample is set at the previous sample, and the width is checked. If the width is larger than a minimum number of drift samples, then the hit is confirmed;
- if before the end of the loop the ADC counts grow up again and exceed th_2 a new hit is generated;
- when the ADC counts fall again below th_2 the second hit ends. As in the case of the first hit, if the width is larger than a minimum number of drift samples, then the hit is confirmed.

For this study the values of the thresholds have been set to 1 ADC counts if the noise production was deactivated, and 2 RMS ADC counts if the noise production was activated (see Section 4.4 for the different samples used in this study). In Figure 4.12 is shown a schematic representation of the hit reconstruction process.

Figure 4.13 shows a comparison between the total charge collected per strip for a muon event in WA105 (left) and the reconstructed charge in the same event by summing all hits belonging to the same strip (right). A LEM gain of 20 is assumed in the simulation, corresponding to an effective gain per view of 10 after charge sharing on the two collection

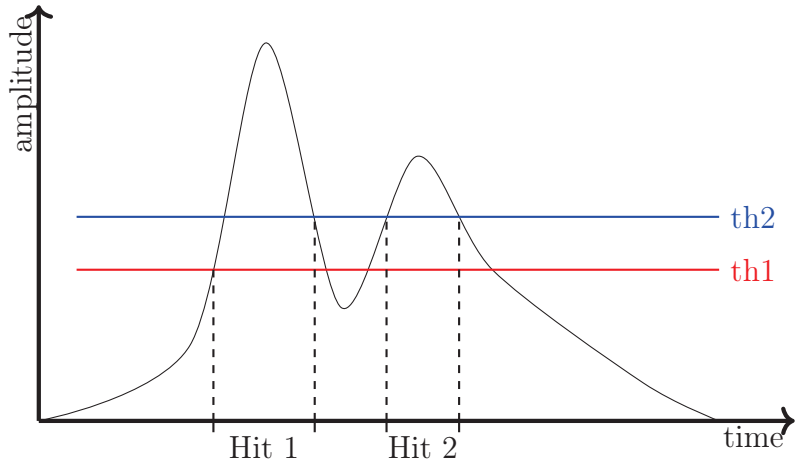

Figure 4.12: Schematic representation of a waveform for a strip. The first hit starts when the signal exceeds th_1 (red line) and end when it falls below th_2 (blue line). The second hit on the strip starts when the signal exceeds th_2 and ends when the ADC counts falls below th_2.

views. The muon is crossing the detector parallel to the anode plane and it has an angle of 45 degrees with respect to the two collection views. There is a good agreement between the collected and reconstructed charge distributions, which shows that the hits reconstruction provides an accurate measurement of the collected charge.

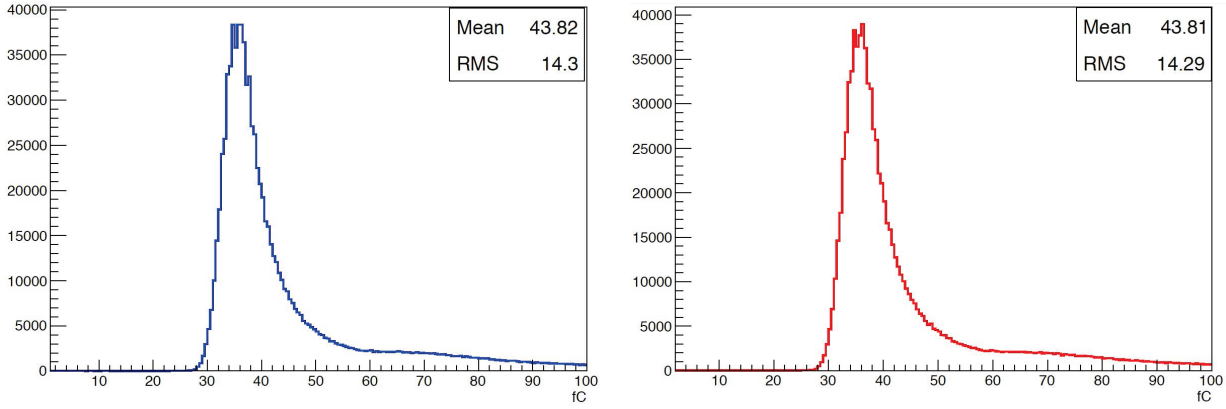

Figure 4.13: Examples of distributions of collected (left) and reconstructed charge (fC) (right) per strip for a muon crossing the detector parallel to the anode plane and at 45 degrees with respect to each view

4.3.5 Energy reconstruction

At this point of the reconstruction, the collected charge from the initial ionization generated by the passing through particle has been reconstructed in several hits, which provide information about the original position of the particle: the strips in the two views where the hits have been reconstructed provide the xy position of the 3D hits while the time of the hits samples with respect to the event t_0 gives its z coordinate.

The reconstructed charge of each hit is computed by integrating the signal waveform samples between the first and the last drift time samples belonging to the hit, namely:

$$Q_{reco} = \frac{\text{Hit integral}}{Cal} \tag{4.19}$$

where Cal is the calibration term defined in Section 4.3.3 which accounts for the conversion factor of the charge into ADC counts corresponding to the integral over all the samples of the hit. In the real detector implementation this constant can be individually calibrated for each channel at the 1% level by using charge injection in the front-end amplifiers.

It is important to remark that Q_{reco} represents a measurement of the residual part of the charge produced by the ionization *after* this one has been undergoing the quenching recombination. The corresponding reconstructed energy is given by the following relation:

$$\begin{aligned} E_{reco} &= W_{ion} Q_{reco} \\ &= W_{ion} \frac{\text{Hit integral}}{Cal} \end{aligned} \tag{4.20}$$

This quantity, affected by recombination effects, cannot be directly compared to the real deposited energy in `GEANT` (presented for instance in Figure 4.5 during the discussion on the energy losses).

This is due to the fact that the recombination factor applied by the simulation $\mathcal{R}$ is computed by `GEANT` individually for each step depending on the amount of deposited charge in the step. This information is unknown at the reconstruction level where many steps contribute to the same hit and only an average quenching correction treatment will be practically applicable.

For this reason, in a first instance in this study E_{reco} will be directly compared to the energy losses simulated by `GEANT4` inclusive of the effect of the quenching losses. This procedure will allow evaluating the energy measurement systematics related to the hits reconstruction and the inversion of the response function alone, independently on the problematic related to treatment of the quenching corrections.

In a second phase, an evaluation of the quenching factor from the reconstructed energy will be performed and applied. The energy reconstruction systematics including quenching unfolding will be correspondingly re-evaluated.

4.4 Reconstruction effects on energy losses measurement

The comparison between the reconstructed energy E_{reco} and the Monte Carlo energy deposited calculated after the recombination E^q_{MC} is studied in four cases of increasing complication of the simulation, progressively adding various effects:

1. *Basic case*: the energy loss simulation and reconstruction are not perturbed by any effects (δ-rays production and fluctuations are deactivated in the generation process and the noise due to the electronics is set to 0);

2. *noise case*: electronics noise generation is added to the simulation;

3. *fluctuations case*: energy fluctuations are activated and simulated using a Landau-Vavilov distribution;

4. *δ-rays case*: δ-rays production is activated. This last case is the one corresponding to the closest simulation to the real detector.

In all these simulations, in order to keep the energy losses analysis as simple as possible and just focused on the unfolding of the reconstruction effects, radiative processes and multiple scattering are deactivated.

The Monte Carlo average $\langle \mathrm{d}E/\,\mathrm{d}x \rangle$ is calculated as the sum of all quenched Monte Carlo energy depositions in the active volume divided by the distance travelled in the same volume. The absence of multiple scattering ensures in that respect a straight path, while the absence of radiative processes ensures that all the energy is contained.

The reconstructed average $\langle \mathrm{d}E/\,\mathrm{d}x \rangle$ is calculated by summing the hits over all the strips and dividing this sum by the distance covered by the strips.

Considering the setting used in the MC generation, particles cross the readout plane along the diagonal: in this way, the region covered by the strips is exactly the diameter of the active volume.

In Figure 4.14 are shown the Monte Carlo and reconstructed $\langle \mathrm{d}E/\,\mathrm{d}x \rangle$ for the four different cases: in all cases the reconstruction process gives a lower value of the reconstructed energy with respect to the Monte Carlo values. Table 4.2 shows the deviation, defined as $(E^q_{MC} - E_{reco})/E^q_{MC}$, for the 4 different cases. The deviations are all positive: it means that there is a systematic effect that brings to underestimate the reconstructed energy. This effect can be related to the quantization of the charge during the ADC conversion and the hits reconstruction which defines a certain number of samples associated to the hit.

It is interesting to note how the systematic deviation in the basic simulation case is larger than in the other cases. The noise and the fluctuations tend to smear the signal, equilibrating the effect of the systematic underestimation. In the case of δ-rays production the bias is due to the production of electrons that could radiate secondary photons.

Now it is possible to discuss the complete comparison among the ionization energy losses of the muons and the equivalent reconstructed quantity. This comparison implies the unfolding of the quenching effects. In order to compare the reconstructed energy to

Case	deviation (%)
Basic case	0.309
Noise case	0.030
Fluctuations case	0.031
δ-rays case	0.255

Table 4.2: Reconstructed energy deviation with respect to the simulated energy for the 4 progressive levels of complication of the simulation.

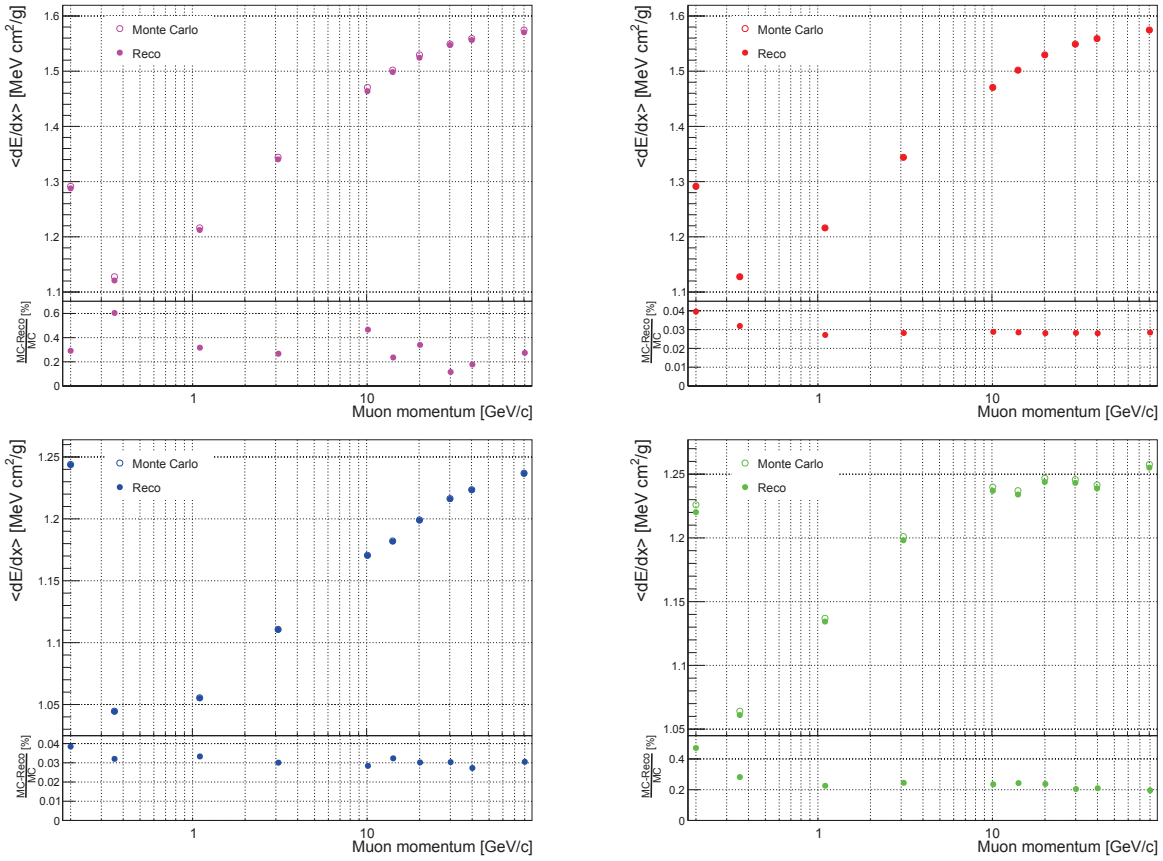

Figure 4.14: Monte Carlo $\langle \mathrm{d}E/\mathrm{d}x \rangle$ (empty dots) and reconstructed $\langle \mathrm{d}E/\mathrm{d}x \rangle$ (full dots) for the 4 different scenarios: basic case (top left), noise case (top right), fluctuations case (bottom left) and δ-rays production case (bottom right). All these measurement are affected by quenching recombination.

the original Monte Carlo energy losses, *i.e.* the energy deposited by the passing through muons, it is necessary to compute an average recombination factor from the reconstructed energy and correct the reconstructed energy for it.

The relation between the reconstructed energy corrected for the recombination effect E_{reco}^{corr} and the reconstructed energy E_{reco} value which is at the output of Qscan is given by:

$$E_{reco}^{corr} \cdot \mathcal{R}_{reco} = E_{reco} \tag{4.21}$$

where $\mathcal{R}_{reco}$ is an empirical approximation of the real $\mathcal{R}$ which affected the recombination processes for the charges contributing to a given hit:

$$\mathcal{R}_{reco} = \frac{A}{1 + \dfrac{k}{\mathcal{E}\rho}\dfrac{E_{reco}^{corr}}{d}} \tag{4.22}$$

where A and k are defined in Chapter 2, $\mathcal{E}$ is the electric field in the TPC, ρ is the liquid argon density and d is the distance travelled by the particle over the strip corresponding to the hit.

By inverting the formula (4.21), it is possible to determine E_{reco}^{corr} for each reconstructed hit:

$$E_{reco}^{corr} = \frac{E_{reco}}{A - \dfrac{E_{reco} k}{\mathcal{E}\rho\, d}} \tag{4.23}$$

In this study the distance d is known by construction from the Monte Carlo generation settings ($d = 0.3\text{ cm}\sqrt{2} = 0.424$ cm). In a generic case of events from real data, where the particle direction is unknown, d should be evaluated using additional information from the track reconstruction.

In Figure 4.15 are shown the Monte Carlo and reconstructed $\langle \mathrm{d}E/\,\mathrm{d}x \rangle$ once corrected for the quenching effect as explained above.

Looking at the deviations in Table 4.3, it is possible to note that the reconstruction, after the empirical correction for the quenching effect, produces results worse than in previous cases when quenching effects were disentangled at the generation level.

This is due to the fact that the quenching factor $\mathcal{R}_{reco}$ is evaluated over a strip of 0.3 cm, whereas the quenching factor $\mathcal{R}_{reco}$ calculated during the Monte Carlo Simulation is applied at microscopic level over a step size of 0.05 cm. Quenching effects are very sensitive to large charge depositions confined in very small volumes. The microscopic corrections tends to dump cases of very high concentrations of charge. This explains also the very large bias obtained in the fluctuations case of the simulation: in this case the fluctuations at Monte Carlo level are essentially concentrated along the track direction and generated over single steps, producing very high quenching factors in the simulation. The reconstructed energy is instead the result of the sum of all these contributions integrated along the strip. From the average reconstructed energy on a strip it is impossible to reproduce the very high quenching factors computed during the simulation. The case with

δ-rays simulation is the one closer to the experimental reality. Also δ-rays can produce localized ionization depositions corresponding to high quenching factors. However this process is more dispersed that the simulation without delta-rays simulation where fluctuations were essentially treated along the track direction generating steps with very high specific ionization. The comparison among these two cases is illustrative of the treatment of the recombination effects and shows that for real events the correction of quenching effects is a real systematic issue to be taken into account in the reconstruction of the real energy deposited by ionizing particles in liquid argon.

Case	deviation (%)
Basic case	0.313
Noise case	0.209
Fluctuations case	18.223
δ-rays case	3.345

Table 4.3: Deviations of the reconstructed energy with respect to the simulated deposited energy including quenching unfolding for the 4 different simulation configurations.

4.5 Summary

The study of the charge readout and of the energy losses in liquid argon points out a few systematic aspects which have to be taken into account in the simulation and in the reconstruction in order to achieve an accurate reconstruction of the energy losses.

First of all it has been verified in details the accuracy of the simulation of the energy losses with respect to the best experimental knowledge provided by the reference parametrizations. The best results are obtained with the `GEANT4` based Qscan simulation, which has been then frozen for the continuation of all the other studies. While `GEANT3` underestimates energy losses with fluctuations for high momenta on incoming muons, `GEANT4` gives goods results for all the simulations over all the momentum range.

Since the goal of this Chapter is to study the basic performance of the charge readout and the energy losses reconstruction, some simulation effects related to the detector response during the transport of charges from the generation point to the anode (attenuation during the drift due to electronegative impurities, diffusion, gain due to the multiplication in the LEM) have been deactivated, relying on their correction based on experimental measurements on samples of cosmic ray tracks, which is a well established technique.

The aspects taken into account for this analysis are directly related to the simulation of the response of the readout system, through the response function of the electronics and the digitization of the signal, and the hit reconstruction algorithm. The inversion of the

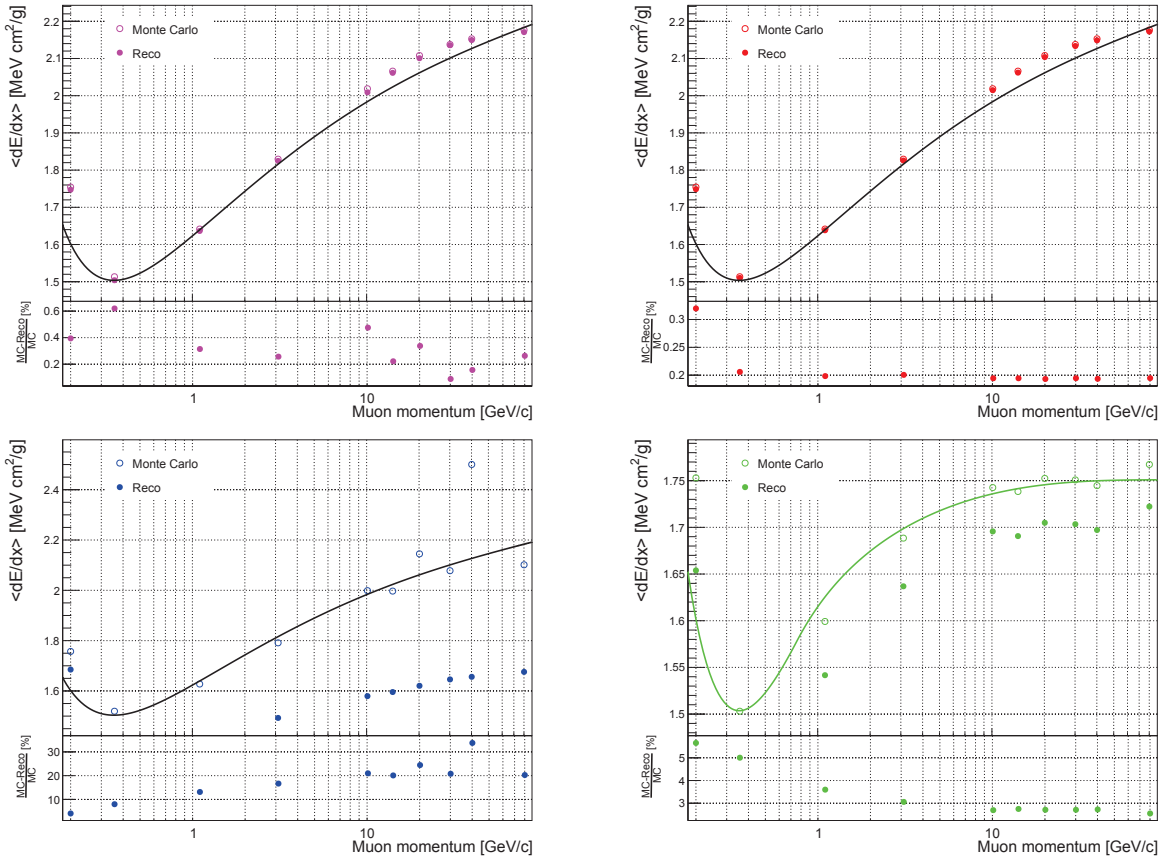

Figure 4.15: Monte Carlo $\langle \mathrm{d}E/\,\mathrm{d}x \rangle$ (empty dots) reconstructed $\mathrm{d}E/\,\mathrm{d}x$ (full dots) for the 4 different scenarios: simplest case (top left), noise case (top right), fluctuations case (bottom left) and δ-rays case (bottom right). All these measurements are corrected to eliminate the recombination effect.

readout response allows to reconstruct the deposited energy after the recombination effects related to quenching.

The reconstructed energy directly compared to the deposited energy after quenching differs from the Monte Carlo truth by values between 0.03% and 0.3%. Reconstructed energies are always smaller than those simulated. The reconstruction algorithm and unfolding of the readout response introduce a small systematic effect related to the way charge is quantized and samples assigned to the hits.

A calculation of reconstructed energy by taking into account an empirical correction for the quenching effects has been performed as well. The difference between the Monte Carlo deposited energy and the reconstructed energy by also including the quenching unfolding is significantly worse (a systematic bias of 3.5% for the most realistic case) than the one obtained only considering reconstruction effects. The reason is due to the fact that the empirical unfolding of the quenching factor $\mathcal{R}_{reco}$: at the level of the reconstructed hits

can be estimated only from the total charge seen by a strip after quenching and cannot account for microscopic effects corresponding to more localized charge depositions within the strip which at the generation level produce stronger recombination effects.

This study sets an upper limit to the accuracy of the energy reconstruction performance and shows the necessity to take into account some related systematic effects.

Chapter 5

Kaons and pions separation using energy losses

A giant Liquid Argon TPC (LAr TCP) is an ideal environment to search for proton decay, in particular in some exclusive decay channels such as the $p^+ \rightarrow K^+\overline{\nu}$ decay, given the large active mass and the particle identification and energy reconstruction capabilities of the detector. The signature of the final state is difficult to be missed or to be confused with other event topologies. It starts with an isolated positive kaon, produced somewhere within the detector fiducial volume, then stopping and generating its decay chain, including first a positive muon and then a positron. For this application it is extremely important to study the particle identification and energy reconstruction capabilities of the detector and to develop an algorithm for kaon identification.

The background to this signature can come from neutral current interactions of atmospheric neutrinos producing single charged particles in the final state or from interactions of cosmic ray muons in the rock surrounding the underground LAr TPC detector then projecting neutral kaons inside the detector which may produce secondary charged kaons [83]. This cosmogenic background source can be limited by defining a fiducial volume of the liquid argon with a large enough external buffer to absorb the neutral kaons. Neutral current interactions of atmospheric neutrinos are a kind of irreducible background, independent on the fiducial volume definition. The background discrimination down to negligible levels relies on isolation and energy cuts on the final state from the neutrino interaction selected by requiring the presence of a single kaon track candidate. This performance relies on assuming about 99% kaon identification efficiency with 1% level pions mis-identification [84, 85]. It is very important to study in details this performance for particle identification with detectors like WA105 by developing particle identification algorithms which can be then directly tested with test-beam particles. The goal of this Chapter is indeed to prepare a detailed study of such a particle identification algorithm which could be validated with the experimental data of WA105.

Since the LAr TPC can provide a detailed measurement of the ionization losses, it is possible to exploit this measurement for particle identification by focusing on what happens in proximity of the stopping point of the particle to be identified, where the separation

power is maximal. Kaons can be then distinguished from other particles, in particular pions which are the closest ones in mass and the most difficult ones to be disentangled, having also a similar decay topology. For this particle identification analysis it is then needed to compare the energy losses measured nearby the stopping point of the candidate track to end-of-range parametrizations of the energy losses, computed for different particle hypothesis.

An example is show in Figure 5.1, where it is possible to see the $\mathrm{d}E/\,\mathrm{d}x$ as a function of the distance from the stopping point (which corresponds to the origin of the horizontal axis). The blue line represents a parametric function for kaons average energy losses in proximity of the stopping point, the red line is the equivalent function for pions. The dots are the measured energy losses sampled at the level of reconstructed hits for two single candidate tracks (blue: a kaon, red: a pion). By comparing the measurements to the parametrizations for each hit of the candidate track a χ^2 with respect to the kaon (or pion) hypothesis can be computed. Using this information it is then possible to identify the track as produced by a kaon or by a pion.

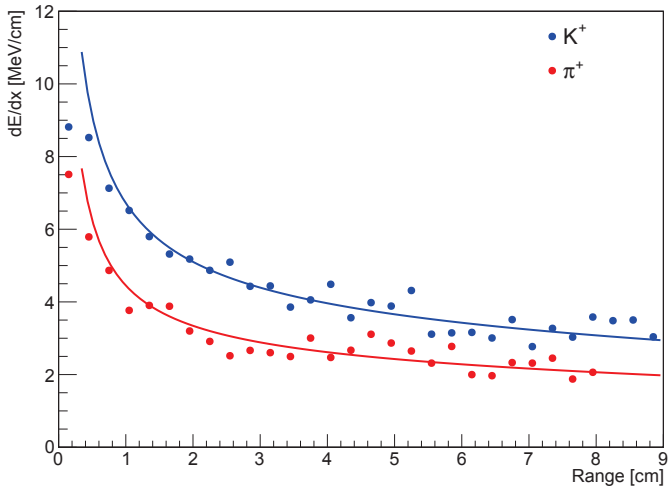

Figure 5.1: Examples of $\mathrm{d}E/\,\mathrm{d}x$ measurements in one view as a function of the distance from the stopping point for a kaon (blue dots) and for a pion (red dots); the red and blue continuous curves represent the average losses computed for the two particle hypotheses. The particles are simulated with an angle of 45° with respect to the view orientation.

This Chapter describes the analysis performed in order to obtain a parametrization of the $\mathrm{d}E/\,\mathrm{d}x$ profile in proximity of the stopping point for pions and kaons and the definition of a particle identification algorithm based on of the comparison of this parametrization with the measured energy losses.

First a short introduction about proton decay modes is given. Then a description of the definition and generation of the Monte Carlo samples used in order to obtain the average

$\mathrm{d}E/\,\mathrm{d}x$ parametrization is provided. The reconstruction technique in order to compare the measured samples to the parametrization is then described. Finally the analysis procedure for particle identification is shown and applied to kaon and pion samples in order to quantify the rejection power. Particle identification techniques, applied to the different particles in the proton decay chain and combined with the measurement of their energies allow for the definition of a very clear decay signature.

5.1 Proton decay

Grand Unified Theories (GUTs) unify the three gauge interactions of particle physics into one single force and, as a consequence, make predictions about baryon number violation and proton lifetime. In the literature proton decay has been studied by several authors [86, 87, 88]. Experimentally The limit on proton lifetime is set by results from Super-Kamiokande [89].

A proton decay mode which can be detected better by DUNE with respect to water Cerenkov detectors is $p^+ \rightarrow K^+\overline{\nu}$ since a LAr TPC can provide the complete signature via the identification of the kaon in the final state and of the products of its decay chain. Since stopping kaons have a higher ionization density than lower-mass particles, a liquid argon TPC could identify the K^+ track with high efficiency.

The signature for this decay is the presence of an isolated charged kaon (which would be monochromatic, with $p = 340$ MeV/c, neglecting the decaying proton Fermi motion in the argon nucleus). The kaon emerges intact from the nuclear environment containing the decaying proton because its momentum is below threshold for inelastic reactions.

In the LAr TPC the kaon can be tracked and identified via the detailed analysis of its energy loss profile. Since the most probable kaon decay mode is $K^+ \rightarrow \mu^+\nu_\mu$, all the charged daughter particles in the decay chain can be reconstructed and identified in liquid argon.

Figure 5.2 shows a sample event in the ICARUS T600 detector in which a kaon, produced in a neutrino interaction, is observed as a progressively heavy ionizing track that crosses the active volume, stops and decays to $\mu^+\nu_\mu$, producing a muon track that also stops and decays in $e^+\nu_e\overline{\nu}_\mu$.

5.2 Definition and generation of the Monte Carlo samples

The kaons generated for this work in the `GEANT` simulation have an initial momentum of $p_{K^+} = 340$ MeV/c, since this is the momentum given by the proton decay process in the proton rest frame. For a kaon, this momentum value corresponds to $\beta\gamma \simeq 0.69$. The smearing due to Fermi momentum is neglected in a first instance.

Using the *Particle Data Group* information on ranges normalized to the medium density and particles masses [44] and assuming (in first approximation) that the energy losses in

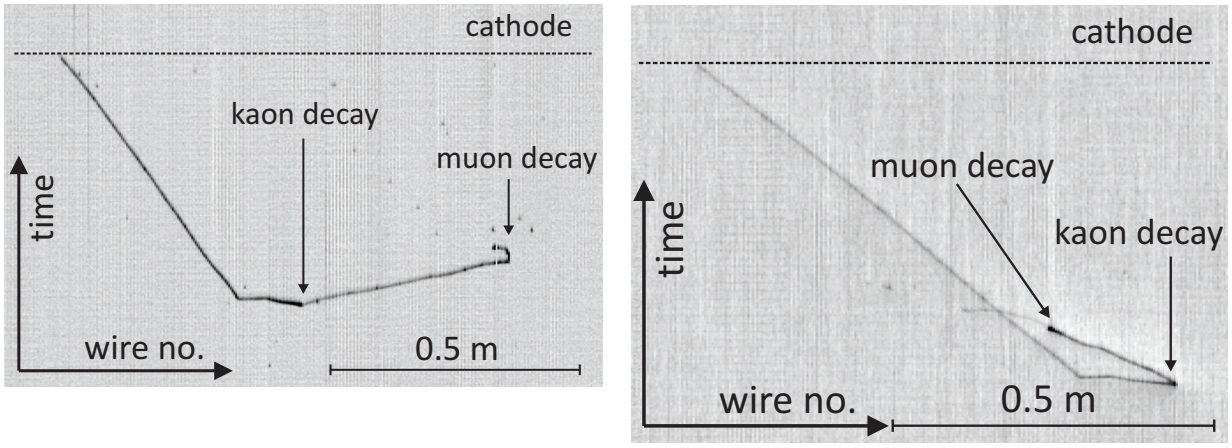

Figure 5.2: Event display for a decaying kaon candidate $K \to \mu\nu_\mu$ $\mu \to e\nu_e\nu_\mu$ in the ICARUS T600 detector. On the left it is shown the collection plane and on the right the induction plane [90].

liquid argon are similar to the ones in carbon (see Figure 5.3 left), it is possible to evaluate the range R travelled by the kaons in the liquid argon before stopping. This distance will represent the average exploitable lever arm for the energy losses measurements.

$$R/M \simeq 40 \text{ g cm}^{-2} \text{ GeV} \tag{5.1}$$

namely:

$$R_{K^+} \simeq 14 \text{ cm} \tag{5.2}$$

For what concerns the pions generation, a constraint on a range similar to the one travelled by the kaons is imposed in order to perform the analysis on an equivalent track length from the stopping point. By looking at Figure 5.3 right, it appears then necessary to generate these particles with a $\beta\gamma = 1$. This corresponds to a momentum $p_{\pi^+} = 140$ MeV/c.

Since for kaon $c\tau = 3.712$ m and for pion $c\tau = 7.804$ m, the average distance travelled by these particles with the momenta stated above is 4.504 m in the case of kaons and 11.053 m for the pions. This shows that most of these particles do not decay over the 14 cm before the stopping point. Similarly the number of hadrons having strong interactions with the production of secondaries over this distance has been evaluated with the `GEANT` simulation. As it will be shown later the requirement for the analysis is to sample the energy losses along the track for a distance of 10.6 cm in space (7.5 cm in one of the two views). In the `GEANT` simulation the number of kaons stopping at shorter distances than 10.6 cm is about 5%. These tracks will not be exploitable for the $\mathrm{d}E/\mathrm{d}x$ analysis and the decay search signature.

In order to study the simplest configuration 1000 K^+ events and 1000 π^+ events are generated with the particles momenta parallel to the anode plane, with a planar angle of 45° with respect to the strip orientation, in order to be symmetric with respect to the

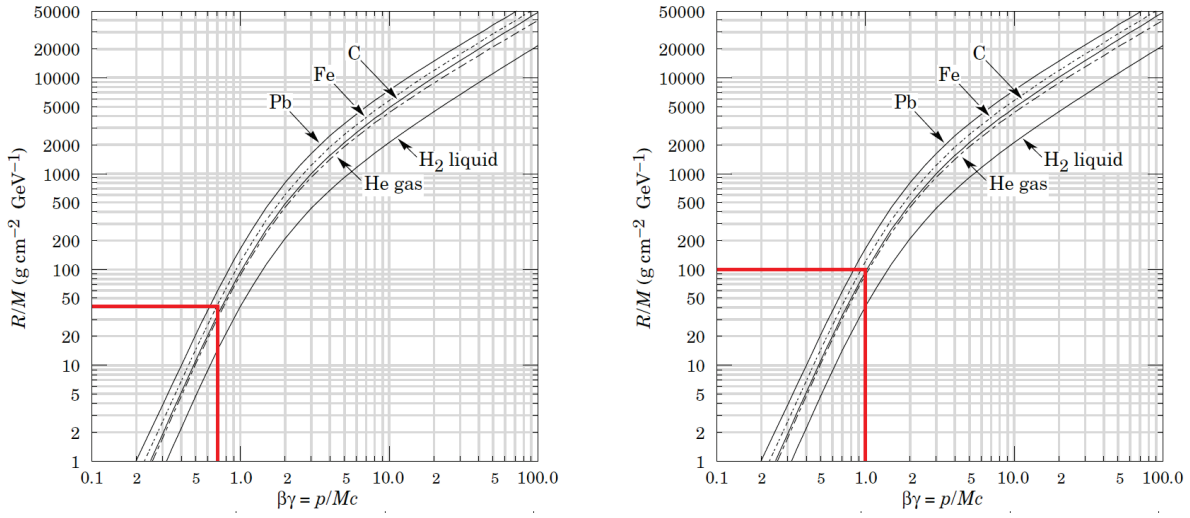

Figure 5.3: Range of charged particles: the $\beta\gamma$ value for a K^+ with $p_K = 340$ MeV/c (left) and for a π^+ with $p_K = 140$ MeV/c and the R/M corresponding value (red lines).

two readout views. This corresponds to the worst case when both views have the minimal sampling and are equivalent. For angles different than 45° one of the two views will have a better sampling than the one used in the analysis developed in this Chapter. The readout strips have a pitch of 3 mm. Finally the generation point is chosen to ensure that the entire distance travelled by the particles is inside the simulated active volume (active volume $d_{active\ vol} = 27.15$ cm): due to the incoming angle, considering the ranges calculated above, the track length expected on each view is $\lesssim 10$ cm. This allows having a full knowledge about the particle energy losses at the reconstruction level. The generation is performed under different signal/noise conditions peculiar of single-phase and dual-phase setups, in order to understand the impact of the non-negligible noise present in a single-phase LAr TPC. For practical reasons all the plots presented in this Chapter have for horizontal axis the distance measured along one view. The corresponding track distance in space is larger by a factor $\sqrt{2}$.

A single-phase TPC, in addition to a worse S/N ratio, would have also a coarser sampling pitch. For instance the single-phase TPC design considered in DUNE has a readout pitch of 5 mm. This introduces a larger uncertainty on the stopping point and a less precise measurement of the energy losses.

In a first approximation, in order to study at the basic level the energy losses in the liquid argon for the calculation of their parametrization to be exploited in the particle identification analysis, the δ-rays production has been deactivated in the simulation. Energy fluctuations have been then generated using the Landau-Vavilov-Gauss distribution implemented in `GEANT4`.

The δ-rays production implies the generation of additional track segments of knocked electrons and the deposition of additional ionization. This could make more difficult the

reconstruction process, introducing errors related to the hits or to the track reconstruction algorithms. These reconstruction effects are neglected on a first instance in order to understand the basic performance of the energy losses measurement technique independently on the quality of the tracking.

The simulation is performed with unitary gain and readout pitch of 3 mm. When noise is applied this corresponds to a single-phase detector $S/N \simeq 10$ similar to ICARUS. When the noise is switched off the simulation becomes close to a dual-phase LAr TPC where noise represents 1% of the signal for a particle at the ionization minimum and can be safely neglected in this analysis. In order to understand the impact of the noise, the noise simulation has also been deactivated in a first instance and then activated in a second phase.

Then the δ-rays production have been as well activated and the analysis has been repeated for these additional two configurations in order to check the differences with respect to the basic case without noise and δ-rays.

Three simulation configurations have been then systematically studied:

- fluctuations without noise and δ-rays production;
- fluctuations with noise (no δ-rays production);
- δ-rays production with noise (realistic case).

The kaon decay topology, once the kaon is at rest at the end of its range, can sometimes create problems in the hits reconstruction due to potential overlaps of the daughter muon track with the mother K^+ or π^+ track, as shown in Figure 5.4.

If the daughter muon goes in the backward direction, overlaps with the parent track will become probable. In this case the reconstruction program has to disentangle the contributions to the measured energy deposition from the two tracks, in particular near the stopping point where the two tracks may be superimposed within the detector pitch. This effect is an additional complication that needs to be properly addressed at the level of tracks reconstruction for the candidate proton decay events.

The daughter muon is clearly distinguishable from the mother particle by looking at the sharp discontinuity in the ionization profile as shown in Figure 5.5. The daughter muon, compared to the stopping mother particle, deposits at its starting point a small fraction of the end-of-range ionization of the mother particle. In case of overlaps the contribution from the muon can be extrapolated back and subtracted from the deposition related to the stopping track of its mother particle.

In this work the kaon decay has been deactivated at the level of Monte Carlo production in order to obtain a correct parametrization of the energy losses nearby the stopping point as a function of the distance, which is the goal of this Chapter. This parametrization can then be used in a more general context to treat as well the overlap cases identified at the tracks reconstruction level after disentangling and subtraction of the daughter muon.

A finer readout pitch (3 mm strips for a dual-phase detector vs 5 mm wires pitch for a single-phase detector as studied in DUNE) is beneficial under several aspects:

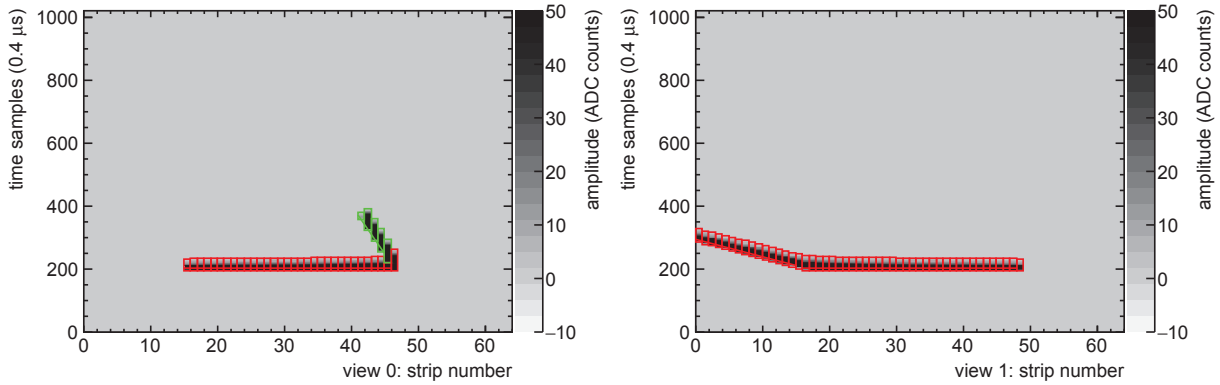

Figure 5.4: Event display for a kaon decay, in view 0 the daughter muon track in green is overlapped within the sample corresponding to the stopping to the mother track.

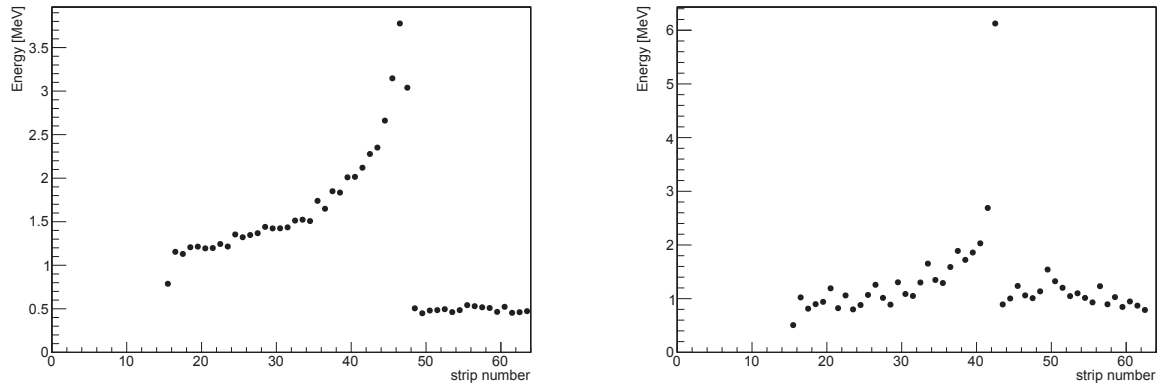

Figure 5.5: Energy deposition in view 0 for a kaon decay (left) for a pion decay (right). It is possible to appreciate the strong discontinuity among the energy loss of the mother particle at the stopping point and the one of the daughter muon.

- it helps in better resolving the overlaps among the mother and daughter particle in the kaon decay;
- it reduces the uncertainty on the position of the stopping point of the mother particle and hence on the amount of energy deposited in the last ionization sample. This aspect will be treated in details in the next section;
- It increases the number of exploitable ionization samples and the separation power in the particle identification fit.

The Monte Carlo generator produces the energy depositions by transporting particles in the detection medium via several identical steps, as described in Chapter 4. Some particular care has to be applied in setting the GEANT steps in the simulations employed for this particle identification analysis. The default step size used in Qscan for the simulation was 0.05 cm. Since the detector pitch size is 0.3 cm, an incoming particle with an angle of 45° will travel a distance $d \simeq 0.424$ cm across each strip. The ratio between the distance travelled within a strip and the step size used by GEANT4 is

$$\text{Ratio} = 8.48 \tag{5.3}$$

This means that the strips are systematically covered by 8 or 9 steps in an alternated series. The consequence is that the strips containing 8 steps would have a simulated smaller energy deposition with respect to the strips with 9 steps. This beat effect generates a discontinuous structure, as shown in Figure 5.6 left. This beat effect still persists even when the step size is reduced to 0.01 (Figure 5.6 right). By setting the step size to 0.001 cm the beat effect eventually vanishes (see Figure 5.7). This is the setting finally used for this analysis.

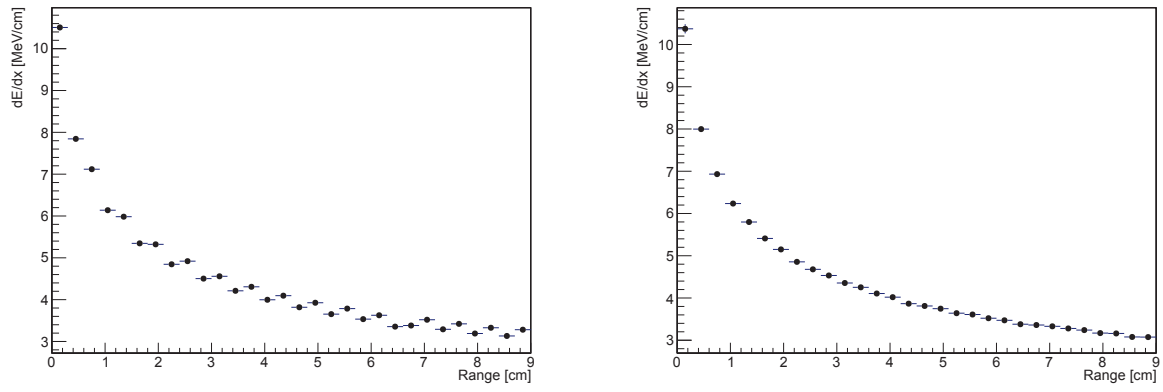

Figure 5.6: $\langle \mathrm{d}E/\,\mathrm{d}x \rangle$ as a function of the range for 1000 kaons. The events have been generated using a GEANT step size of 0.05 cm (left) or 0.01 cm (right).

As described in Chapter 4 the electrons-ions recombination factor $\mathcal{R}$ at the Monte Carlo level is evaluated for each step by using the energy deposited in that particular step. As a consequence of that, the step size is very important: the $\mathcal{R}$ calculation becomes more and more precise when adopting smaller steps.

During the reconstruction process for particle identification a possible approach could consist in correcting the measured energy for the quenching effect in order to compare to the theoretical $\mathrm{d}E/\,\mathrm{d}x$ values for different particle hypothesis.

This process is however complicated since, as seen also in the Chapter 4 dealing with the energy losses reconstruction, microscopic effects with different quenching factors are summed up at the level of the total charge seen by a single strip.

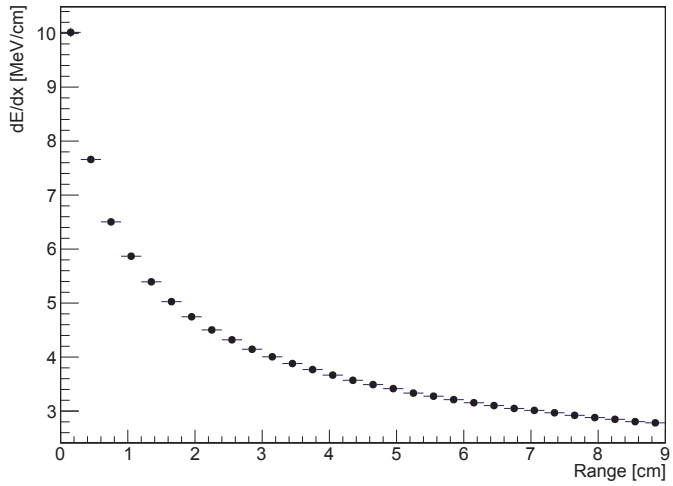

Figure 5.7: $\langle \mathrm{d}E/\,\mathrm{d}x \rangle$ as a function of the range for 1000 kaons using the step size 0.001 cm.

By not knowing individually these microscopic contributions, the only possible correction for quenching effects at the level of the total charge seen by a strip would be based on taking into account an average empirical recombination factor.

This average factor ($\langle \mathcal{R}_{reco} \rangle$) can be only computed on the basis of the average energy loss seen by the strip after recombination. The energy loss is obtained by dividing the total energy collected in the strip by the effective strip pitch seen by particle ($pitch * \sin(\vartheta)$), as explained in Chapter 4.

However this unfolding procedure, as seen in Chapter 4, is not very accurate and for this reason it is deliberately not applied in the particle identification procedure worked out in this Chapter.

This approach avoids mixing up the systematics due to the correction of the quenching effects with the parametrization of the energy losses. The quenching effects are correctly simulated at the single steps level. Then the parametrization of the energy losses and the experimental measurements on single tracks are directly expressed, and compared to each other for the particles ID calculations, only in terms of quenched $\mathrm{d}E/\,\mathrm{d}x$.

There is therefore no attempt of unfolding in order to express the parametrization and the tracks measurements in terms of real $\mathrm{d}E/\,\mathrm{d}x$ corrected by the quenching. This choice of using the quenched energy in the analysis has to be kept in mind when comparing results to the absolute $\mathrm{d}E/\,\mathrm{d}x$ scale. The $\mathrm{d}E/\,\mathrm{d}x$ values in plots shown in this Chapter are smaller than what one would expect by taking into account the Bethe-Bloch because they include also recombination effects.

5.3 Energy loss parametrization and particles ID analysis

In the calculation of the average $\mathrm{d}E/\mathrm{d}x$ parametrization, the only information used is at level of the hits reconstruction, in order to avoid possible errors related to the clustering or tracking algorithms.

The events taken into account for this analysis are those that have a minimal number of consecutive strips which collect a signal, *i.e.* each event needs to have a minimal track length (computed as the difference between the first and the last strip collecting the signal). This requirement avoids taking into account the events where the particle decays in flight or interacts with the liquid argon.

The length requirement used in this analysis is $l_{view} \geq 7.5$ cm from the stopping point. This minimal track length corresponds to an optimal distance with respect to the stopping point in order to obtain the maximal discrimination power from the energy losses profile which shows little difference among the two particle hypothesis for greater distances from the stopping point. The fraction of events non satisfying the length criterion described above at the reconstruction level is $\approx 4\%$ for the kaon sample and $\approx 7\%$ for the pion sample, this is mainly an effect of hadronic interactions, as explained before. This length can be compared to the range of the kaon at 340 MeV/c which amounts to 10.6 cm in one view (14 cm in space) and it makes this particle identification criterion exactly applicable also to lower energy kaons (down to about 290 MeV/c) and as well to higher energy kaons resulting from the Fermi momentum smearing.

A crucial point for the calculation of the parametrization is to reconstruct the energy losses of the kaons and pions as a function of the distance from the stopping point (*range*). For this purpose it is very important to make sure to reconstruct correctly the stopping point from the pattern of deposited energy in the strips. The Monte Carlo stopping point is deliberately not used in order to take into account quantization effects related to the strips pitch which will be anyhow present in the real events. The strips pitch has an important role in the definition of the sampling of the $\mathrm{d}E/\mathrm{d}x$ curve. As mentioned before the finer pitch is a merit factor for dual-phase LAr TPC detectors.

The track starting point is defined as the first strip which contains a significant signal over threshold with respect to the particle direction.

The distance travelled by the particle is sampled in bins of 0.3 cm width (the readout pitch). The $\mathrm{d}E/\mathrm{d}x$ for each bin is evaluated as the total energy ΔE deposited in a selected strip divided by the distance Δx travelled in the strip ($\Delta x = 0.3\sqrt{2}$ cm $= 0.424$ cm, since the particle incoming angle in this simulation is 45°):

$$\left(\frac{\mathrm{d}E}{\mathrm{d}x}\right)_{bin} = \left(\frac{\Delta E}{\Delta x}\right) = \frac{\text{Energy deposited}}{0.424 \text{ cm}} \tag{5.4}$$

This $\mathrm{d}E/\mathrm{d}x$ is then corrected by the track angle. For the calculation of the parametrization the track angle is extracted from its absolute knowledge from the MC. In the particle ID

analysis presented in the following the same procedure will also be applied to the samples of the candidate tracks to be compared to the parametrization.

In the general case, when comparing to the parametrization track from real events, without having the knowledge of the incoming angle from the MC, it will be necessary to use the fitted track direction information in order to evaluate the travelled distance in the strips. An error on the track direction measurement could result in an overall systematic effect on the $\mathrm{d}E/\,\mathrm{d}x$ scale of the sampled track but not on the $\mathrm{d}E/\,\mathrm{d}x$ shape as a function of the distance from the stopping point. In a first approximation this secondary systematic effect on the performance of the particle ID algorithm is neglected. Similarly the effect of multiple scattering has been neglected as well in a first approximation.

Figure 5.8 shows the total Monte Carlo energy deposited in the active volume without multiple scattering (green area) and with multiple scattering (orange area) for 1000 kaons in the simplest case of Landau-Vavilov-Gauss fluctuations (left) and in the more complex case of δ-rays production (right). The mean energy depositions with multiple scattering switched-off or switched-on are very similar: the difference is about 0.3% in both cases of the simulations with fluctuations and δ-rays generation. Hence, neglecting multiple scattering is a reasonable choice.

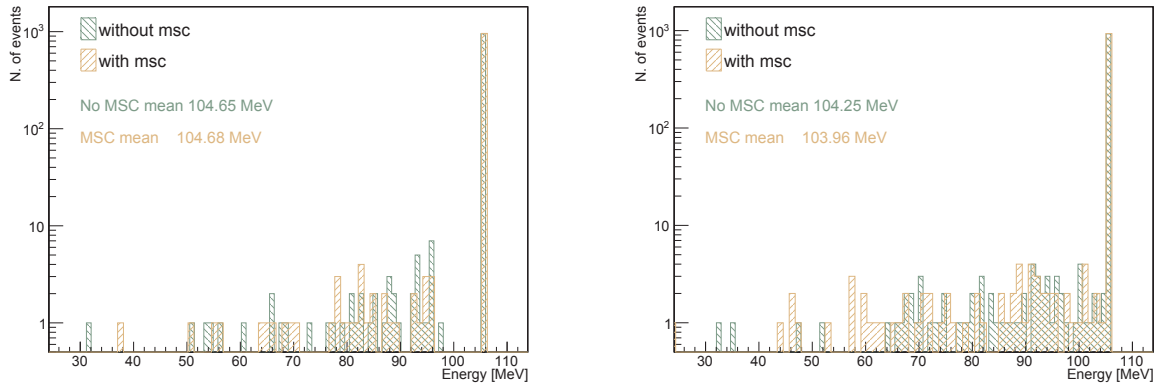

Figure 5.8: Monte Carlo energy deposition in active volume without multiple scattering (green area) and with multiple scattering (orange area) for 1000 kaons in the simplest case of Landau-Vavilov-Gauss fluctuations (left) and in the more complex case of added δ-rays production (right).

The $\mathrm{d}E/\,\mathrm{d}x$ bins corresponding to different samples of 0.3 cm can then be plotted as a function of the sample number starting from the sample identified as stopping sample of the track. For illustrative reasons all the plots are produced not by reporting on the x axis the sample number but by putting a distance, computed by multiplying the sample number by the pitch of 0.3 cm. In order to be completely rigorous and coherent with the simulation geometry this distance should have been corrected as well by the track angle, however this has no effects at all in the analysis discussed in this Chapter, which is de facto

only based coherently on the sample number.

Since the energy losses are relevant in proximity of the particle stopping point, it is very important how this point is defined and reconstructed. The particle stopping point can be known with an accuracy which depends on the strip pitch.

Figure 5.9 shows two examples in which the particle is stopping respectively at the beginning or at the end of the strip. The reconstructed particle stopping point will be the same. However there will be a difference between the left and the right cases in terms of the energy losses $\Delta E/\Delta x$ measured by this last strip which collects the ionization signal. If the distance travelled in the last strip is small (as shown in Figure 5.9 left), the quantity $\Delta E/\Delta x$ is smaller than the $\Delta E/\Delta x$ in the case where the particle crosses a greater distance in the strip (Figure 5.9 right). This means that, when taking into account the average $\langle \mathrm{d}E/\,\mathrm{d}x \rangle$ over many events, the bin corresponding to the last strip will be affected by large fluctuations related to the real stopping position of the particle within the strip width.

The large increase of the energy losses nearby the stopping point implies that in the particle identification analysis the definition of the first bin of the distribution plays an important role. Primarily it is important that the reconstructed last strip of the track should contain the real position of the stopping point. Furthermore the strip width and the consequent indetermination of the stopping point position within this width introduces fluctuations on the energy loss measurement in this last strip.

In the following several methods will be investigated for what concerns the choice of the last strip in order to achieve the best performance in terms of particle identification analysis.

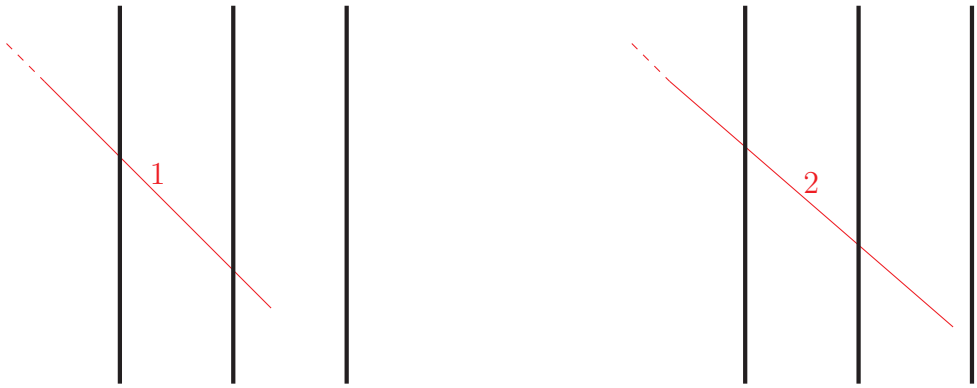

Figure 5.9: Schematic view of charge deposition (red line) with respect to the strips size. Left: the particle stops at the beginning of the last strip. Right: the particle stops almost at the end of the last strip.

Two possible solutions for the selection of the last strip (which should be representative of the stopping point) have been studied:

Case 1: the last strip is defined as the one which contains the highest energy deposition.

Following this definition the first bin could correspond to the last strip which collects the signal, or to the last-but-one. If the particle travels a big distance in the last strip before stopping, the energy deposition per cm will be the largest of the track; otherwise if the particle stops at the beginning of the strip, the largest energy deposition will be typically in the last-but-one strip which records a signal, as it will be shown later in Figure 5.11. Using this definition the are no large energy fluctuations in the first chosen bin and the energy losses are a monotonic function of the range, as shown in Figure 5.10 left.

Case 2: the last strip is defined as the last one which collects a significant signal above noise. In this case the first bin in the histogram always corresponds to the last strip. According to this definition however the energy deposited in the first bin of the histogram may change for each event, depending on the real stopping point of the particle within the strip. Figure 5.10 right shows the average energy losses per cm as a function of the range using this definition: it is possible to note the smaller value for the deposition in the first bin, due to the fluctuations on the position of the stopping point within the strip.

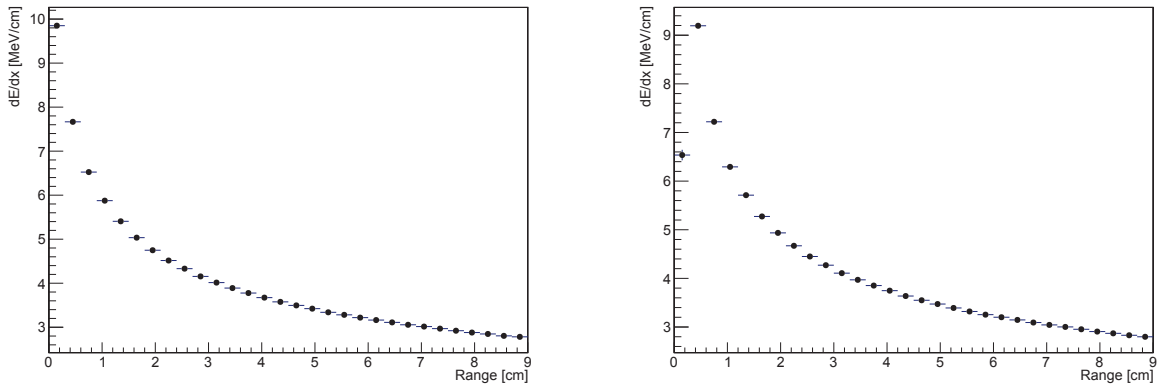

Figure 5.10: $\langle \mathrm{d}E/\,\mathrm{d}x \rangle$ as a function of the range for 1000 kaons in two different cases: the first bin is defined as the strip with the highest energy deposition (left) and the first bin is defined as the last strip collecting a significant signal.

It is interesting to look at the energy distribution for the last and the last-but-one strips for the two possible cases of last strip choice for kaon decays. In **Case 1** the energy distribution in the strip upstream the highest energy strip is very regular and it has a direct correlation with the position of the stopping point in the downstream strips (Figure 5.11 top and bottom right).

The energy distribution in the last strip (Figure 5.11 top left) is not symmetric and it is not possible to parametrize it with a Landau distribution. This can be understood by looking at Figure 5.11 bottom left: here it is possible to see the relation between the energy

deposited (x axis) and the difference between the Monte Carlo stopping point coordinate and the coordinate of the strip with the highest energy deposition (y axis).

From these distributions it is possible to see that if a particle deposits a small quantity of energy in the reconstructed last strip there are two cases represented by two different branches in the plot. The low deposited energy may correspond to particles stopping in the downstream strip. So the reconstructed last strip is in reality the last-but-one strip from the stopping point. The fact that the highest energy strip was reconstructed as last strip is due to the shortage of the particle path in the downstream strip.

As shown by the second branch, it may also happen that the particle deposits a small quantity of energy in the last reconstructed strip because it deposited a lot of energy in the last-but-one strip (Figure 5.11 bottom left). This is due to path fluctuations related to the to the energy fluctuations. Otherwise if the particle deposits a lot of energy in the highest energy strip, this indeed corresponds to the stopping point.

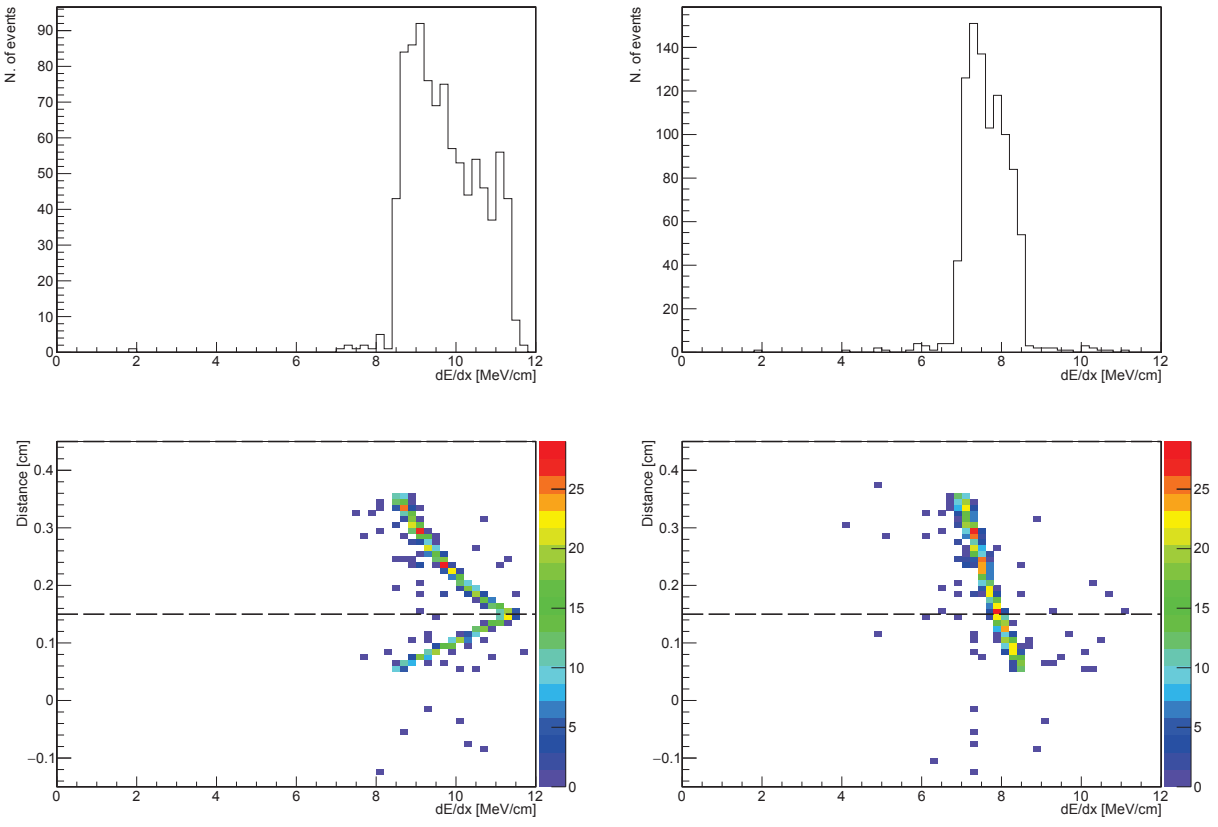

Figure 5.11: Top: energy distribution in the last strip (left) and in the last-but-one strip (right). Bottom: difference between the Monte Carlo and recorded stopped point as a function of the energy deposition in the last strip (left) and in the last-but-one strip (right). The definition of *last* and *last-but-one* strip corresponds to the definition given in **Case 1**.

In **Case 2** the energy distribution in the upstream strip is regular and it has a direct correlation with the position of the stopping point (see Figure 5.12 top and bottom right), as in **Case 1**. The difference with respect to **Case 1** is the larger quantity of energy deposited in this strip: this is due to the fact that in **Case 2** it is always the last-but-one strip (*i.e.* the last strip crossed before particle stops). In **Case 1**, on the contrary, could be the last-but-one or the third to last before the particle stops: it means that the energy deposition could be smaller.

Looking at the energy deposition in the last strip (Figure 5.12 top and bottom left) it is possible to note that a greater energy deposition in the last strip corresponds to an higher distance travelled in the last strip, as expected.

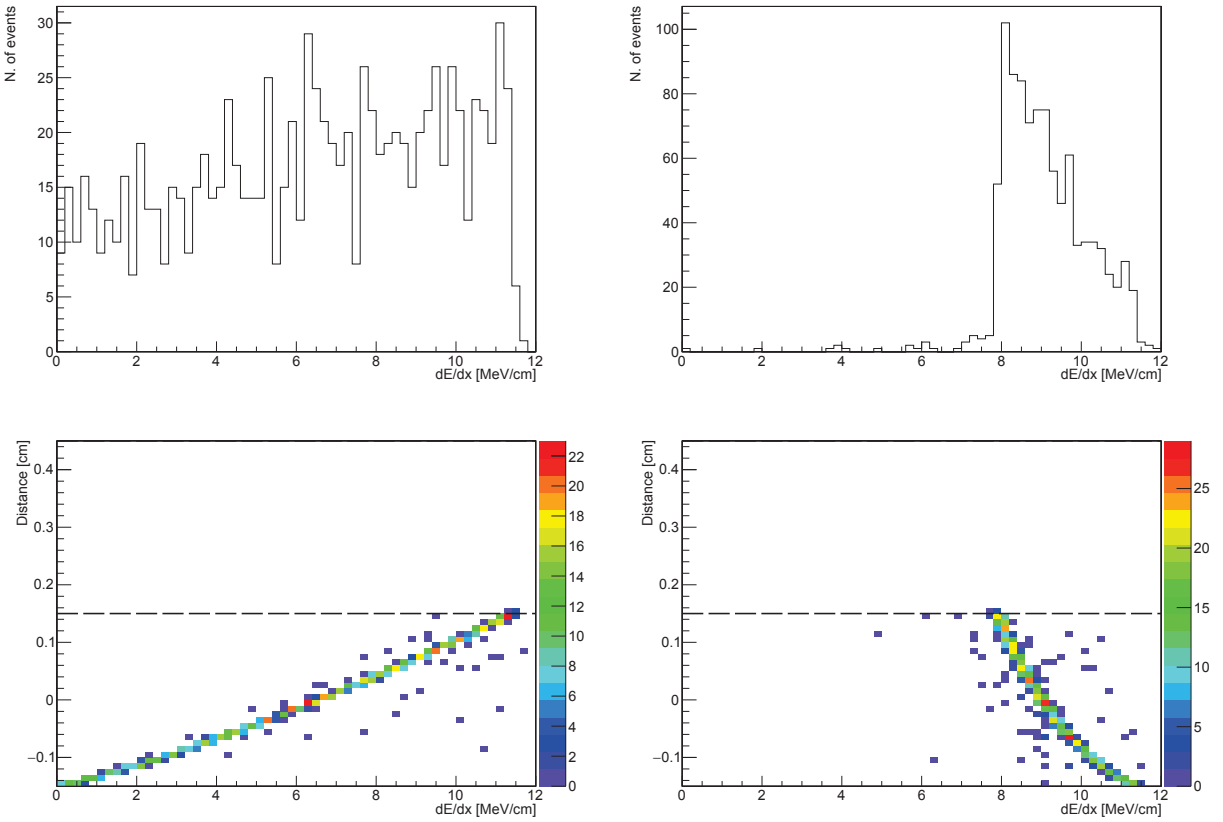

Figure 5.12: Top: energy distribution in the last strip (left) and in the last-but-one strip (right). Bottom: difference between the Monte Carlo and recorded stopped point as a function of the energy deposition in the last strip (left) and in the last-but-one strip (right). The definition of *last* and *last-but-one* bin corresponds to the definition given in **Case 2**.

Following the definition given in **Case 1** the $\langle \mathrm{d}E/\,\mathrm{d}x \rangle$ distribution is a monotonic function for all the range. This definition generates a very complicated picture and the first bin includes different physical situations: it includes the energy deposited at the end

of the track for the high energy particles and the energy deposited for the passing through particles.

The definition given in **Case 2** does not present the problems described above. The first bin contains only the last part of the track and the last-but-one bin corresponds to the last strip which has been completely crossed by the particle. For these reasons in this work the first bin of the energy losses distribution close to the track stopping point is finally defined as the last strip of the track which contains a signal.

In a more general simulation context the presence of the daughter muon, which is not present at this level of the simulation, will not perturb significantly the situation corresponding to these two selection criteria since the ionization profile of the daughter muons is very different (at much lower values) than the one of the stopping particle so that the daughter particle hits can be easily identified and removed from the analysis. Similarly there will be a small contribution from the daughter muon to the strip where the mother particle stops. This contribution compared to the ionization of the stopping particle will be much smaller and represents a second order effect with respect to the variability of the stopping point of the mother particle within the strip.

5.4 Development of the kaon identification algorithm

Once that energy losses sampling is defined, the next step of this work is to find a function to parametrize the mean energy losses distribution as a function of the distance from the stopping point.

In a first instance the analysis has been performed by using the Monte Carlo generation without the noise simulation neither δ-rays production (as discussed above). In a second phase the noise simulation has been introduced and finally the δ-rays production has been activated in order to analyse the consequences of these effects.

5.4.1 Simulation including only fluctuations

Figure 5.13 shows the reconstructed energy losses distribution as a function of the range for the kaons (left) and for the pions (right) in the view 0.

The parametrization of the energy losses for kaons and pions has been performed by fitting the energy losses distributions with different functional models in order to find the curve better describing the distributions.

The fit region starts at $range = 0.45$ cm and stops at $range = 7.2$ cm. The requirement on the starting point is due to the choice of the first bin (as explained before) ensuring a behavior independent on the fluctuations happening in the first chosen bin. The upper limit of the fit region is related to the request of minimal length for each tracks (see Section 5.3).

As a first attempt, an exponential function has been used to parametrize the distribution, but it was found that it does not fit in a reasonable way the points coming from the simulation results. Then, a power law function has been used to fit the distributions:

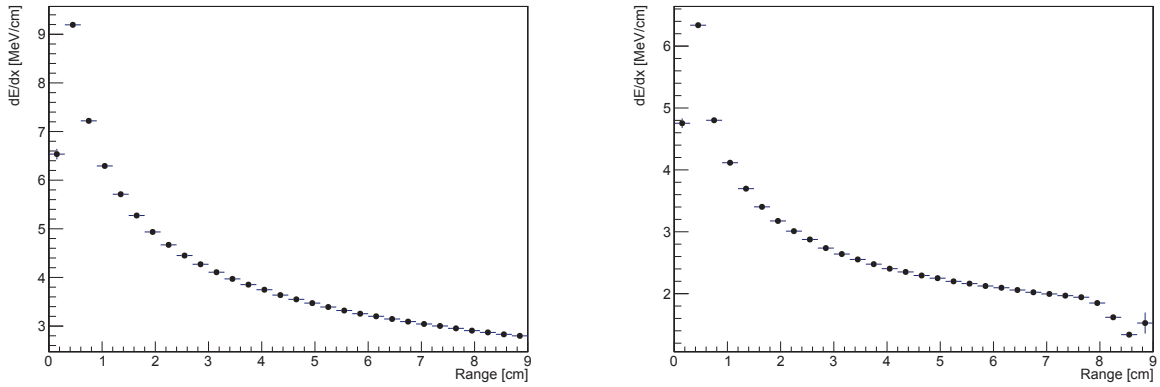

Figure 5.13: $\langle \mathrm{d}E/\,\mathrm{d}x \rangle$ as a function of the range for 1000 kaons (left) and 1000 pions (right) in the view 0.

as shown in Figure 5.14 (blue curve), this function underestimates energy losses for low values of range. Finally a linear combination of power law function and exponential has been used to define the parametrization:

$$f(x) = Ax^B + C\,\mathrm{e}^{Dx} \tag{5.5}$$

Looking at the Figure 5.14 it is possible to note that the parametrization performed using Equation (5.5) (red dashed line) is very similar to the power law parametrization, with the only difference for low values of range: here Equation (5.5) interpolates better data. For this reason this last parametrization has been chosen for this analysis.

In Figure 5.15 are shown the kaons and pions energy losses distributions fitted using the power law function plus exponential (equation (5.5)). In Table 5.1 are reported the parameters values of the function.

	View 0	View 1
A	4.960	4.990
B	−0.530	−0.526
C	1.525	1.521
D	−0.025	−0.028

	View 0	View 1
A	2.805	2.790
B	−0.686	−0.680
C	−1.453	1.448
D	−0.020	−0.021

Table 5.1: Fit results for kaons (left) and pions (right) energy losses distributions.

In order to evaluate the uncertainty to be associated to the parametrization of the average energy losses one needs to take into account the dispersion of the measured energy

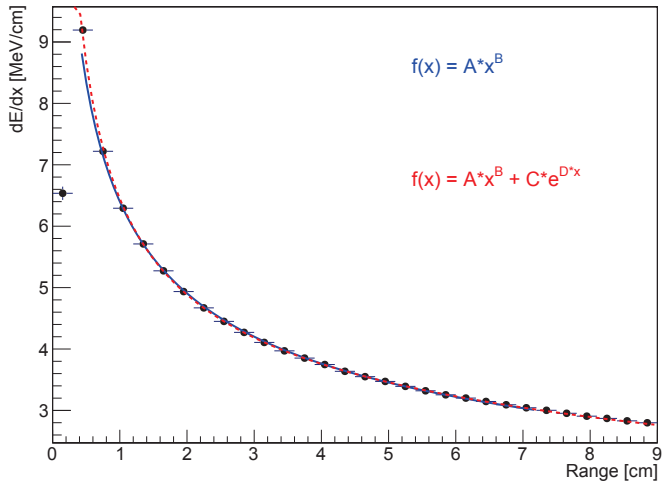

Figure 5.14: Difference between the parametrization using a power law and formula 5.5).

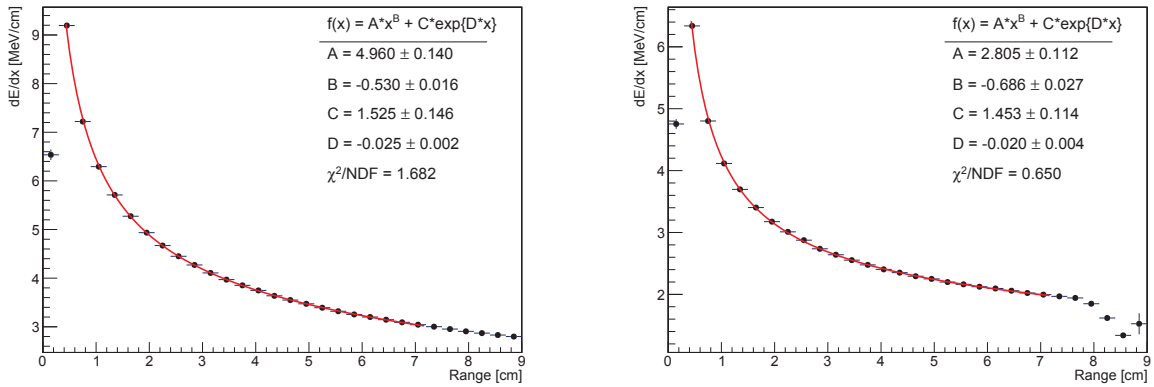

Figure 5.15: Kaon (left) and pion (right) energy losses distribution fitted with the power law function plus exponential (5.5) for view 0.

losses distribution for each distance bin. Each bin of the distribution (with the exception of the first bin, which is not used for the fit) has been fitted using a Gaussian function, as a good approximation of a Landau distribution for this particular sampling. The σ resulting from this Gaussian fits is used to define the uncertainty of the average losses distribution for each bin. In Figure 5.16 are shown the energy losses distribution and relative Gaussian parametrization for the second, third and fourth bin.

Particle identification is performed in the following way: a χ^2 is defined for the kaon and pion hypothesis using the information obtained from the parametrization and evaluated

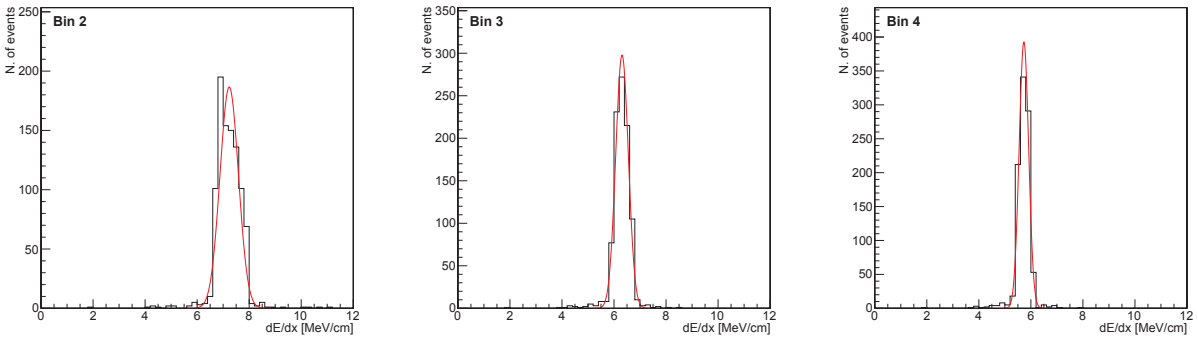

Figure 5.16: Energy losses distribution for three different distance bins. The distributions are fitted using a Gaussian distribution: the σ obtained from this interpolation is used to evaluate the uncertainty associated to the parametrization.

for each candidate track.

For the kaon hypothesis the χ^2 is defined in the following way:

$$\chi^2_K = \sum_j \frac{(y_j - \tilde{y}_{j,K})^2}{\sigma^2_{j,K}} \tag{5.6}$$

where the sum is performed over all the range bins, y_j represents the value of energy deposited in the j-th bin, $\tilde{y}_{j,K}$ is the value of parametric function obtained using equation (5.5) for the j-th bin and $\sigma_{j.K}$ is width of the Gaussian parametrization for the energy distribution in the j-th bin.

In the same way it is possible to define a χ^2 for the pion hypothesis:

$$\chi^2_\pi = \sum_j \frac{(y_j - \tilde{y}_{j,\pi})^2}{\sigma^2_{j,\pi}} \tag{5.7}$$

the π label means that these quantities are evaluated using the pions parametrization.

In Figure 5.17 left it is shown the χ^2 distribution in the kaon hypothesis for the view 0: the majority of the kaon events (blue area) lies in the region of low χ^2 value, as expected. On the other side, pion events (red area) have usually a big χ^2 value. It is possible to apply a cut on this variable in order to separate the kaons from the pions. The separation obtained using as discriminant value $\tilde{\chi}^2_K = 120$ (black dashed line in Figure 5.17 left) is shown in Table 5.2.

It is interesting to compare the χ^2 values with respect to the two hypothesis in order to look for a correlation between χ^2_K and χ^2_π, exploitable to reject a greater number of pions. Figure 5.17 right shows the correlation between χ^2_K and χ^2_π for each event: the two populations (kaons in blue and pions in red) are well separated. It is possible to look if a cut depending on the two χ^2 could give a better separation. Eventually in order to perform

this separation it has been defined a straight line cut with this parametrization:

$$\chi^2_\pi = 5\chi^2_K - 370 \tag{5.8}$$

The results of this new cut are reported in Table 5.3.

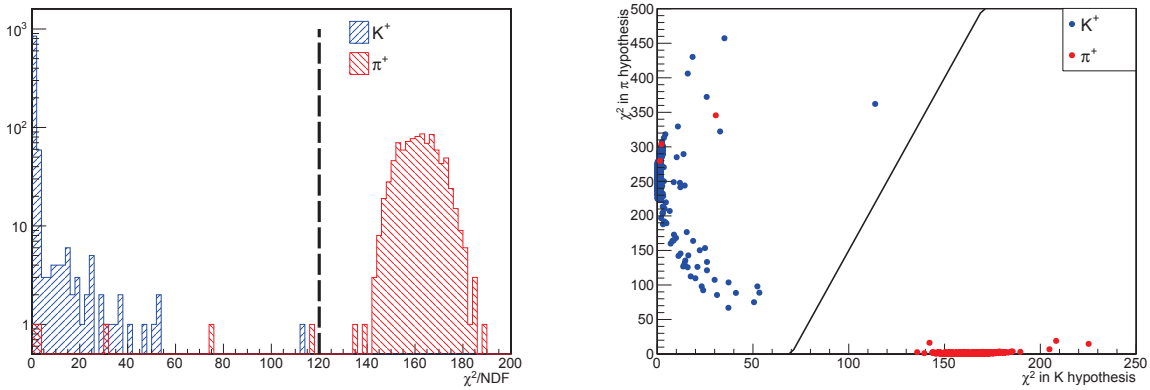

Figure 5.17: χ^2 distribution with respect to the kaon hypothesis (left) and event distribution as a function of χ^2_K and χ^2_π for kaons (blue) and pions (red) in view 0 in the case of only fluctuactions.

	View 0	View 1
Total K^+	958	959
Surviving K^+	957	958

	View 0	View 1
Total π^+	933	928
Surviving π^+	5	6

Table 5.2: Results of cut on χ^2_K distributions for kaons sample (left) and pions sample (right) in the case of only fluctuations.

This bi-dimensional cut based on the two χ^2 estimation does not increase significantly the results achieved with a single cut based on the χ^2_K. The reason of this fact lies in the fact that the two populations are originally well separated.

5.4.2 Simulation including fluctuations and noise

At this point it is interesting to repeat the analysis performed above by adding also the electronic noise simulation. Noise generation is made following the description in Chapter 4. The noise represents the 10% of the signal of a particle at the ionization minimum, as in the ICARUS LAr TPC.

	View 0	View 1
Total K^+	958	959
Surviving K^+	957	959

	View 0	View 1
Total π^+	933	928
Surviving π^+	6	6

Table 5.3: Results of linear cut (5.8) on χ^2_K distributions for kaons sample (left) and pions sample (right) in the case of only fluctuations.

Figure 5.18 shows the reconstructed energy losses distribution as a function of the range for the kaons (left) and the pions (right) in the view 0. Comparing these distributions with the distributions in Figure 5.13 it is possible to note that the case with and without noise are very similar: this happens because the noise represents about 10% of the signal, as explained before and it is at second order with respect to the ionization fluctuations.

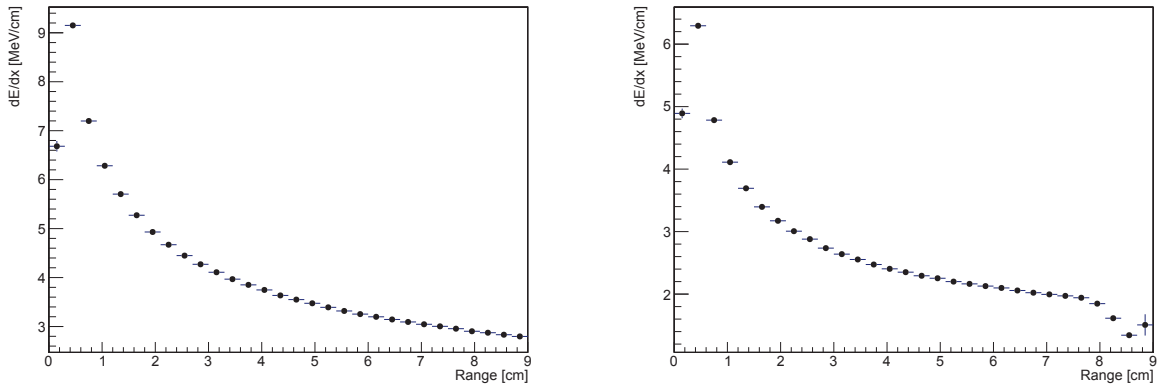

Figure 5.18: $\langle \mathrm{d}E/\,\mathrm{d}x \rangle$ as a function of the range for 1000 kaons (left) and for 1000 pions (right) for the view 0.

Figure 5.19 shows the results of the fit of the energy losses distribution for the kaons (left) and the pions (right) in view 0. In Table 5.4 are reported the fit results in the case of the kaons (left) and pions (right) generation with the noise simulation.

To confirm the similarity of the simulation with the noise generation with respect to the simplest case with only the energy loss fluctuations, in Figure 5.20 it is possible to see the comparison between the energy deposition in three different bins. The results of the fits in the two different case are very similar, as expected.

Finally, by repeating the analysis described for the case with only fluctuations, it is possible to analyse the χ^2 distribution for the kaon hypothesis (Figure 5.21 left). Setting a cut for the value $\tilde{\chi}^2_K = 90$ it is possible to separate the two populations, with the results reported in Table 5.5.

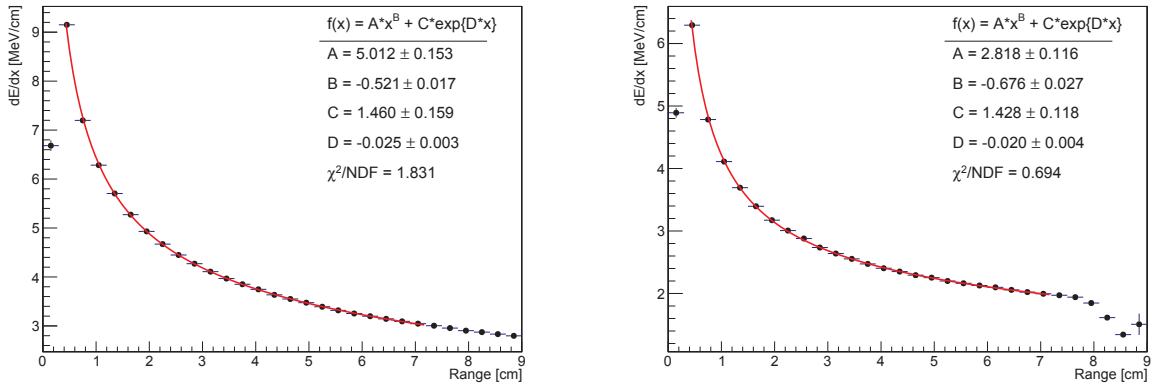

Figure 5.19: Kaon (left) and pion (right) energy losses distribution with noise fitted with the power law function plus exponential (5.5) for view 0.

	View 0	View 1
A	5.012	4.987
B	−0.521	−0.523
C	1.460	1.518
D	−0.025	−0.028

	View 0	View 1
A	2.818	2.798
B	−0.676	−0.672
C	1.428	1.433
D	−0.020	−0.021

Table 5.4: Fit results in the case with noise generation kaons (left) and pions (right) distribution (right).

As expected, the noise generation has not modified the kaons and pions distributions. The only effects is that the χ^2_π distribution assumes lower values with respect to the case without noise generation, as it is possible to see by looking at Figure 5.21 right.

Also with the noise generation the two populations are well separated and by applying a linear cut depending on the two χ^2, with the following parametrization:

$$\chi^2_\pi = 6.25\chi^2_K - 375 \tag{5.9}$$

it is possible to obtain the results shown in Table 5.6.

Also in this case the linear cut based on the two χ^2 estimation gives results very similar to those obtained with a single cut based on the χ^2_K.

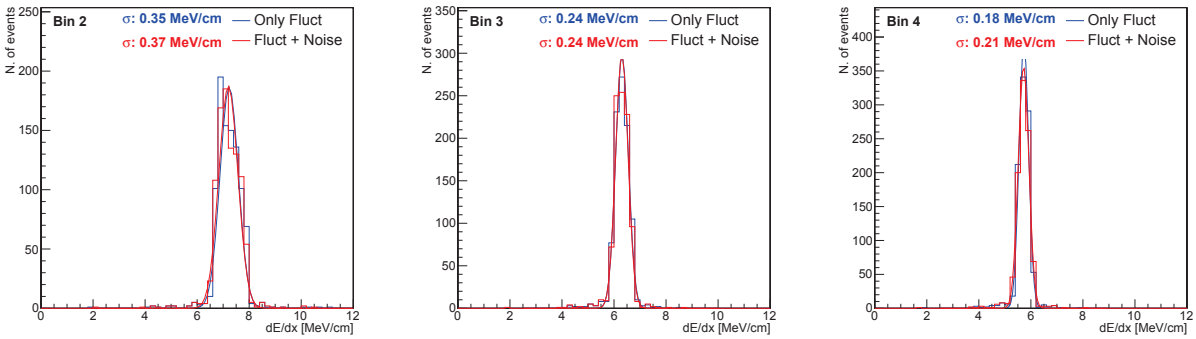

Figure 5.20: Comparison between the energy distribution for kaons in three different bins in the case of generation with fluctuations (blue lines) and the case of generation with fluctuations and noise (red lines).

	View 0	View 1
Total K^+	958	959
Surviving K^+	956	958

	View 0	View 1
Total π^+	933	928
Surviving π^+	5	6

Table 5.5: Results of cut on χ^2_K distributions for kaons sample (left) and pions sample (right) in the case of fluctuations and noise.

	View 0	View 1
Total K^+	958	959
Surviving K^+	957	958

	View 0	View 1
Total π^+	933	928
Surviving π^+	5	6

Table 5.6: Results of linear cut (5.9) on χ^2_K distributions for kaons sample (left) and pions sample (right) in the case of fluctuations and noise.

5.4.3 Simulation including δ-rays and noise

As a final step the δ-rays production has been added to the simulation, in order to put in evidence the differences between the basic case with only the fluctuations and to have a simulation closer to the real behaviour. The noise is left deactivates since it has been shown to have practically no effect.

In Figure 5.22 are shown the results of the fit performed on the kaon (left) and pion (right) distributions in view 0 and in Table 5.7 are reported the fit results.

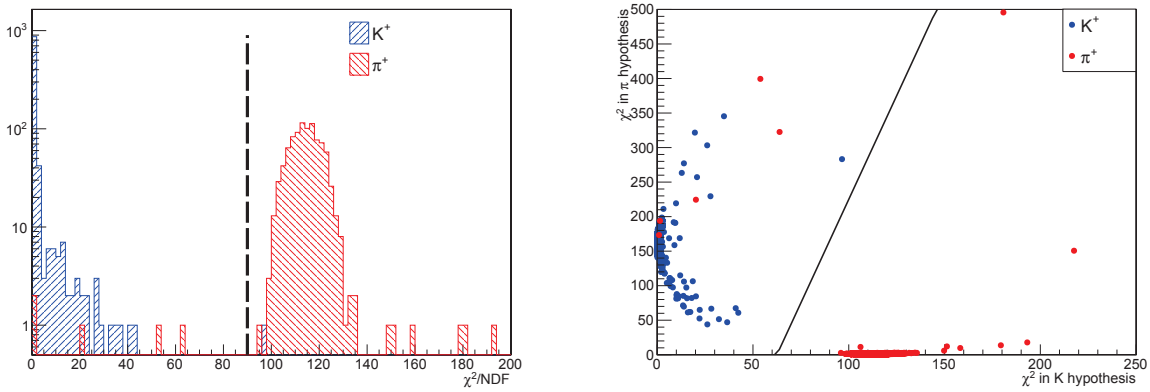

Figure 5.21: χ^2 distribution with respect to the kaon hypothesis (left) and event distributions as a function of χ^2_K and χ^2_π (right) for kaons (blue) and pions (red) in view 0 in the case of fluctuations and noise.

	View 0	View 1
A	4.575	4.598
B	−0.601	−0.597
C	2.204	2.214
D	−0.028	−0.028

	View 0	View 1
A	2.629	2.660
B	−0.744	−0.728
C	1.873	1.834
D	−0.027	−0.027

Table 5.7: Fit results for the case with δ-rays production for kaons (left) and pions (right) distributions.

Looking at Table 5.7 it is possible to compare these results with the results obtained from the parametrization in the simplest case with only fluctuations (see Table 5.1): it is possible to note some small differences between the parameters values: looking at the Figure 5.23 it is obvious that the δ-ray productions corresponds to higher values of energy losses for kaons (left) and pions (right).

This effect is visible by also observing the energy losses distributions in each bin, as shown in Figure 5.24. Here it also possible to appreciate a second effect of the δ-ray production: the width of the energy distributions increases.

δ-rays emission increases the energy deposited in some events. At bin level this explains why the energy distributions in each bin are larger than the ones with only fluctuations. At the level of the mean energy deposition also the total energy deposited is bigger than the deposition in the fluctuations case, this is an effect already observed related to the treatment of quenching for the fluctuations cases which introduce very concentrated energy

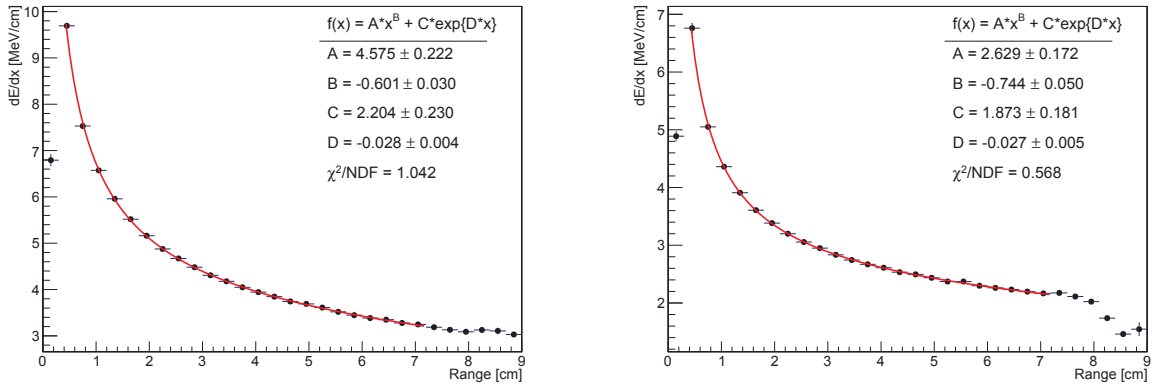

Figure 5.22: Kaon (left) and pion (right) energy losses distributions generated with δ-rays production using power law function plus exponential (5.5) for view 0.

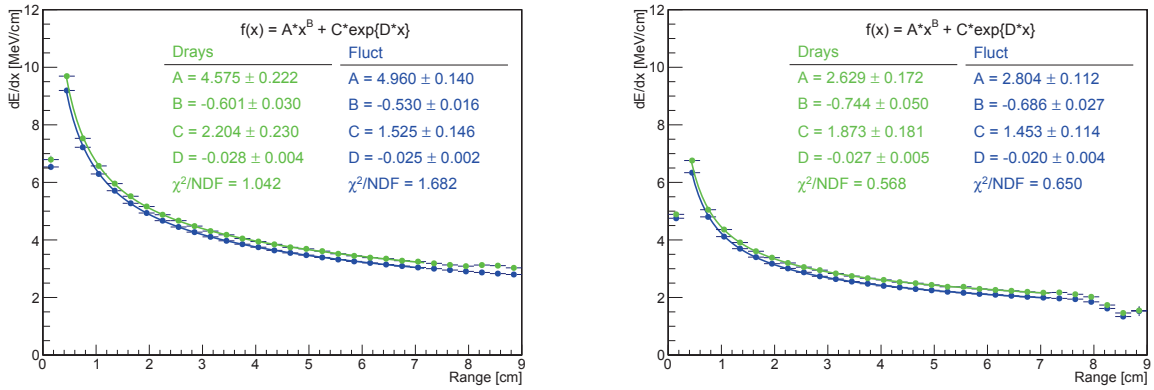

Figure 5.23: Fit comparison between the fluctuations case (blue) and δ-rays case (green) for kaons (left) and pions (right).

depositions.

These two differences are reflected in the χ^2 distributions: looking at the Figure 5.25 left, it is possible to see how the pion distribution (red area) is closer to the kaon distribution (blue area). Using the discriminant value $\tilde{\chi}^2 = 15$ it is possible to separate the populations, with the results shown in Table 5.8.

It is obvious that the δ-rays production makes more difficult to perform the particle identification separation. In particular, the single cut on χ^2_K is not sufficient anymore to distinguish kaon events (losses of $\sim 2\%$ of events).

The bi-dimensional plot in Figure 5.25 right shows how the χ^2 distribution are close to each other, however it is still possible to find a linear function capable to separate the two

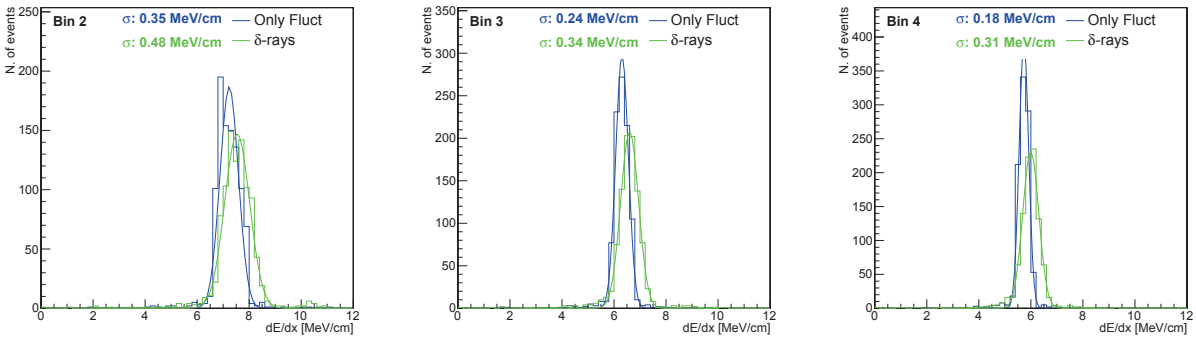

Figure 5.24: Comparison between the energy distribution for kaons in three different bins in the case of generation of fluctuations (blue lines) and the case of generation of δ-rays (green lines).

populations. By using the linear function:

$$\chi^2_\pi = 0.5\chi^2_K \tag{5.10}$$

(black straight line in the plots) it is possible to increase the number of kaons which survive to the selection, obtaining the results showns in Table 5.9.

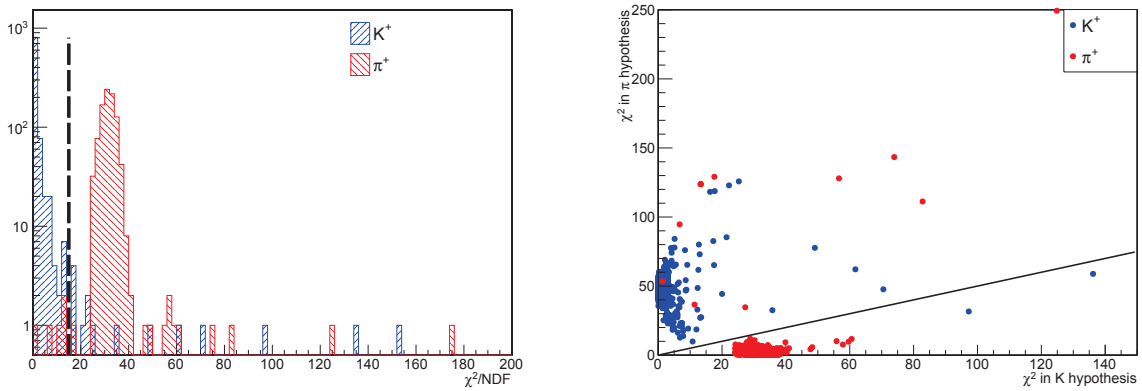

Figure 5.25: χ^2 distribution with respect to the kaon hypothesis (left) and event distributions as a function of χ^2_K and χ^2_π (right) for kaons (blue) and pions (red) in view 0.

In this case the linear cut based on the two χ^2 estimation allows improving the number of kaons well identified, but, on the other hand the number of pions misidentified is three times greater than in the case of the simple cut on the χ^2_K.

	View 0	View 1
Total K^+	956	951
Surviving K^+	938	932

	View 0	View 1
Total π^+	934	936
Surviving π^+	5	2

Table 5.8: Results of cut on χ^2_K distributions for kaons sample (left) and pions sample (right) in the case of δ-rays generation.

	View 0	View 1
Total K^+	956	951
Surviving K^+	954	950

	View 0	View 1
Total π^+	934	936
Surviving π^+	15	15

Table 5.9: Results of linear cut (5.10) on χ^2_K distributions for kaons sample (left) and pions sample (right) in the case of δ-rays generation.

5.5 Event energy cut

Another useful tool to separate kaons from pions is to study the total energy losses during the entire decay chain and to measure the total energy deposited in the events.

The most probable decay mode for the K^+ is $K^+ \to \mu\,\nu_\mu$ (B.R. = 63.55%), with a consequent muon decay $\mu^+ \to e^+\,\nu_e\,\bar{\nu}_\mu$ (B.R $\approx$ 100%). In Figure 5.26 it is shown the reconstructed track of a kaon decaying in a muon for an event simulated in the Lyon TPC. In Figure 5.27 it is possible to see the deposited energy by the kaon and by the daughter muon in view 0 (left) and in view 1 (right).

Looking at Figure 5.27 left (*i.e.* view 0) one can see the energy deposited by the kaon increasing while going from the kaon starting point, on the left side, up to the peak value corresponding to the stopping point of the kaon. Then the constant energy deposition visible at the right of the plot corresponds to the deposited energy by the daughter muon.

In Figure 5.27 right (view 1) a clear separation among the two particles in the profile of the energy distribution is less evident. This is due to the short length of the muon track in this view (compare Figure 5.27 right). However it is still very evident the characteristic shape of the increasing energy deposition of the kaon up to its stopping point from the right (starting point) to the left (stopping point).

Proton decay is a two body process, so the kaon momentum is fixed. Neglecting the Fermi motion, a proton in argon nucleus has a total energy E_p = 938.27 MeV. This implies that the daughter kaon has a monochromatic momentum p_{K^+} = 339.26 MeV/c (as mentioned before) and a kinetic energy $E^{kin}_{K^+}$ = 105.33 MeV. At the end of the range, the kaon decays at rest, producing a muon with p_{μ^+} = 235.54 MeV/c and $E^{kin}_{\mu^+}$ = 152.50 MeV.

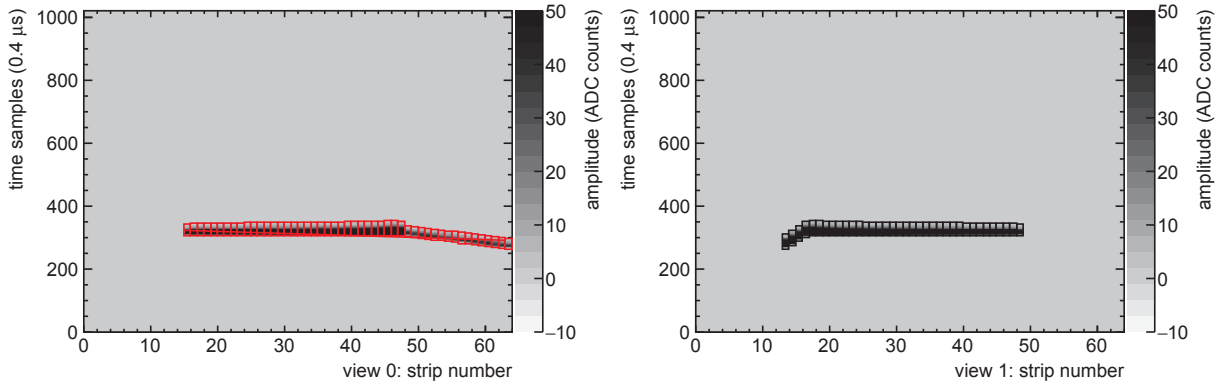

Figure 5.26: Event display for a kaon decay simulated in the Lyon TPC. It is possible to distinguish the daughter muon track in both views. It is also interesting to notice how in view 0 the muon track is not completely contained in the detection region.

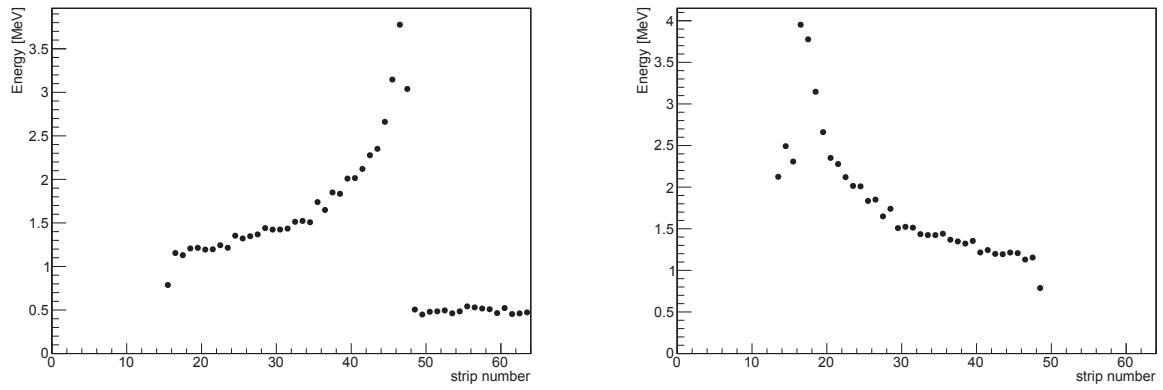

Figure 5.27: Energy deposition for a kaon decay event in view 0 (left) and in view 1 (right). In this figure are reported the deposited energies per strip instead of the $\mathrm{d}E/\,\mathrm{d}x$ since it is not possible to know the distance traveled in the strip by the particles by using only the information at the hit level.

Finally the muon decays via a three body process, so the daughter particles have not a fixed momentum (and energy). It is possible to calculate the maximum momentum transferred to the positron, which is $p_{e^+,max} = 52.82$ MeV/c. Consequently the maximal kinetic energy is $E^{kin}_{e^+,max} = 52.32$ MeV. The muon decay kinematics is exactly the same in the case of muons coming from kaon or pion decays. In order to distinguish these two mother particles it is more interesting to compare the kinetic energy of the mother particle plus the one of daughter muon, neglecting the energy of the electron from the muon decay which would

not introduce any further discrimination. In the case of a kaon decay the total kinetic energy of the mother particle plus the muon amounts to $E^{kin}_{K,\mu} = 257.83$ MeV.

For the pion, the most probable decay is $\pi^+ \to \mu^+ \nu_\mu$, with a consequent muon decay in electron and neutrinos. A pion with a momentum $p_{\pi^+} = 140$ MeV/c is considered, since a pion with this momentum has a track length comparable to the track length of a kaon with $p_{K^+} = 339.26$ MeV/c, as mentioned in section 5.2. The kinetic energy of this pion is $E^{kin}_{\pi^+} = 58.12$ MeV. At the end of the range the pion decays and produces a muon with $p_{\mu^+} = 29.80$ MeV/c which corresponds to $E^{kin}_{\mu^+} = 4.12$ MeV. Finally the kinetic energy for the pion plus the muon is $E^{kin}_{\pi^+,\mu} = 62.24$ MeV. This value can be compared to the one obtained before for the kaon ($E^{kin}_{K,\mu} = 257.83$ MeV).

To record all the energy of these processes it is necessary to have a sufficiently large detection volume, of the order of 1 m size, in particular in order to contain the daughter muon. The muon produced by the kaon decay has a $\beta\gamma \sim 2.23$. It implies that the range R travelled by the muon in the liquid argon before stopping is (see Figure 5.28)

$$R/M \simeq 700 \text{ g cm}^{-2} \text{ GeV} \tag{5.11}$$

namely

$$R_\mu \simeq 52.88 \text{ cm} \tag{5.12}$$

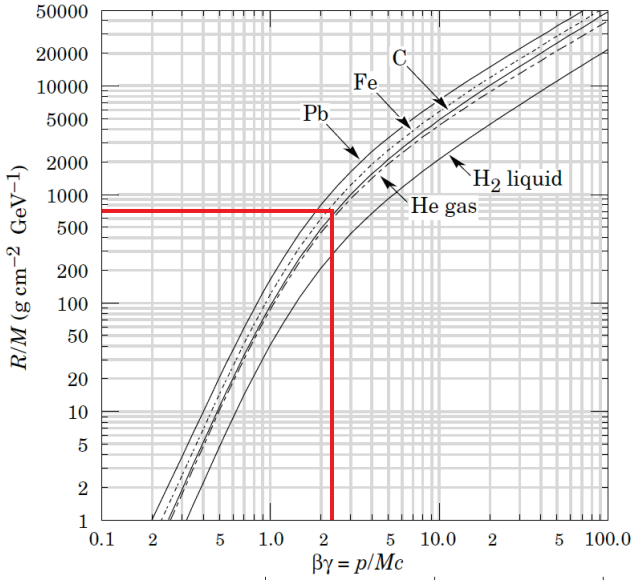

Figure 5.28: Range of charged particle. The $\beta\gamma$ value for a muon with $p_{\mu^+} = 235.54$ MeV/c corresponds to $R/M \sim 700$ g cm^{-2} GeV.

Large detectors as DUNE 10 kt are completely containing these events within their fiducial volume. The distinction on the total kinetic energy of the mother candidate plus

the muon (257.83 MeV for a kaon decay and 62.24 MeV for a pion decay) can be fully applied.

Figure 5.29 shows the WA105 event display for a simulated daughter muon with an initial momentum $p = 235.54$ MeV/c (top and bottom left) and for a muon with an initial momentum of $p = 29.80$ MeV/c. The difference between the energy depositions and the hits topologies in the two cases is evident.

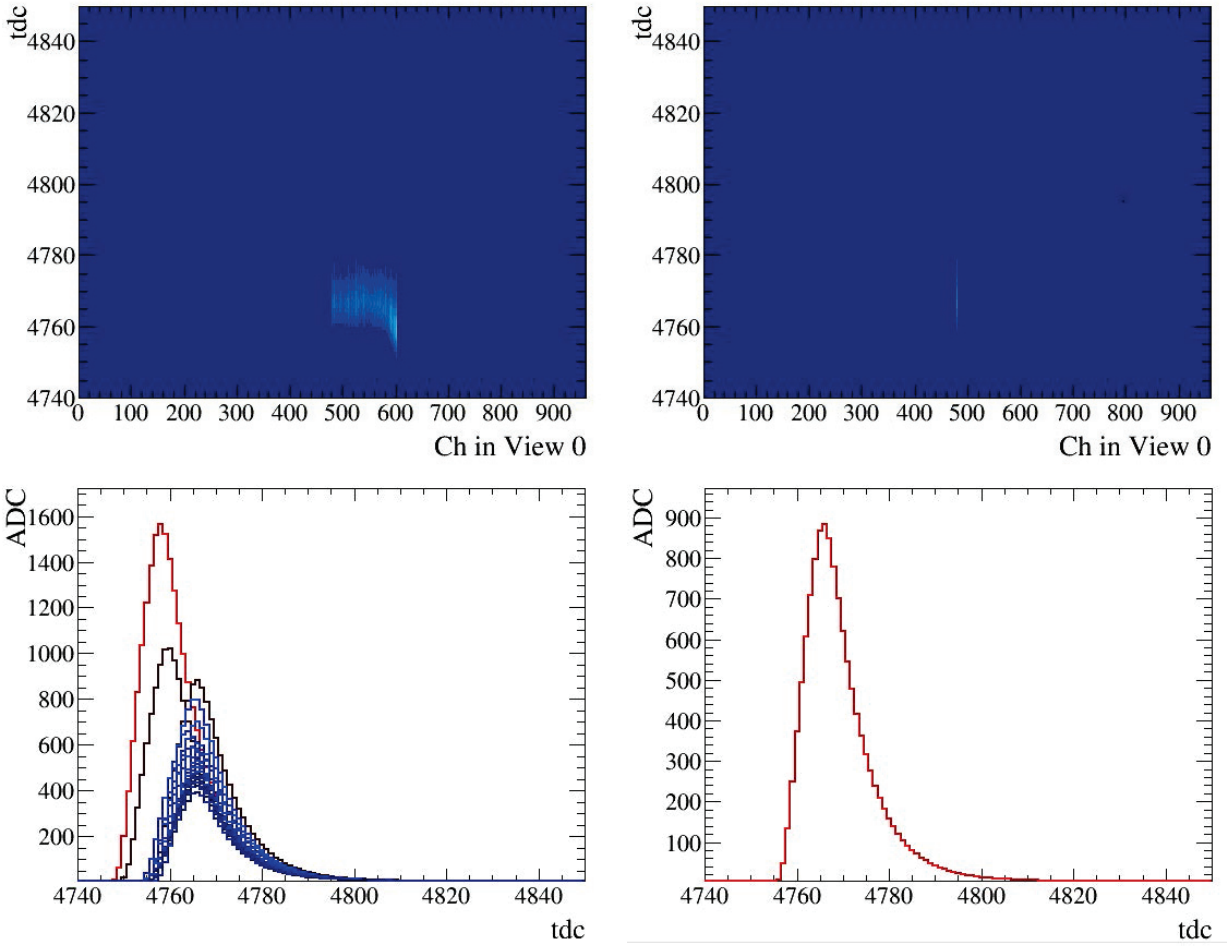

Figure 5.29: Event display for the $6 \times 6 \times 6$ m^3 detector: the drift time versus channel number of the reconstructed hits (top) and raw waveforms showing the amplitude of the signal on one view (bottom) for a muon with an initial momentum obtained from a kaon decay at rest, leaving hits on about 100 readout channels (left) and obtained from a pion decay at rest, depositing its energy in a single hit (right).

The typical energy resolution on the kinetic energy obtained by integrating the energy losses for stopping tracks in a liquid argon TPC is of the order of 1% as shown by the ICARUS collaboration [91]. In Figure 5.30 it is shown the simulated distribution of the

total charge deposited by muons with an initial momentum $p = 235.54$ MeV/c (left) and by muons with an initial momentum of $p = 29.80$ MeV/c. The resolution obtained is 0.3% in the case of muons generated from kaons and 1.4% in the case of muons produced by pions.

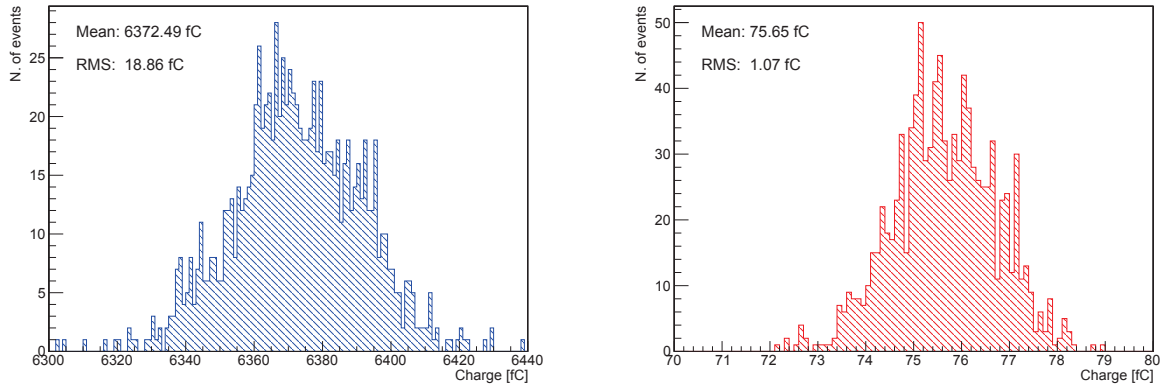

Figure 5.30: Total charge deposition for 1000 muons with an initial momentum compatible to that obtained from a kaon decay at rest (left) and to that obtained from a pion decay at rest (right) by using the WA105 charge readout simulation.

This figure would correspond to a huge separation power by considering the fixed values of the kinetic energies quoted above. This rejection criterion can be applied also to the kinetic energy of the mother track by looking at its total deposited energy. However in this case the measurement would have some large correlation with the one based on the exploitation of the end-of-range energy losses measurements.

Even if most of the separation power between kaon and pion decay chains can be achieved just by the kinetic energy measurement of the daughter muon and of the mother particle, the identification of the mother particle is a necessary criterion to prove that the mother particle is a kaon. The analysis presented in this Chapter is mainly focused on the discrimination by particle identification at the end of the range by simulating a setup with a diameter $d = 27.15$ cm which does not contain the entire the muon track before it stops. For this reason it is not possible to apply directly in the analysis a cut on the total energy of the daughter and mother particle to the samples used for the end-of-range studies. However it is interesting to consider at least the energy losses of the mother particle by comparing the measured integral of the energy losses of the kaons to the one measured for pions. The discrimination power coming independently from the measurement of the daughter muon is anyhow evident as shown in Figure 5.30.

In Figure 5.31 are shown the different integrated energy losses distributions for kaons (left) and for pions (right). It is important to remark that these energy distributions are not corrected by the quenching factor, similarly as for all the other energy measurements reported in this analysis: this is the reason for which the mean energy deposited looks

different with respect to the kinetic energy calculated before.

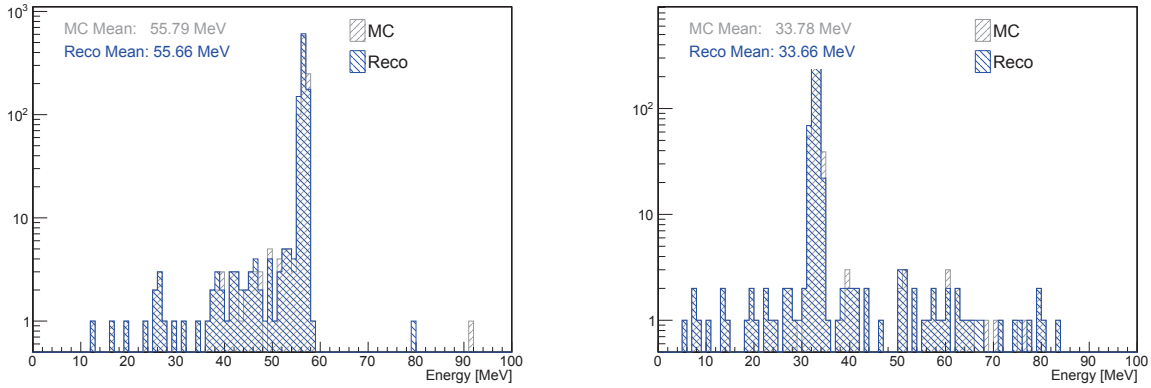

Figure 5.31: Comparison between Monte Carlo (gray) and reconstructed (blue) integrated energy losses in the view 0 for kaons (left) and pions (right) tracks. The energy values are not corrected by the quenching factor.

It is also interesting to note that these distributions include all the events, without any restriction on the track length.

In Figure 5.32 it is possible to see the reconstructed energy distribution for the kaons (left) and for the pions (right) for the three different simulation cases studied: only fluctuations (top), noise generation (center) and δ-rays production (bottom). The events taken into account for these plots are the ones that satisfy the constraint on the track length described in Section 5.3: this allows eliminating the low energy events from the reconstructed energy losses distribution. The Monte Carlo distribution shown for comparison is still corresponding to the total statistics before the track length cut.

Finally it could be very useful to exploit the relation between the total energy deposition in the event and the χ^2_K of the same event. In Figure 5.33 it is shown the bi-dimensional plot with the energy (y axis) as a function of χ^2_K (x axis) for the kaons (blue dots) and pions (red dots). The two populations are well separated with respect to the χ^2_K variable, as seen in section 5.4; they are well separated also with respect to the total energy deposited, as described above. Some π events with a small χ have an energy deposition greater than the majority of the kaons events. This is explainable with the fluctuations effects.

It is now possible to add an energy cut to the cut on χ^2_K. As described in Section 5.4, the χ^2_K cut used is $\tilde{\chi}^2_K = 120$. For what concerns the deposited energy, by looking at Figure 5.32 top, it is reasonable to choose as a discriminant the value $\tilde{E} = 60$ MeV. The number of events with $\tilde{\chi}^2_K < 120$ and $\tilde{E} < 60$ MeV is reported in Table 5.10 (in Figure 5.33 the bottom region on the left, delimited by the dashed lines).

In Figure 5.34 the distributions of energy deposition as a function of χ^2_K for the simulation with the noise effects are reported. It is obvious that the situation is very similar to the case without noise described above. This is in agreement with what found in Section

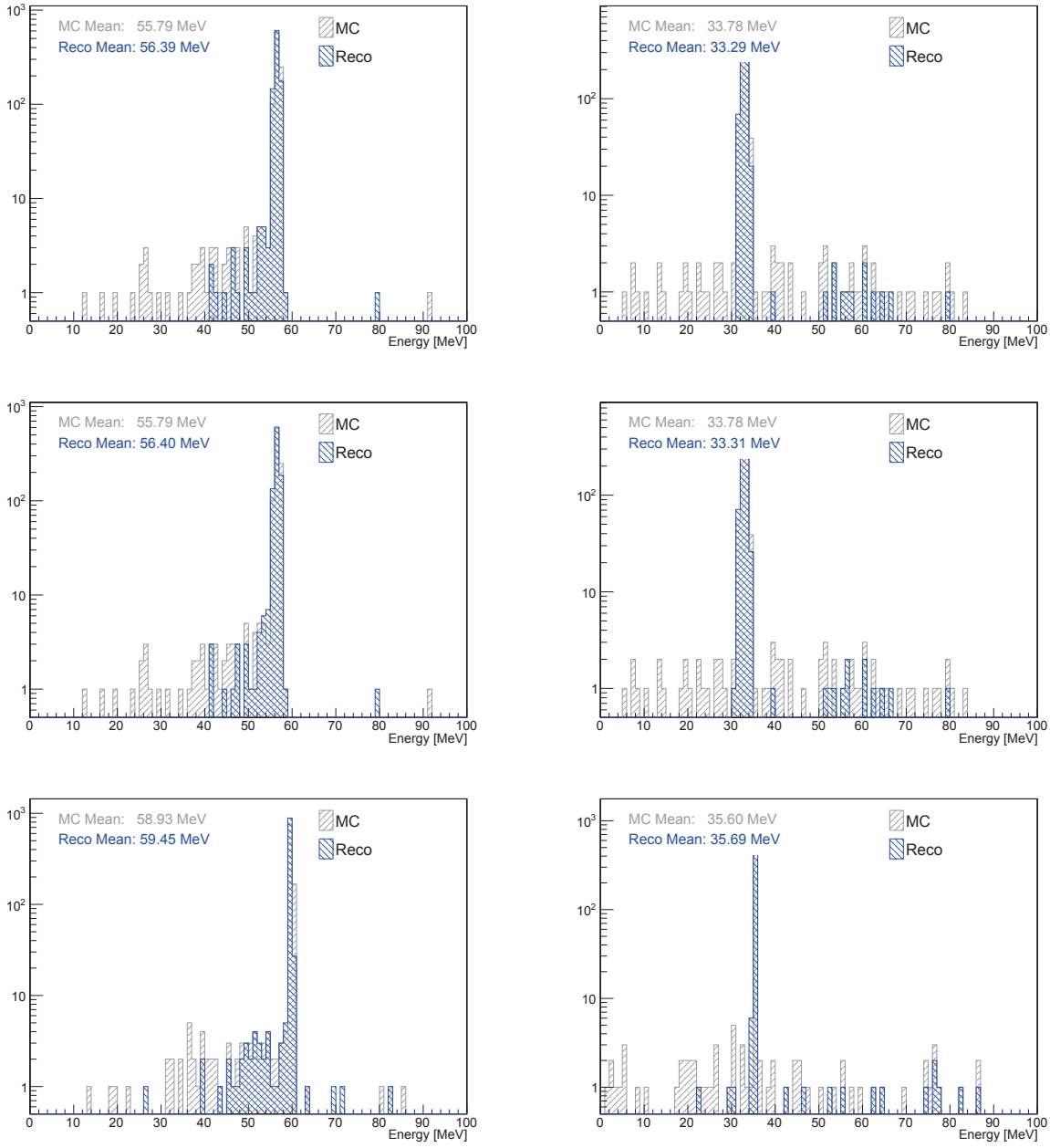

Figure 5.32: Comparison between Monte Carlo (gray) and reconstructed (blue) kaons (left) and pions (rigth) integrated energy losses for the events with the requirement of $l_{view} \geq 7.5$ in the view 0 for the reconstructed distribution. The distributions are shown for the following simulation cases: only fluctuations (top), noise generation (center) and δ-rays production (bottom). The energy values are not corrected by the quenching factor.

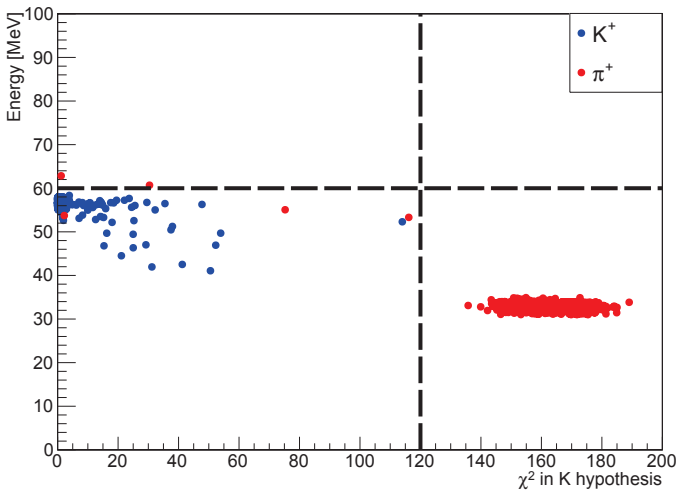

Figure 5.33: Total energy deposited as a function of χ^2_K for kaons (blue dots) and pions (red dots) in view 0 in the basic simulation case with only fluctuations effects.

	View 0	View 1
Total K^+	958	959
Surviving K^+	957	958

	View 0	View 1
Total π^+	933	928
Surviving π^+	3	0

Table 5.10: Results of energy and χ^2_K cuts for kaons sample (left) and pions sample (right) in the case of only fluctuations effects.

5.4, where it is shown that the changes to the simulation related to the noise generation are negligible. Combining the χ^2_K cut using in the Section 5.4 $\tilde{\chi}^2_K = 120$ with the energy cut $\tilde{E} = 60$ MeV (look at Figure 5.32 center), the number of events with $\tilde{\chi}^2_K < 120$ and $\tilde{E} < 60$ MeV is reported in Table 5.11.

	View 0	View 1
Total K^+	958	959
Surviving K^+	956	958

	View 0	View 1
Total π^+	933	928
Surviving π^+	3	0

Table 5.11: Results of energy and χ^2_K cuts for kaons sample (left) and pions sample (right) with the simulation including noise generation.

Looking at the simulation with the δ-rays productions, the situation is quite different.

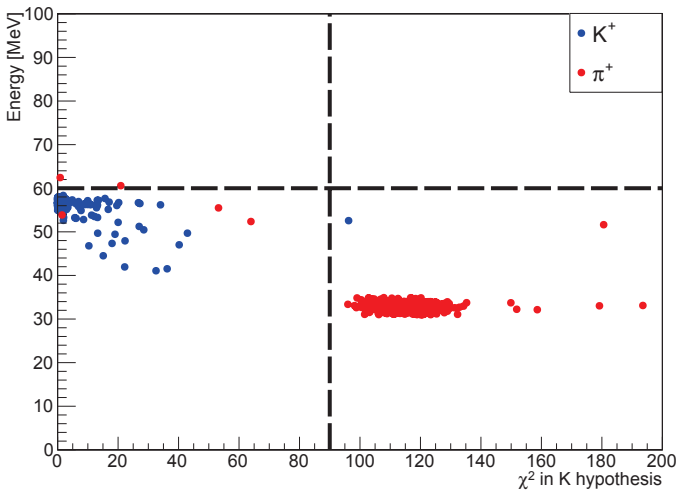

Figure 5.34: Total energy deposited as a function of χ^2_K for kaons (blue dots) and pions (red dots) in view 0 with the simulation including noise generation.

Looking at Figure 5.35 it is possible to note how the pions population has now a small χ^2_K, very near to the kaons population (as seen in Figure 5.25): δ-ray production increases the energy deposition in some bins (as seen in Figure 5.24), and this contributes to produce a small χ^2_K. Because the average energy deposited by the pion is smaller than the one deposited by the kaons (see Figure 5.32), it is useful to introduce a lower cut on the energy. So, in this case, the conditions to discriminate kaons and pions are: $\tilde{\chi}^2_K < 160$ and 38 MeV $< \tilde{E} <$ 72 MeV. The energy cuts allow increasing the χ^2_K threshold in order to accept more kaons events. The results of this selection are reported in table 5.12.

	View 0	View 1
Total K^+	956	951
Surviving K^+	952	948

	View 0	View 1
Total π^+	934	936
Surviving π^+	6	3

Table 5.12: Results of energy and χ^2_K cuts for kaons sample (left) and pions sample (right) in the case of δ-rays generation.

By taking into account the energy discrimination only one could have set a cut around $\tilde{E} = 40$ MeV. The idea of the energy cut which has been eventually adopted is to improve the result of the χ^2_K cut by using also the information from the total energy deposition. From the scatter plot corresponding to the simulation with fluctuations only one can notice a population of events from pions at low χ^2_K which would not be eliminated by the cut at $\tilde{E} = 40$ MeV and a few of them tend to be greater than 60 MeV. That motivates the idea

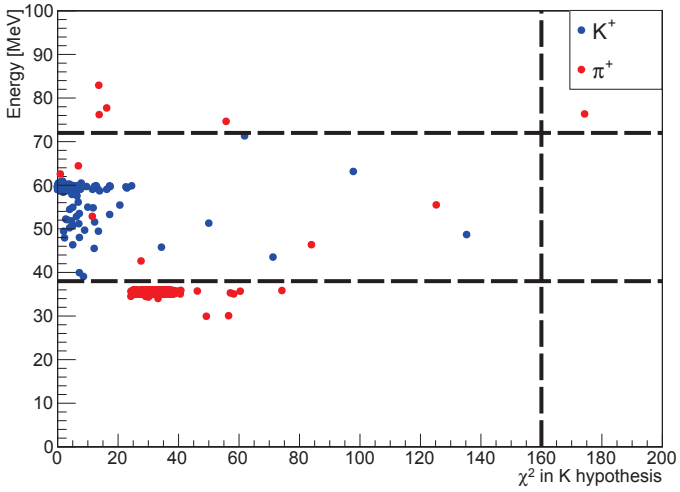

Figure 5.35: Total energy deposited as a function of χ^2_K for kaons (blue dots) and pions (red dots) in view 0 in the case of δ-rays generation.

of a cut at high energy. In case of the delta rays the cut at 40 MeV was necessary in order not to lose too many kaons with the χ^2_K cut since the two populations became closer in χ^2_K. Still some pion events beyond 40 MeV are present also in this case and motivate a cut at 72 MeV. The reason why pions tend to produce this tail at higher energy beyond 40 MeV (see also Figure 5.32) is related to the fact that the pion is lighter than the kaon and this generates larger fluctuations in the energy depositions. Indeed given the lighter pion mass the maximal transferred kinetic energy in the delta ray production is larger than in the kaon case. It seems this effect is also simulated in the energy losses fluctuations without explicit delta ray production.

Finally, similarly to what has been done above, it is interesting to study also the relation between the total energy deposition in the event and the χ^2_π of the same event. Figure 5.36 shows the bi-dimensional plots with the energy (y axis) as a function of χ^2_π (x axis) for the kaons (blue dots) and for the pions (red dots) in the three different cases: only fluctuations (left), fluctuations and noise (center) and δ-rays and noise (right).

Following the idea used above in the analysis of the bi-dimensional plots of the total energy deposition as a function of χ^2_K, two cuts ($\tilde{E}$ on the energy value and $\tilde{\chi}^2_\pi$ on the χ^2_π value) can be introduced to separate the kaons and pions populations. In the case with only fluctuations and fluctuations and noise the cuts used are $\tilde{E} = 40$ MeV and $\tilde{\chi}^2_\pi = 40$. In the case of δ-rays generation the cuts are $\tilde{E} = 40$ MeV and $\tilde{\chi}^2_\pi = 12$. The results of these selections are reported in Tables 5.13, 5.14 and 5.15. It is evident that these results are very similar to those obtained when comparing the total energy loss with χ^2_K.

The exploitation of the total energy losses of the mother track is, as expected, largely correlated to the rejection power provided by the end-of-range profile, however it helps in improving the rejection power. Overall, for the simulation including the δ-ray production

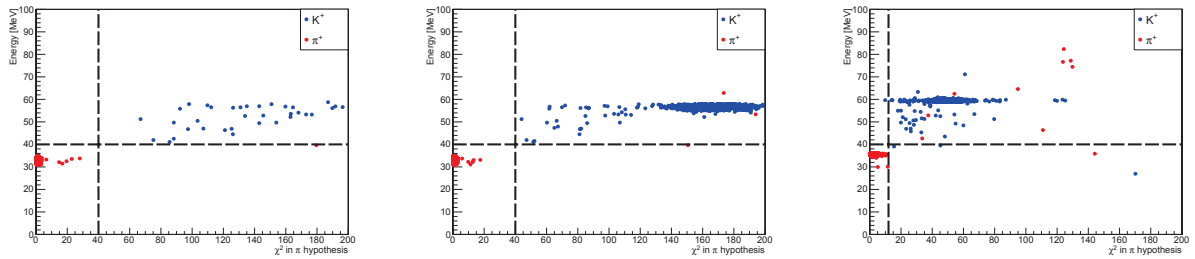

Figure 5.36: Total energy deposited as a function of χ^2_π for kaons (blue dots) and pions (red dots) in view 0 in the case with only fluctuations (left), including the noise generation (center) and in the case of δ-rays generation (right).

	View 0	View 1
Total K^+	958	959
Surviving K^+	958	958

	View 0	View 1
Total π^+	933	928
Surviving π^+	13	10

Table 5.13: Results of energy and χ^2_π cuts for kaons sample (left) and pions sample (right) in the case of only fluctuations effects.

and corresponding to a realistic case, the application of an additional cut on the total energy losses of the mother particle helps in improving the pion rejection by about a factor 3 with respect to the selection performed by exploiting only the energy losses profile bringing the pion contamination at the few per mille level. Further rejection power can be obtained by exploiting the integral energy losses of the daughter muon 152.50 MeV in case of a kaon decay vs 4.12 MeV for a pion decay. This separation is completely independent from the previous one based on the mother particle. Assuming 1% accuracy on the kinetic energy measurements there is a quite evident separation both in terms of range and of total energy of the daughter muon, even by taking into account a possible deterioration due to delta-rays fluctuations and quenching effects. The final kaon identification algorithm for the proton decay search can be based on an independent analysis treatment of the mother track by measuring the energy losses profile close to the stopping point and also the integral of the energy losses, combined with the independent handle relying on the measurement of the daughter muon energy and range, which is potentially providing a striking discrimination factor.

	View 0	View 1
Total K^+	958	959
Surviving K^+	958	957

	View 0	View 1
Total π^+	933	928
Surviving π^+	13	10

Table 5.14: Results of energy and χ^2_π cuts for kaons sample (left) and pions sample (right) with the simulation including noise generation.

	View 0	View 1
Total K^+	956	951
Surviving K^+	952	949

	View 0	View 1
Total π^+	934	936
Surviving π^+	15	17

Table 5.15: Results of energy and χ^2_π cuts for kaons sample (left) and pions sample (right) in the case of δ-rays generation.

5.6 Summary

The study of energy losses provides an important handle for particle identification. In this Chapter it has been shown how an accurate measurement of energy losses at the end of the range R allows separating kaons and pions.

The Monte Carlo kaon sample used for this analysis has been produced with the kinematical characteristics similar to the kaons which would be produced by proton decay (*i.e.* with a momentum $p_{K^+} = 340$ MeV/c). The Monte Carlo pion sample has been produced with an initial momentum such that the length of the ionization track in liquid argon is similar to the one of such kaons, in order to have a comparable analysis lever arm with respect to the stopping point of the two particles.

After sampling at the hits level the kaons and pions energy depositions, a parametrization has been computed to describe the energy losses of these particles nearby their stopping point. The most suitable function for this parametrization $\mathrm{d}E/\,\mathrm{d}x$ is found to be a linear combination of a power law function and an exponential. By using this parametrization, a χ^2 has been defined in order to separate the two populations.

In order to understand different effects in the simulation, the analysis has been performed at increasing levels of complication.

Analysing the samples where the noise simulation and δ-rays production were deactivated, the efficiency for kaon identification is 99.9%, with a pion misidentification rate of 0.6%. The same result has been achieved in the simulation with the noise production. When the δ-rays production is activated for a comparable kaon identification efficiency (99.8%) the pion misidentification rate grows up to 1.7%. This is due to the larger dis-

persion of the energy distribution in each bin of distance from the stopping point. This dispersion is caused by the fluctuations related to δ-rays energy depositions.

This numbers give an idea of the rejection power achievable from charge readout analysis standalone for the kaon identification. A further separation between kaon and pion samples can been achieved looking at the kinematic of all the processes involved: kaons and pions decay produces $\mu\nu_\mu$ which a subsequent μ decay in $e\nu_e\nu_\mu$. The difference between the two processes lies in the kinetic energy of the kaon or the pion plus the one of the daughter muon (for a kaon decay the total kinetic energy amounts to $E^{kin}_{K,\mu} = 257.83$ MeV, for a pion decay to $E^{kin}_{\pi,\mu} = 62.24$ MeV). This additional handle can be exploited for the kaon to pion separation although the integral energy losses of the mother particle are expected to have a good degree of correlation with the energy losses profile analysis already applied. This point has been verified by comparing the mother particle total energy deposition to the χ^2 of the particle identification based on the energy losses close to the stopping point. This brings to a lower pion misidentification rate of 0.6% in the complete simulation case including also δ-rays production. The measurement of total energy and range of the daughter muon provides a completely independent handle with striking discrimination power against the pion background. This additional discrimination from measurement of the daughter muon can be then combined with the analysis developed in this Chapter, which is anyhow primarily needed in order to provide a direct kaon identification.

Chapter 6

Electron/photon separation and π^0 rejection

In an experiment studying $\nu_\mu \rightarrow \nu_e$ oscillations the reconstruction of electromagnetic showers is a crucial step in the neutrino events reconstruction because it represents the evidence of the electron production from a ν_e CC interaction. The electron identification and the measurement of its energy provide essential information about the incoming neutrino.

Apart the intrinsic ν_e contamination at production in the neutrino beam. The first source of background for this process is represented by showers produced by a photons originating by π^0 decays. π^0 can be easily produced in neutrino interactions. In a neutral current neutrino interaction a photon conversion occurring close to the primary neutrino vertex can mimic a final state topology quite similar to the one of a ν_e CC interaction.

In Figure 6.1 it is possible to see a simulated shower generated by an electron and on the right a shower generated by a photon. The two showers are very similar: it is very important to develop an algorithm that allows to distinguish the mother particle originating the showers.

In order to disentangle the mother particle of the electromagnetic shower it is possible use two handles in the charge readout analysis: first of all, a shower generated by an electron stems from a visible track coming from the neutrino interaction vertex; a shower generated by a photon, on the contrary, will have a gap between the primary vertex where the photon is generated and the point where the conversion in an electron/positron pair occurs, *i.e.* the point from where it is possible to start detecting the shower. This is also visible in Figure 6.1 where the Monte Carlo production point of the two particles was the same. This topological difference can be used to do a primary selection between the showers originated by a photon and those originated by an electron.

The second important discriminating element between a photon shower and an electron shower is the energy profile deposited at the beginning of the cascade. The shower generated by an electron is originated by a single charged particle: the deposited energy profile should be compatible with that hypothesis. The photon generates a pair of charged particles, so the energy deposited at the beginning of the shower is double with respect to the case of a genuine electron shower.

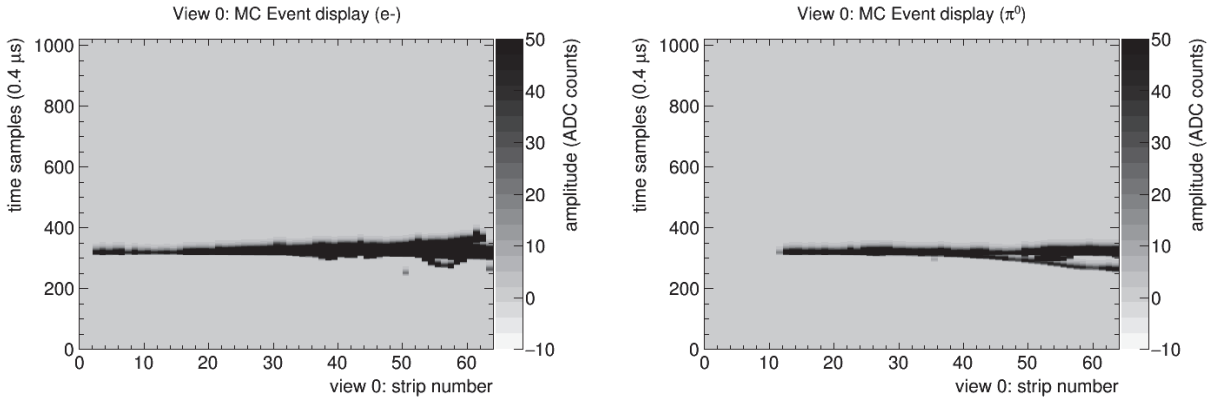

Figure 6.1: Event display for a shower generated by an electron (left) and a photon produced by π^0 decay (right).

This Chapter describes the analysis performed in order to obtain a parametrization of the ionization charge profile produced in an electromagnetic shower as a function of the distance from the starting point of the cascade, and a definition of the analysis procedure allowing to distinguish the originating particle of the shower.

As it will be shown later the charge readout pitch has a crucial role in the charge profile and distance measurements. First a description of the definition and generation of the Monte Carlo samples used in order to obtain the average charge collection is provided. The reconstruction technique is then described in order to compare the charge generated by an electron shower and the one generated from a photon, comparing the results obtained using the dual-phase readout (strips width of 0.3 cm) and a pitch similar to the one foreseen for the single-phase wires pitch readout (strips width of 0.6 cm). Finally a comparison between the simulation results without and with noise effects in the readout is presented.

6.1 Definition and generation of the Monte Carlo samples

The purpose of this study is to define a procedure to distinguish the electromagnetic showers generated by an electron from those generated by a photon. The electron candidates generating the shower are potentially the resulting particles from ν_e CC interactions. The typical energy of the electron associated to the ν_e CC interaction is in a range of energies from 0.5 GeV to 4 GeV. For this reason the Monte Carlo samples generated for this study correspond to a uniform distribution in the energy range between 0.5 GeV to 4 GeV, as shown in Figure 6.2. The results obtained with this flat distribution are more general can be easily re-weighted for any ν_e CC interactions production spectrum.

In order to study the simplest configuration, the electrons and the photons are generated

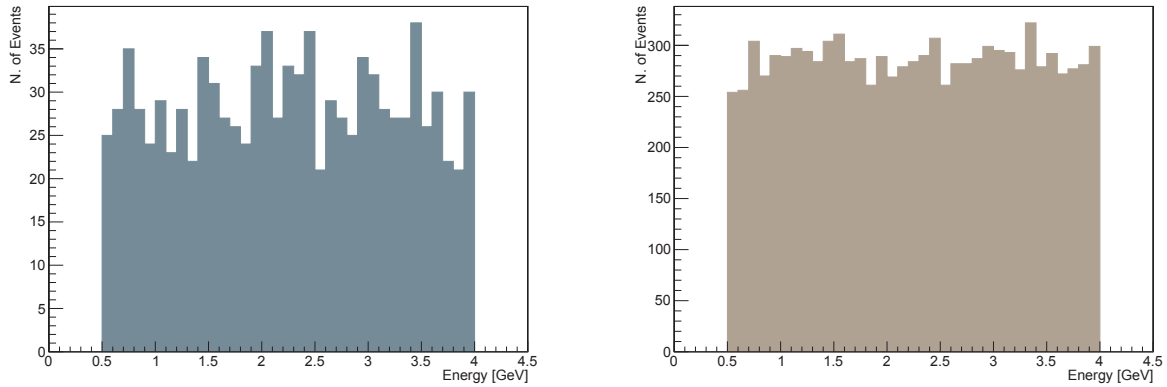

Figure 6.2: Monte Carlo primary energy for electrons samples (left) and for photons samples (right), corresponding to a flat generation spectrum.

with momenta parallel to the anode plane. In order to be symmetric with respect to the two readout views, particles have been generated with an incoming planar angle $\varphi = 45°$ with respect to the strip orientation.

The generation point of the particles has been chosen close to one of the borders of the active region in order ensure a good containment of the energy deposited by the showers. In particular, the coordinate of the electrons and photons generation has been defined at the beginning of the third strip: hence, it is possible to state that the minimum distance travelled by the particle is the length of the strip divided by the incoming angle φ, *i.e.* $d_{min,strip} = 0.3\sqrt{2}$ cm. The choice of putting the generating coordinates inside the active volume allows to get a complete sampling of the energy losses.

The electrons sample consists typically of 1000 events. The photons sample consists of 10000 events: the reason why this second sample is ten times larger is that the showers generated by a photon have to satisfy a proximity constraint, as described in Section 6.2 to be selected in the analysis. This implies a strong reduction of the sample (loss of about 80% of the events). The number of produced events has then been increased consequently in order to achieve a reasonable statistic for the final analysis.

In first instance, in order to study at the basic level the energy depositions and to reduce the uncertainties related to the electronic response, the noise has been deactivated in the simulation. This assumption reflects in particular the situation of the dual-phase TPC where noise represents at most 1% of the signal of a particle at the ionization minimum and can be safely neglected in this analysis. During this first part the only effects taken into account are the fluctuations, parametrized by `GEANT4` using the Landau-Vavilov-Gauss distribution. In this simulation the δ-rays production has not been deactivated, because this is an electromagnetic process activated above a fixed threshold. To deactivate this production would imply to apply a cut on the shower propagation. In the final part of the analysis a noise production similar to the one of a single phase detector has been activated

in order to see the differences between the two cases.

6.2 Energy profile reconstruction and *electron*/γ separation

In this study, differently from what has been done in the other Chapters, the variable used for the analysis is the collected ionization charge: as seen in Chapter 4, there is a linear relationship between collected charge and reconstructed energy, so these quantities are equivalent.

In the case of muons (Chapter 4), kaons and pions (Chapter 5), particles have a well known trajectory and it is reasonable to compute the mean energy loss in a strip as the collected energy in a strip divided the effective distance travelled over the same strip (known from the particle trajectory).

In the electromagnetic showers, with many particles contributions, apart for the initiating track, it is not possible to know the distance traveled by the individual charged particles over the strips. For this reason, the variable taken into account in the analysis is just the total charge collected in each strip. It is also important to stress that the collected charge used as discriminating variable in this analysis is not corrected by the recombination effects. In order to study the discrimination power which is based on a relative comparison it is not needed to correct for quenching effects but just to take them correctly into account. The simulation is all inclusive of the quenching effects. Effects related to the charge attenuation during the drift due to electronegative impurities are not simulated, we assume however that in the final analysis on real data the collected charge will be corrected for the attenuation losses during the drift by using the knowledge of the event t_0 from the scintillation light and/or the beam time tagging and the measured purity levels.

In the measurements of the collected charge, the only information used is at hits reconstruction level, in order to avoid possible errors related to the clustering or tracking algorithms.

The crucial difference between a shower generated by an electron and the one generated by a photon is the amount of energy deposited at the beginning of the shower: the photon converts into an electron/positron pair. The electron and positron tracks are practically overlapped and impossible to disentangle within the resolution of the detector. They will appear as a single track originating the electromagnetic shower as in the case of a genuine electron. However a double quantity of ionization is produced with respect to the case where a single electron generates the shower. This difference in the ionization will be visible at the level of the detected charge in the strips.

The goal of this work is to compare the average charge collected over several strips along the track originating the shower and to define a cut in order to distinguish the origin of the showers.

The choice of the number of the strips used to evaluate the mean charge deposited by the track initiating the shower must be large enough to take into account a reasonable

sampling of the path travelled by the particle, but it does not have to be too big in order to avoid including in the calculation the charge deposited when the shower starts to be fully developed.

The first step in the reconstruction process consists in measuring the charge deposition in each strip since the beginning of the shower: for a shower generated by an electron the starting point corresponds to the Monte Carlo generation point of the electron, so this is the same for all the events (in the strips coordinate system chosen it corresponds to the third strip).

For a shower originating from a photon conversion the situation is different: the starting point of the shower is the point where the electron/positron pair is generated by the photon conversion and the distance of this point from the Monte Carlo generation point of the photon is variable following an exponential distribution with a decay constant given by the conversion length, which is 9/7 of the corresponding radiation length in liquid argon X_0.

The measurement of this gap distance d_{shower} can be used as discriminant to understand if the shower is generated by a photon or not: if the distance is not 0, within the detector space resolution, it is obvious that the shower is generated by a photon. In Figure 6.3 it is possible to appreciate the importance of the measurement of d_{shower}. In both cases the particles have been generated in the same position (in the strips coordinate system, the third strip). On the left the primary particle is an electron and the charge collection starts at the third strip. On the right the primary particle is a photon: the charge deposition starts after some strips: this gap is the proof that a photon travelled this region of the space before converting.

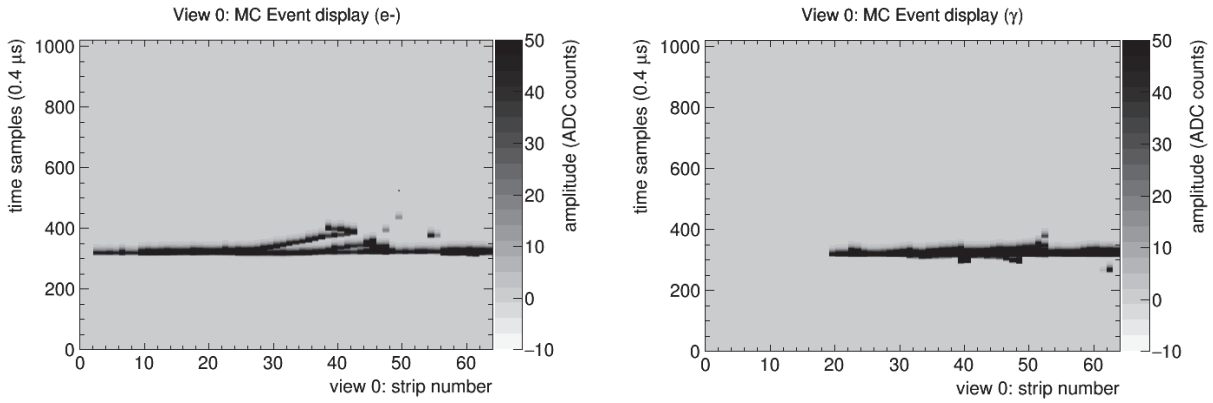

Figure 6.3: Event display for a shower generated by an electron (left) and by a photon (right). For the electron, the shower starting point corresponds to the Monte Carlo generation point (strip n. 2). In the photon event the gap between the Monte Carlo generation point (strip n. 2) and the starting point of the shower is d_{shower}.

The deposited charge measurement and the measurement of d_{shower} are strongly dependent on the strips pitch: in the following part of this section a comparison between a

dual-phase TPC, with a strip pitch of 0.3 cm and a single-phase TPC, with a strip pitch of 0.6 cm is presented. In the case of a $pitch = 0.3$ cm, the active volume used in the analysis is covered by 64 strips; in the other case, where the strip dimension is 0.6 cm, the total number of the strips is 32.

In Figure 6.4 are shown the average charge depositions in each strips for the view 0 in the case of $pitch = 0.3$ cm (top) and $pitch = 0.6$ cm (down); for the electrons (left) shower all the events are taken into account to evaluate the average charge. For the photon showers (right) the events taken into account to produce the plot are those which have a $d_{shower} = 0$.

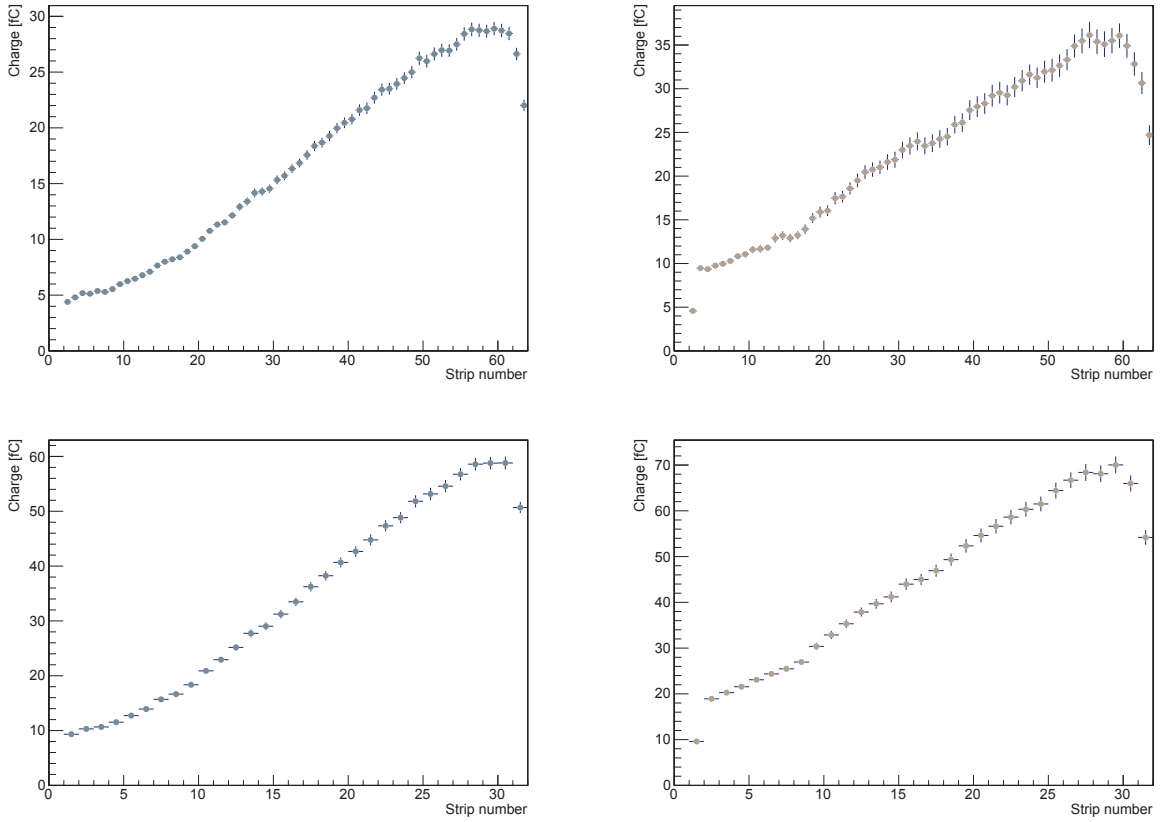

Figure 6.4: Top: average charge collected in each strip for a shower originated by electron (left) and by photon (right) for a typical dual-phase TPC pitch of 0.3 mm. Bottom: average charge collected in each strip for a shower originated by electron (left) and by photon (right) for a single-phase like TPC pitch of 0.6 mm.

Looking at Figure 6.4 right (top and bottom), the photon shower distribution, it is possible to note a very low charge deposition in the first bin with respect to the following behaviour of the cascade. The reason of this is that the events in this plots are the ones with $d_{shower} = 0$. It means that the conversion has happened at the distance from the

generation point smaller than the strip dimension, but from the reconstructed information it is impossible to know exactly where within the strip it has happened: the amount of the charge deposited on the strip depends on the distance covered by the charged particles on the strip and therefore on the exact conversion point of the photon within the strip. In the electrons case, the situation is different being the primary electron always generated at the same point on the strip.

In Figure 6.5 it is shown the distribution of the distance between the Monte Carlo generation point and the shower starting point for two different configurations: the left plots shows the distribution in the case of $pitch = 0.3$ cm, the right one in the case of $pitch = 0.6$ cm.

In both cases the peak in the last bin in the distribution corresponds to the greatest value of d_{shower} in the region of interest for the analysis: ($d_{shower} = 62$ for the dual-phase case and $d_{shower} = 31$ for the single-phase case). This just means that the photon conversion in a electron/positron pair happens out of the region covered by the analysis. This is reasonable because the radiation length in liquid argon is $X_0 = 14$ cm and the exploited distance covered by the strips in view 0 is 18.6 cm.

The events in the first bin, *i.e.* those who have a distance $d_{shower} = 0$, are the ones corresponding to the entries in Figure 6.4 right top and bottom: for these events it is not possible to decide, at this level of the analysis based only on the presence of a gap, if they are generated by an electron or by a photon.

The number of the events with $d_{shower} = 0$ is 236 in the case of $pitch = 0.3$ cm and 451 in the case of $pitch = 0.6$ cm. The larger strips pitch implies the classification as $d_{shower} = 0$ also of the events where the photon conversion happens in correspondence of the second strip, which would be rejected in the case of the smaller strips pitch.

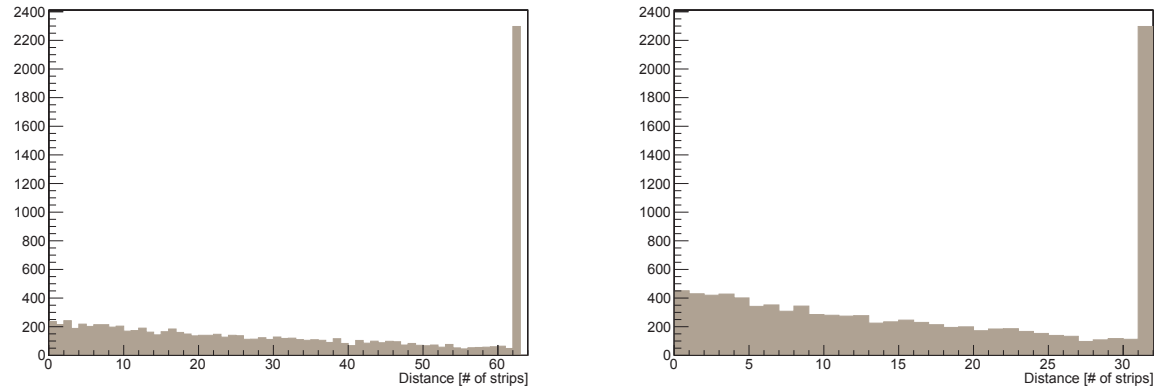

Figure 6.5: Distribution of the distance between the Monte Carlo generation point and the shower stating point in the case of $pitch = 0.3$ cm (left) and $pitch = 0.6$ cm (right).

By comparing the charge deposition for the showers generated by an electron and by a photon (see Figure 6.6) it is possible to note that the two distributions have a different

charge deposition for all the shower development (with the exception of the two last bins): this behaviour allows exploiting the comparison of the average charge deposited over several strips: for this work the optimal number of the strips used to evaluate the average charge deposited turned out to be 30 in the case of a $pitch = 0.3$ cm and 15 in the case of a $pitch = 0.6$ cm. This means that the charge taken into account to evaluate the ionization profile is the charge deposited by the shower along a distance of about 12.7 cm.

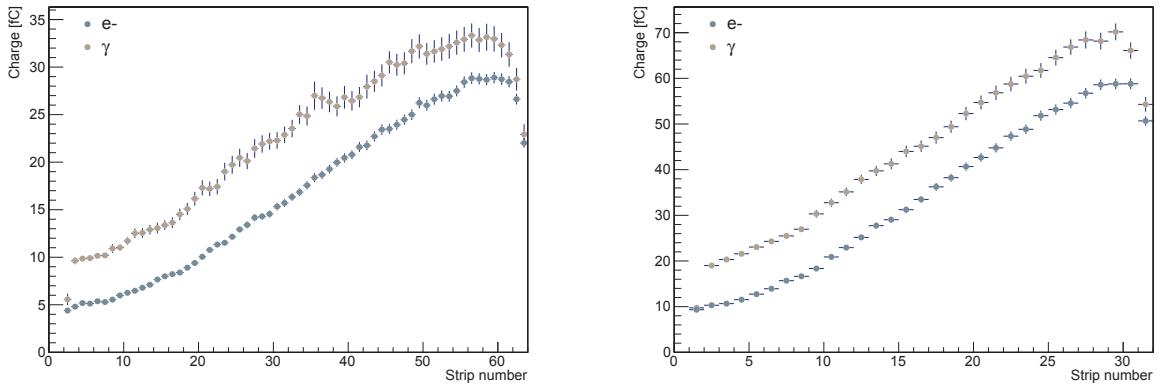

Figure 6.6: Comparison between the average charge collected for electron showers (blue dots) and photon showers (brown) in the case of $pitch = 0.3$ cm (left) and in the case of $pitch = 0.6$ cm (right).

In Figure 6.7 is shown the average charge produced by the showers in 12.7 cm collected using a readout with strips of 0.3 cm (left) and 0.6 cm (right).

Looking at the distributions in Figure 6.7, it is now possible to define two cuts in order to reject the events originated by a photon. It is possible to choose a lower cut-off q_{min} as a standard cut applied in the electron selection to make sure of having an electron-like track initiating a shower within one radiation length and to avoid more complicate situations related to the overlaps of hadrons with photon shower or hadrons having secondary interactions. It is reasonable to impose as a minimum average charge value $q_{min} = 4$ fC in the case of $pitch = 0.3$ cm. If the strip dimension is 0.6 cm, the minimum value imposed is $q_{min} = 8.5$ fC. In Table 6.1 are reported the results of this cut for the two different configurations.

In order to select an upper limit for the mean charge it is useful to look at the integral distribution of the charge (see Figure 6.8). Using these distributions it is possible to choose a cut according to the efficiency: for instance, to have an efficiency of 60% for the electrons (*i.e.* 600 events which pass the cut) in the case of $pitch = 0.3$ cm (Figure 6.8 left), the cut is $q_{max} \simeq 9$ fC. In the case of $pitch = 0.6$ cm (Figure 6.8 right) to have an efficiency of 60% for the electrons the cut to apply is $q_{max} \simeq 19$ fC.

In Table 6.2 are reported the number of events survived after the cuts $q_{min} = 4$ fC and $q_{max} = 9.5$ fC in the double phase case, and $q_{min} = 8.5$ fC and $q_{max} = 19$ fC in the single

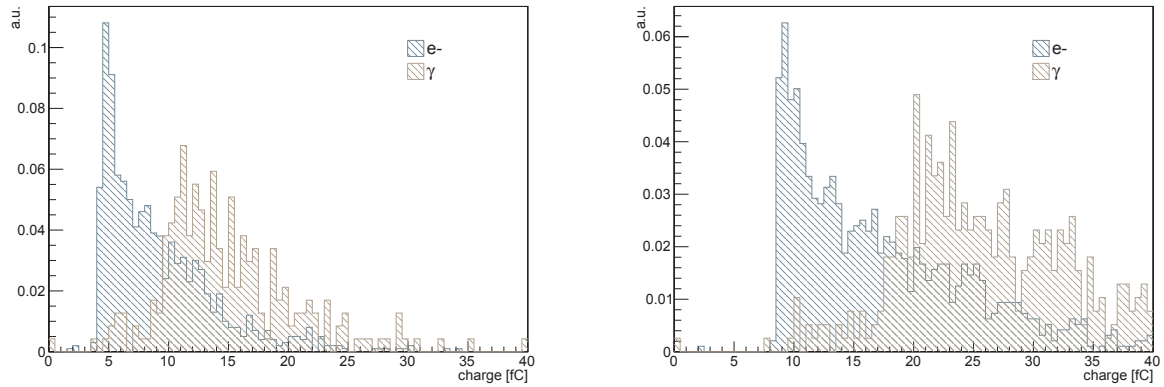

Figure 6.7: Comparison between the average charge deposition for electron showers (blue) and photon showers (brown). The mean is evaluated over 30 strips in the case of $pitch = 0.3$ cm (left) and over 15 strips in the case of $pitch = 0.6$ cm (right).

	Originating particle	Processed events	Events with $q > q_{min}$
$pitch = 0.3$ cm	**Electron**	1000	994
	Photon	236	233
$pitch = 0.6$ cm	**Electron**	1000	997
	Photon	451	450

Table 6.1: Number of events with a mean charge greater than q_{min}.

phase case.

As shown in Table 6.2, performing this study in the dual-phase TPC, with a strip pitch of 0.3 cm, by requiring an efficiency of 63% for a shower generated by an electron, the probability of mis-identification is 0.2%. In the single-phase TPC, to obtain an efficiency of 63% in the electron shower identification, the probability to misidentify the origin of the shower is 0.52%, more than the double with respect to the dual-phase case.

6.3 White noise effects

As last step of this analysis, the effects related to electronic response are taken into account, in order to study the impact of these effects on the analysis.

In Figure 6.9 is shown the average charge distribution with and without noise reconstructed over 12.7 cm in the case of the dual-phase TPC (top) and in the case of single-phase TPC (bottom).

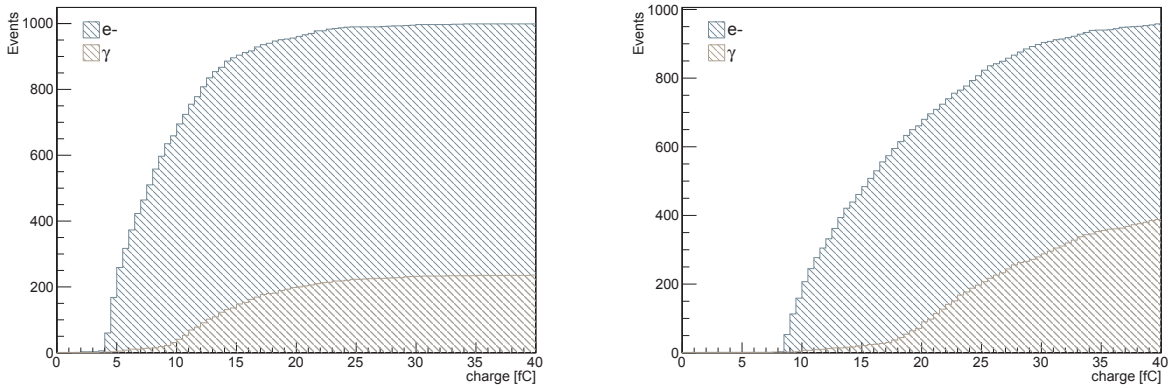

Figure 6.8: Average charge distribution for electron showers (blue area) and photon showers (brown area) in the case $pitch = 0.3$ cm (left) and in the case $pitch = 0.6$ cm (right).

	Originating particle	Total events	$d_{shower} = 0$	After cuts	Efficiency
$pitch = 0.3$ cm	**Electron**	1000	—	629	62.9%
	Photon	10000	236	20	0.20%
$pitch = 0.6$ cm	**Electron**	1000	—	630	63%
	Photon	10000	451	52	0.52%

Table 6.2: Results of the analysis after the cuts q_{min} and q_{max} in the diffetent configurations.

It is obvious that there are not many differences between the case without the noise and the case with the noise given the fact that the noise fluctuations are strongly integrated over the charge profile.

All the steps described above have been repeated for the simulation with the noise response, up to the calculation of the mean charge distribution over a distance of 12.7 cm (Figure 6.10).

Also, in this case the cuts over the mean charge have been applied, following the idea described above:

$$pitch = 0.3 \text{ cm} \begin{cases} q_{min} = 4.0 \text{ fC} \\ q_{max} = 9.5 \text{ fC} \end{cases}$$

$$pitch = 0.6 \text{ cm} \begin{cases} q_{min} = 8.5 \text{ fC} \\ q_{max} = 19.0 \text{ fC} \end{cases}$$

The results of these cuts are reported in Table 6.3.

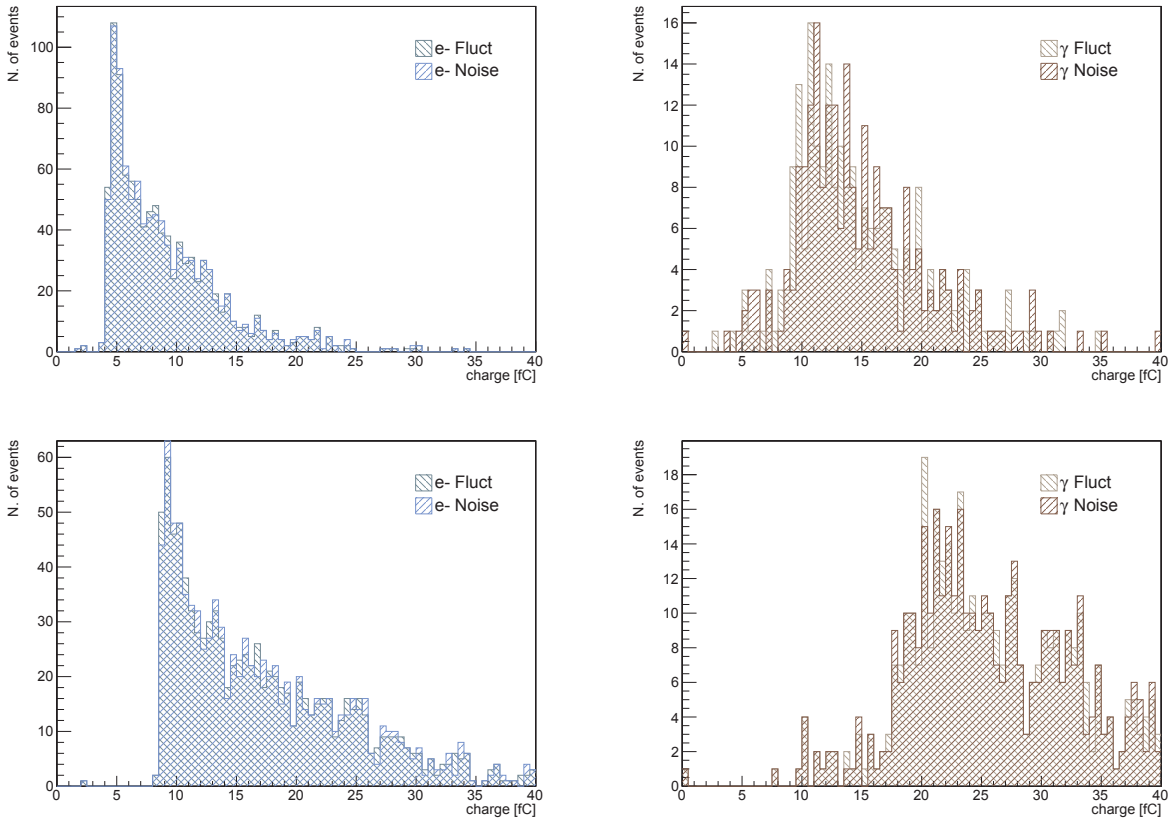

Figure 6.9: Top: average charge distribution with and without the noise effects for electron showers (left) and photon showers (right) in the case of $pitch = 0.3$ cm. Bottom: average charge distribution with and without the noise effects for electron showers (left) and photon showers (right) in the case of $pitch = 0.6$ cm.

6.4 Summary

Electromagnetic showers produced by a photon originating by π^0 decay represent an important background for ν_e CC interactions selection. For this reason it is crucial to have a good method to discriminate this kind of events from electromagnetic showers originated by prompt electrons coming out from ν_e CC interactions.

The purpose of this study is to use the charge profile collected at the beginning of the shower to disentangle the origin of the showers: if the originating particle is a photon, it first produces a couple electron/positron, which deposits the double of the energy with respect to the case where the mother particle is a single electron.

In addition, another parameter used as discriminator to identify an electromagnetic shower generated by a photon is the distance d_{shower} between the neutrino vertex position and the point where the electron/positron conversion happens: if d_{shower} is non 0 it is

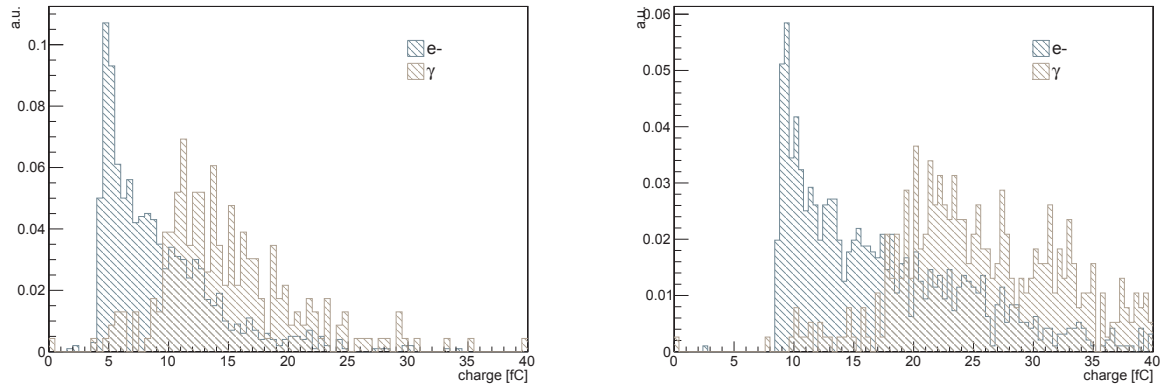

Figure 6.10: Comparison between the mean charge deposition for electron showers (blue) and photon showers (brown). The average is evaluated over 30 strips in the case of $pitch = 0.3$ cm (left) and over 15 strips in the case of $pitch = 0.6$ cm (right) taking into account the noise response.

	Originating particle	Total events	$d_{shower} = 0$	After cuts	Efficiency
$pitch = 0.3$ cm	**Electron**	1000	—	626	62.6%
	Photon	10000	231	20	0.20%
$pitch = 0.6$ cm	**Electron**	1000	—	627	62.7%
	Photon	10000	445	51	0.51%

Table 6.3: Results of the analysis after the cuts q_{min} and q_{max} in the different configurations, in the case of noise effects.

obvious that the shower has been originated by a photon.

The analysis has been performed by comparing results obtained using the dual-phase readout (strips size of 0.3 mm) and a pitch similar to the one foreseen for the single phase pitch (strips size of 0.6 mm).

Looking at the charge distribution collected in the first 12.7 cm for the two type of electromagnetic showers, two cuts have been studied in order to reject the events generated by a photon. The lower cut-off q_{min} is based on the minimal $\mathrm{d}E/\,\mathrm{d}x$ deposited by a particle. The upper cut q_{max} has been chosen to have an efficiency of $\approx 60\%$.

Requiring a selection efficiency on the electron generated showers of 63%, the misidentified shower rate is 0.2% in the case of $pitch = 0.3$ mm and 0.5% in the case of $pitch = 0.6$ mm. This effect is quite important since it corresponds to doubling the background. It has also been verified that the presence of the noise in the simulation does not change the results.

This study shows how a liquid argon TPC can provide a good separation between electron generated and photon generated electromagnetic showers. Furthermore, it has been demonstrated how a smaller size of the pitch in the electronic readout allows to achieve a better photon rejection.

Chapter 7

Conclusions

A crucial challenge for the future of Particle Physics is the study of the neutrino masses and mixing, representing the first evidence of Physics beyond Standard Model. Thanks to the recent results achieved, it is now possible investigate the CP violation in neutrino sector. Giant Liquid Argon Time Projection Chambers (LAr TPCs) represent the ideal detectors to perform measurements which can permit to discover evidence for CP violation in the neutrino sector. LAr TPCs provide a very good quality imaging coupled to excellent energy resolution and particle identification capabilities. A new technique called dual-phase Liquid Argon Time Projection Chamber (DP LAr TPC) introduces multiplication in the vapor phase present above the liquid phase: in this way it is possible to increase the signal collected by the readout charge system located at the top of the detector. This allows obtaining typical $S/N \sim 100$. In the gaseous phase the multiplication of electrons is achieved in avalanches occurring in a high electric field within the micro-pattern structure of the Large Electron Multiplier (LEM).

The operation of the LEM in the dual-phase liquid argon TPC requires a good knowledge about the maximal voltage that can be applied to the LEM before starting an electric arc. For this reason a detailed study aimed at verifying the Paschen law has been performed: first of all it has been demonstrated that a parametrization of the breakdown tension $V_b = V_b(dp,\ d)$, which includes a linear dependence on the distance, is in agreement with the experimental data. Subsequently a correction factor δ has been introduced, to take into account the gas density variations due to the pressure and temperature fluctuations. Finally a global parametrization is proposed and explained how it can be applied to a general case of temperature and pressure conditions.

The goal of this thesis is to study and analyze the charge reconstruction in dual-phase LAr TPC. The charge readout is crucial for a neutrino experiment seeking for rare events using a liquid argon TPC. After an accurate comparison between the theoretical knowledge about energy losses and the simulation performed by `GEANT`, all the effects related to the detector response have been scrutinized. The aspects taken into account for this analysis are directly related to the simulation of the response of the readout system, through the response function of the electronics and the digitization of the signal, and the hit reconstruction algorithm. The reconstructed energy, when directly compared to the deposited

energy after quenching effects, differs from the Monte Carlo simulation by a value between 0.03% and 0.3%. Reconstructed energies are always smaller than those simulated: this effect is due to the reconstruction algorithm which introduces a small systematic effect related to the way charge is quantized and samples assigned to the hits. Finally a calculation of the reconstructed energy by taking into account an empirical correction for the quenching effects has been performed: in this case the discrepancy between the reconstructed energies and the Monte Carlo truth is significantly worse than the one obtained only considering reconstruction effect, with a systematic bias of 3.5% for the most realistic case. The reason of this is due to the empirical correction for the quenching factor $\mathcal{R}$: at the level of the reconstructed energy this factor can be estimated only from the total energy seen by a strip after quenching and cannot account for microscopic effects corresponding to more concentrated charge depositions within the strip, like in case of delta rays emission, which at the generation level produce stronger recombination effects.

The study of energy losses provides an important handle for particle identification: by sampling the trajectory of a charged particle and by measuring its energy losses, it is possible to identify its nature. In this thesis this method has been used to define a discrimination between kaons and pion: this is crucial in the proton decay search, looking for the exclusive channel $p \to K^+\overline{\nu}$. After sampling at the hits level the kaons and pions energy depositions, a parametrization has been computed to describe the energy losses of these particles nearby their stopping point, using a a linear combination of power law function and exponential. By using this parametrization, a χ^2 has been defined in order to disentangle the two populations. In the more realistic case the kaon identification efficiency reaches 99.8%, with a pion mis-identification of 1.7%. A further separation between kaon and pion samples can been achieved by looking at the kinematics of the entire decay chain. Combining the energy losses information with the χ^2 defined above, it is possible to reach a lower pion mis-identification rate of 0.6% in the full simulation realistic case.

Finally it has been shown how it is possible to perform π^0 rejection by studying energy losses of the charged track segment originating electron candidate showers. In an experiment studying $\nu_\mu \to \nu_e$ oscillations the reconstruction of the electrons shower represents a crucial step in the neutrino event reconstruction. The study presented in this thesis uses the charge profile collected at the beginning of the electromagnetic showers in order to disentangle the origin of the shower. Another parameter used as discriminator to identify an electromagnetic shower generated by a photon is the distance d_{shower} between the neutrino vertex position and the point where the electron/positron conversion happens. The analysis has been performed by comparing results obtained using the dual-phase readout (strip size of 3 mm) and a pitch similar to the one which will be used for the single-phase readout (strip size of 6 mm). Requiring a selection efficiency on the electron generated showers of 63%, the misidentified shower rate is 0.2% in the case of $pitch = 0.3$ mm and 0.5% in the case of $pitch = 0.6$ mm.

Bibliography

[1] Jr. R. Davis. "A progress report on the Brookhaven Solar neutrino experiment". *abstract of an invited paper for the Washington meeting of the APS*, 1972.

[2] B. Aharmim et al. (SNO Collaboration). "Low-energy-threshold analysis of the Phase I and Phase II data sets of the Sudbury Neutrino Observatory". *Phys. Rev. C*, 81, 2010.

[3] Bellerive et al. (SNO Collaboration). "The Sudbury Neutrino Observatory". *Nucl. Phys.*, B, 2016.

[4] R. Jeffrey Wilkes. "New results from Super-K and K2K". *arXiv:hep-ex/0212035v1*, 2016.

[5] M. Koshiba. "Kamiokande experiment". *SLAC Summer Institute.*, 1998.

[6] R. Becker-Szendy et al. "IMB-3: A Large water Cerenkov detector for nucleon decay and neutrino interactions". *Nucl. Instrum. Meth. A*, 324:363, 1993.

[7] M. H. Ahn et al. "Measurement of neutrino oscillation by the K2K experiment". *Phys Rev. D*, 74:072003, 2006.

[8] Z. Maki, M. Nakagawa, and S. Sakata. "Remarks on the Unified Model of Elementary Particles". *Progress of Theoretical Physics*, 28(5):870–880, 1962.

[9] M Kobayashi and T. Maskawa. "CP-Violation in the Renormalizable Theory of Weak Interaction". *Progress of Theoretical Physics*, 49(2):652 – 657, 1973.

[10] Jen-Chieh Peng for the Daya Bay Collaboration. "Daya Bay: Results and Perspectives". *Nucl. Part. Phys. Proc.*, 265:105 – 110, 2015.

[11] Soo-Bong Kim. "New results from RENO and prospects with RENO-50". *Nucl. Part. Phys. Proc.*, 265-266:93 – 98, 2015.

[12] Michiru Kanedaa on behalf of the Double Chooz Collaboration. "Results from the Double Chooz experiment". *EPJ Web Conf.*, 125, 2016.

[13] B. T. Cleveland et al. "Measurement of the solar electron neutrino flux with the Homestake chlorine detector". *Astrophys. J.*, 496:505–526, 1998.

[14] F. Kaether, W. Hampel, G. Heusser, J. Kiko, and T. Kirsten. "Reanalysis of the GALLEX solar neutrino flux and source experiments". *Phys. Lett.*, B685:47–54, 2010.

[15] SAGE Collaboration. "Measurement of the solar neutrino capture rate with gallium metal. III: Results for the 2002-2007 data-taking period". *Phys. Rev. C*, 80:015807, 2009.

[16] Super-Kamiokande Collaboration. "Solar neutrino measurements in Super-Kamiokande-I". *Phys. Rev. D*, 73:112001, 2006.

[17] Super-Kamiokande Collaboration. "Solar neutrino measurements in Super-Kamiokande-II". *Phys. Rev. D*, 78:032002, 2008.

[18] Super-Kamiokande Collaboration. "Solar neutrino measurements in Super-Kamiokande-III". *Phys. Rev. D*, 83:052010, 2011.

[19] Y. Nakano. *"^{8}B solar neutrino spectrum measurement using Super-Kamiokande IV"*. PhD thesis, Tokyo University, 2016.

[20] Y. Nakano. "Solar neutrino results from Super-Kamiokande". Talk given at the *38th International Conference on High Energy Physics*, Chicago, USA, 2016.

[21] SNO Collaboration. "Combined Analysis of all Three Phases of Solar Neutrino Data from the Sudbury Neutrino Observatory". *Phys. Rev. C*, 88:025501, 2013.

[22] Borexino Collaboration. "Precision measurement of the ^{7}Be solar neutrino interaction rate in Borexino". *Phys. Rev. Lett*, 107:141302, 2011.

[23] Borexino Collaboration. "Measurement of the solar ^{8}B neutrino rate with a liquid scintillator target and 3 MeV energy threshold in the Borexino detector". *Phys. Rev. D*, 82:033006, 2010.

[24] Borexino Collaboration. "Neutrinos from the primary proton-proton fusion process in the Sun". *Nature*, 512:383–386, 2014.

[25] MINOS Collaboration. "Measurement of Neutrino and Antineutrino Oscillations Using Beam and Atmospheric Data in MINOS". *Phys.Rev. Lett*, 110:251801, 2013.

[26] MINOS Collaboration. "Electron neutrino and antineutrino appearance in the full MINOS data sample". *Phys.Rev. Lett*, 2013.

[27] K. Iwamoto. "Recent Results from T2K and Future Prospects". Talk given at the *38th International Conference on High Energy Physics*, Chicago, USA, 2016.

[28] A. Cervera. "Latest Results from Neutrino Oscillation Experiments". Talk given at the *SUSY 2016 Conference*, Melbourne, Australia, 2016.

[29] P. Vahle. "New results from NOνA". Talk given at the SUSY 2016 Conference, Melbourne, Australia, 2016.

[30] KamLAND Collaboration. "Constraints on ϑ_{13} from a Three-Flavor Oscillation Analysis of Reactor Antineutrinos at KamLAND". *Phys. Rev. D*, 83, 2011.

[31] CHOOZ Collaboration. "Limits on Neutrino Oscillations from the CHOOZ Experiment". *Phys. Rev. B*, 466:415–430, 1990.

[32] Palo Verde Collaboration. "Final results from the Palo Verde neutrino oscillation experiment". *Prog. Part. Nucl. Phys*, 48:113–121, 2002.

[33] M. Ishitsuka. "New results of Double Chooz". Talk given at the Conference *Rencontres de Moriond EW 2016*, La Thuile, Italy, 2016.

[34] Z. Yu. "Recent Results from the Daya Bay Experiment". Talk given at the *XXVII International Conference on Neutrino Physics and Astrophysics*, London, UK, 2016.

[35] S-H. Seo. "New Results from RENO". Talk given at the *XXVI International Conference on Neutrino Physics and Astrophysics*, Boston, USA, 2014.

[36] I. Esteban et al. "Updated fit to three neutrino mixing: exploring the accelerator-reactor complementarity". *JHEP, arXiv:1611.01514*, 2016.

[37] J. Arafune et al. "CP Violation and Matter Effect in Long Baseline Neutrino Oscillation Experiments". *Phys.Rev. D*, 56, 1999.

[38] S. K. et a. Agarwalla. "The mass-hierarchy and CP-violation discovery reach of the LBNO long-baseline neutrino experiment". *JHEP*, 05:094, 2014.

[39] R. et al Acciarri. "Long-Baseline Neutrino Facility (LBNF) and Deep Underground Neutrino Experiment (DUNE)". *arXiv:1512.06148*, 2015.

[40] C. Rubbia. "The Liquid-Argon Time Projection Chamber: a new concept for neutrino detectors". *EP Internal Report 77-8*, 1977.

[41] Davide R. Nygren. "Proposal to investigate the feasibility of a novel concept in particle detection". *INSPIRE-1365360*, 2009.

[42] M. Antonello et al. "Underground operation of the ICARUS T600 LAr-TPC: first results". *Journal of Instrumentation*, 6(07):P07011, 2010.

[43] C. Caso et al. (*Particle Data Group*). *"Review of Particle Physics"*. Eur. Phys. J. C, 3, 1998.

[44] K. Nakamura et al. (*Particle Data Group*). *"Review of Particle Physics"*. J.Phys. G, 37, 2010.

[45] L. Onsager. "Initial recombination of ions". *Phys. Rev.*, 54:554–557, 1938.

[46] G. Jaffé. "Zur Theorie der Ionisation in Kolonnen". *Ann. der Phys.*, 42:304 – 344, 1913.

[47] J. Thomas and D. A. Imel. "Recombination of electron-ion pairs in liquid argon and liquid xenon". *Phys. Rev. A*, 36:614–616, 1987.

[48] J. Birks. "Theory and Practice of Scintillation Counting". *Pergamon Press*, 1964.

[49] S. Amoruso et al. "Study of electron recombination in liquid argon with the ICARUS TPC". *Nucl. Instrum. Meth.*, A 523:275–286, 2004.

[50] T. Doke et al. "Estimation of absolute photon yields in Liquid Argon and Xenon for relativistic (1MeV) electrons". *Nucl. Instrum. Meth.*, A 291:617–620, 2004.

[51] C Amsler et al. "Luminescence quenching of the triplet excimer state by air traces in gaseous argon". *Journal of Instrumentation*, 3(02):P02001, 2008.

[52] The ArDM collaboration. "Development of wavelength shifter coated reflectors for the ArDM argon dark matter detector". *JINST*, 4:P06001, 2009.

[53] W. Walkowiak. "Drift velocity of free electrons in liquid argon". *Nucl. Instrum. Meth.*, A449:288–294, 2000.

[54] E. Buckley et al. "a study of ionisation electrons drifting over large distance in Liquid Argon". *Nucl. Instrum. Meth.*, A 275:364–372, 1989.

[55] The ProtoDUNE Dual Phase Collaboration. "Yearly progress report on WA105/ProtoDUNE dual phase (2016)". *SPSC-SR-184*, 2016.

[56] M. Antonello et al. "Experimental observation of an extremely high electron lifetime with the ICARUS-T600 LAr-TPC". *JINST*, 9(12):P12006, 2014.

[57] The MicroBooNE Collaboration. "Measurement of the Electronegative Contaminants and Drift Electron Lifetime in the MicroBooNE Experiment". *MICROBOONE-NOTE-1003-PUB*, 2016.

[58] M. Suzuki et al. "Momentum transfer cross section of argon deduced from electron drift velocity data". *Journal of Physics D: Applied Physics*, 23(7):842 – 850, 1990.

[59] E. Shibamura et al. "Ratio of diffusion coefficient to mobility for electrons in liquid argon". *Phys. Rev. A*, 20(6):2547 – 2554, 1979.

[60] B. A. Dolgshein et al. "New method of registration of ionizing-particle tracks in condensed matter". *PETP LETTERS*, 1970.

[61] E. M. Gushchin et al. "Emission of hot electrons from liquid and solid Argon and Xenon". *Sov. Phys. JETP*, 55(5):860–862, 1982.

[62] A Badertscher et al. "Construction and operation of a double phase LAr Large Electron Multiplier Time projection chamber". *ArXiv:0811.3384*, 2008.

[63] C. Cantini et al. "Performance study of the effective gain of the double phase liquid Argon LEM Time Projection Chamber". *JINST*, 2014.

[64] A Badertscher et al. "First operation of a double phase LAr Large Electron Multiplier Time Projection Chamber with a two-dimensional projective readout anode". *Nucl. Instrum. Meth.*, A641, 2011.

[65] The LBNO-DEMO (WA105) Collaboration. "Technical Design Report for large-scale neutrino detectors prototyping and phased performance assessment in view of a long-baseline oscillation experiment". Technical Report CERN-SPSC-2014-013. SPSC-TDR-004. arXiv:1409.4405, CERN, 2014.

[66] R. Acciarri et al. "Long-Baseline Neutrino Facility (LBNF) and Deep Underground Neutrino Experiment (DUNE)". *arXiv:1601.05471*, 2016.

[67] F. Paschen. "Ueber die zum Funkenübergang in Luft, Wasserstoff und Kohlensäure bei verschiedenen Drucken erforderliche Potentialdifferenz". *Annalen der Physik*, 37:69 – 96, 1889.

[68] L. Ledernez et al. "A modification of Paschen law for Argon". 29th *ICPIG*, 2009.

[69] Elyse Sili and Jean Pascal Cambronne. "A new empirical expression of the breakdown voltage for combined variation of temperature and pressure". *World Academy of Science, Engineering and Technology*, 63:270–275, 2012.

[70] R. Reid et al. *The Properties of Gases and Liquids*. McGraw-Hill, fourth edition edition, 1987.

[71] A. Ankowski et al. "Energy reconstruction of electromagnetic showers from π^0 decays with the ICARUS T600 Liquid Argon TPC". *Acta Phys. Polon.*, B 41:103–125, 2010.

[72] F. Arneodo et al. (The ICARUS-Milano Collaboration). "Performance of a liquid argon time projection chamber exposed to the CERN West Area Neutrino Facility neutrino beam". *Phys. Rev. D*, 74(07):112001, 2006.

[73] J. Rico. *"First study of the stopping muon sample with the ICARUS T600 detector"*. PhD thesis, ETH ZURICH, 2002.

[74] D. Lussi. *"Study of the response of the novel LAr LEM-TPC detector exposed to cosmic rays and a charged particle beam"*. PhD thesis, ETH ZURICH, 2013.

[75] W. H. Press et al. *Numerical recipes in C: the art of scientific computing*. Cambridge University Press, 2 edition, 1992.

[76] V. Houng and C. Paul. "Method and means for recognizing complex patterns", 1962.

[77] C. Cantini et al. "Long-term operation of a double phase LAr LEM time projection chamber with a simplified anode and extraction-grid design". *JINST*, 9, 2014.

[78] pdg.lbl.gov/2012/AtomicNuclearProperties.

[79] D. E. Groom et al. "Muon stopping power and range tables 10 MeV to 100 TeV". *Atom. Data Nucl. Data Tabl.*, 78:183–356, 2001.

[80] W.H.Barkas. Technical Report 10292. Technical report, UCRL, 2016.

[81] GEANT team. *"GEANT User's Guide"*, 1993.

[82] S. Agostinelli et al. "Geant4 – a simulation toolkit". *Nucl. Instrum. Meth.*, A 506:250–303, 2003.

[83] J. Klinger, V. A. Kudryavtsev, M. Richardson, and N. J. C. Spooner. "Muon-induced background to proton decay in the $p \to K^+\nu$ decay channel with large underground liquid argon TPC detectors". *Phys. Lett.*, B746:44–47, 2015.

[84] A. Bueno et al. "Nucleon decay searches with large liquid argon TPC detectors at shallow depths: Atmospheric neutrinos and cosmogenic backgrounds". *JHEP*, 04:041, 2007.

[85] A. Stahl et al. "Expression of Interest for a very long baseline neutrino oscillation experiment (LBNO)". *CERN-SPSC-2012-021, SPSC-EOI-007*, 2012.

[86] J. C. Pati and A. Salam. "Is Baryon Number Conserved?". *Phys. Rev. Lett.*, 32:661–664, 1974.

[87] H. Georgi and S. Glashow. "Unity of All Elementary Particle Forces". *Phys. Rev. Lett.*, 32:438–441, 1974.

[88] S. Dimopoulos et al. "Proton Decay in Supersymmetric Models". *Phys. Rev. Lett.*, B112, 1982.

[89] The Super-Kamiokande Collaboration. "Search for Proton Decay via $p \to \nu K^+$ using 260 kiloton $\cdot$ year data of Super-Kamiokande". *Phys. Rev. D*, 90, 2014.

[90] M. Antonello et al. "Precise 3D track reconstruction algorithm for the ICARUS T600 liquid argon time projection chamber detector". *Adv. High Energy Phys.*, 2013.

[91] F. Arneodo et al. "The ICARUS 50 L LAr TPC in the CERN neutrino beam". In *New detectors. Proceedings, 36th Workshop of the INFN Eloisatron Project, Erice, Italy, November 1-7, 1997*, pages 3–12, 1998.